UNIVERSITY OF SOUTHAMPTON

FACULTY OF ENGINEERING, SCIENCE AND MATHEMATICS

Optoelectronics Research Centre

HIGH POWER NANOSECOND PULSED FIBER LASER AMPLIFIERS

by

Khu Tri Vu

Thesis for the degree of Master of Philosophy

January 2008

UNIVERSITY OF SOUTHAMPTON

ABSTRACT

FACULTY OF ENGINEERING, SCIENCE AND MATHEMATICS
Optoelectronic Research Centre

Master of Philosophy

HIGH POWER NANOSECOND PULSED FIBER LASER AMPLIFIERS

by Khu Tri Vu

This project is to develop a high power nanosecond pulsed fiber laser amplifier using large mode area fibers doped with Ytterbium. It first focuses on building an all-fiber master oscillator power amplifier (MOPA) system that is capable of performing at high peak power and pulse energy with high beam quality. The performance of the MOPA then is improved in term of the usability of the output pulse with active adaptive pulse shaping.

Large mode area (LMA) fibers with very low numerical aperture (NA) are characterised and used. These fibers help to increase the mode field diameters and keep the number of modes at a manageable level. The fiber diameters are in the range of 20-40μm and the NA is around 0.06. Due to the high bend loss of higher order modes compared to the fundamental, it is possible to improve the mode quality though bending the fibers at appropriate bending radii. For a top-hat refractive index profile with NA of 0.06, the critical bending radii for 20μm, 30μm and 40μm are 90mm, 50mm and 30mm, respectively.

In the first MOPA setup, the 1077nm signal output of the single mode preamplifier is passed to the post-amplification stage consisting of an LMA GTwave fiber of 20μm core. This stage is pumped with a high power pigtailed pump at 915nm. The long (100ns) rectangular seed pulses are significantly reshaped and producing narrowed pulses ($\sim$30ns) with an extended tail. With a 3m delivery fibre after the final stage amplifier passive fiber, the peak power with no Stimulated Raman Scattering (SRS) component is about 13kW. For short pulse amplification (20ns), the amount of reshaping is small before a large amount of SRS is observed. The total peak power of the pulse including the SRS components can be as high as 30kW.

The experimental results shows that most of SRS power is generated in the passive delivery fiber. There are two possible techniques to improve the performance of the MOPA: use of a photonic bandgap delivery fiber offering low nonlinearity per unit length, and the use of preshaped pulse to maintain a constant peak power across the full pulse duration.

Active pulse shaping using a simulated annealing algorithm is performed. In the first instance, direct shaping of the diode is deployed. The output pulses are shaped to square, triangular and two-step pulses as a demonstration of the capability of the technique. Then, an Electro-Optic Modulator (EOM) is used in the MOPA setup with a free space launched 30μm fiber postamplifier which produced 1mJ output pulses at 20kHz repetition rate. This improves the extinction ratio significantly and allows shaping algorithm to produce 1mJ square pulse of high energy without nonlinear effects. A 1mJ square pulse with duration of 100ns and long two-stepped pulse of duration of up to 10μs are produced. This adaptive method can generate any arbitrarily desired pulse shapes. The square pulse output is then used to generated individual SRS order components in a single mode fiber.

A gain-switched setup is also investigated as a 1060nm picosecond pulse source for the MOPA. Injection and self seeding are comparatively studied using the EOM-FROG technique. It is concluded that the inexpensive and simple self seeding gives similar performance compared to the expensive injection seeding using a distributed feed back laser. Pulses of 1GHz in repetition rate and 70ps in duration are produced directly from the diode. A linearly chirped Bragg fiber gratings is used to compress the pulse to below 20ps reducing the time bandwidth product from 3 to 0.7.

Contents

Declaration of Authorship

I, Khu Tri Vu, declare that the thesis entitled **HIGH POWER NANOSECOND PULSED FIBER AMPLIFIERS** and the work presented in the thesis are both my own, and have been generated by me as the result of my own original research from October 2004 to December 2006. I confirm that:

- this work was done wholly or mainly while in candidature for a research degree at this University;
- where any part of this thesis has previously been submitted for a degree or any other qualification at this University or any other institution, this has been clearly stated;
- where I have consulted the published work of others, this is always clearly attributed;
- where I have quoted from the work of others, the source is always given. With the exception of such quotations, this thesis is entirely my own work;
- I have acknowledged all main sources of help;
- where the thesis is based on work done by myself jointly with others, I have made clear exactly what was done by others and what I have contributed myself;
- parts of this work have been published as:
  - K. T. Vu, A. Malinowski, M. A. F. Roelens, M. Ibsen, P. Petropoulos, D. J. Richardson. Full Characterisation of Low Power Picosecond Pulses From a Gain-Switched Diode Laser using Electro-Optic Modulation Based Linear FROG. Photonics Technology Letters. Accepted Jan 2008.
  - K.T. Vu, A. Malinowski, M.A.F. Roelens, M. Ibsen, D.J. Richardson. Detailed Comparison of Injection-Seeded and Self-Seeded Performance of a Gain-Switched Laser Diode. CLEO 2007, Baltimore, US, paper JWA119.
  - K.T. Vu, A. Malinowski, M.A.F. Roelens, M. Ibsen, P. Petropoulos, D.J. Richardson. Full Characterisation of Low Power Picosecond Pulses From a Gain-Switched Diode Laser using Electro-Optic Modulation Based FROG. CLEO 2007, Baltimore, US, paper CFF4.
  - K.T. Vu, A. Malinowski, D. J. Richardson, F. Ghiringhelli, L. M. B. Hickey, and M. N. Zervas. Adaptive pulse shape control in a diode-seeded nanosecond fiber MOPA system. Opt. Express 14, 10996-11001 (2006).
  - F. He, J. H. Price, K. T. Vu, A. Malinowski, J. K. Sahu, and D. J. Richardson. Optimisation of cascaded Yb fiber amplifier chains using numerical-modelling. Opt. Express 14, 12846-12858 (2006).

Khu Tri Vu
15 January 2008

Acknowledgements

There has been so much help from everyone who I know and have met during my studies that I would like to thank them deeply. Although I am trying to name some people that I can think of at the moment of writing, there are many others who I may fail to mention and for this I apologise.

First of all I would like to say thank you to my supervisors, Professor Dave Richardson and Dr Andy Malinowski. They have done their best for me throughout my studies. Prof. Dave Richardson has given me all of the guidance that I needed all the way. Dr Andy Malinowski has shown great patience to me. He is always there for me to ask for help and guidance. They have been very encouraging people, who spent a considerable amount of time with me during the duration of my research.

I would like to specially thank other member of Professor Richardson's fiber laser group with whom I have shared the equipment and ideas. I am particularly grateful to Fei He and Dr Jonathan Price for the many useful discussions and for letting me access equipment and components whenever I needed them.

In addition, I acknowledge those who have directly helped with the work presented in this thesis. I am grateful for the contribution of all my co-workers during the research progress. In particular, I would like to thank Dr Fabio Ghiringhelli, Dr Louise Hickey and Professor Mikhail Zervas at Southampton Photonics Inc. for their cooperation in development of GTWave fiber amplifiers. I would like to thank Dr Joanne Flanagan for her help with characterisation of the large mode fibers. I thank Dr Janata Sahu and Mr John Hayes for fabricating many fibers that I used. I thank Dr Andy Piper and Pascal Dupriez for their work which provided my initial laser and amplifier setup. I thank Dr Michaël Roelens for sharing the FROG code and helping me with the gain-switching setup. I am grateful for the contribution of Dr Morten Ibsen in fabricating chirped fiber Bragg gratings. I would like to thank Kang Chen and Paulo Almeida for helping me with the experimental work in the final stage of the research and for carrying on the work I have started.

I thank all of the technicians, IT and supporting staffs for their help during the time I stayed at the ORC. I send my special thank to Ms Eve Smith for being such a fantastic student supporter. I would like also thank Dr Eleanor Tarbox for her guidance through out the course as a Tutor. Then, I also thank those who share my office with me in Portacabin B and then Room 1015/47.

I acknowledge support of Universities UK and University of Southampton for providing the Overseas Research Studentship. I acknowledge the support of Southampton Photonics Inc. for letting me using their many R&D components.

I also thank all members of Vietnamese Society in Southampton for providing a home away from home. I specially thank Dr Dong Trung Huynh's family for being such lovely friends with whom I deeply enjoyed being with everyday.

Most important of all, this is a tribute to my family who are always my love and encouragement even at a very far distance. They are always the motivation for every thing I have done in my life. Finally I would like to thank my wife, Uyen Nguyen, for being a patient, devoted and unconditional companion.

List of Abbreviations

AOM	Acousto-Optic Modulator
ASE	Amplified Spontaneous Emission
AWG	Arbitrary Waveform Generator
BDO	Beam Deliver Optics
CFBG	Chirped Fiber Bragg Gratings
CPA	Chirped Pulse Amplification
CW	Continuous Wave
DCA	Digital Communication Analyser
DCF	Double-Clad Fiber
DFB	Distributed Feedback
EOM	Electro-Optic Modulator
ESA	Excited State Absorption
FROG	Frequency-Resolved Optical Gating
FP	Fabry-Perot
FWHM	Full Width at Half Maximum
LMA	Large Mode Area
MCVD	Modified Chemical Vapour Deposition
MFD	Mode Field Diameter
MOPA	Master Oscillator Power Amplifier
NA	Numerical Aperture
OD	Outer Diameter
OPO	Optical Parametric Oscillator
ORC	Optoelectronics Research Centre
OSA	Optical Spectrum Analyser
PBGF	Photonics Band Gap Fiber
PC	Polarisation Controller
SA	Simulated Annealing
SBS	Stimulated Brillouin Scattering
SHG	Second Harmonic Generation
SMSR	Side-Mode Suppression Ratio
SPI	Southampton Photonics Inc.
SPM	Self-Phase Modulation
SRS	Stimulated Raman Scattering
TBWP	Time-Bandwidth Product
WDM	Wavelength Division Multiplexing

Chapter 1

Introduction

1.1 Motivation

This project is concerned primarily with development of high energy pulsed laser amplifiers operating in the nanosecond regime. Fiber lasers and amplifiers offer several advantages over conventional solid-state lasers. Rare-earth doped glass fiber lasers have much higher efficiency than crystal host solid-state lasers. Also, the spectral transitions in glass are much broader than they are in crystals, which leads to the possibility of broadband amplification, tunable lasers and very short pulse sources. The beam quality of the output is purely determined by the structure and configuration of the fiber. The development of all fiber lasers and amplifiers is leading to cheap, robust and compact replacements for expensive, complicated solid-state lasers. Fiber lasers are arguably the most powerful solid-state laser technology available today. They are very competitive in performance terms to crystal host solid state lasers in industrial applications such as welding and materials processing and offer significant benefits in term of compactness and power efficiency.

The increasing numbers of applications of ultrafast pulsed lasers have been held back by the cost of solid state laser systems. Most current commercial ultrafast optical systems are based on mode-locked Ti:Sapphire lasers. They are bulky, expensive and are not readily scalable to the multiwatt average powers required by some applications. The high power nanosecond regime lasers use Nd-doped glass that require careful thermal management to avoid beam quality distortion. Existing very high power applications are currently served by even more bulky and expensive gas laser systems which cannot provide femtosecond pulses. Fiber laser systems have good mode quality and are low cost and compact. They are generally pumped with compact diode laser sources which are available commercially at low cost. The aim of this project is to develop single transverse mode Ytterbium (Yb)-doped fiber amplifiers with output pulses of more than 1mJ. Initial work is on nanosecond pulses, but the work will be extended to ultrafast pulses as the project progresses.

The first phase of this project was to develop an all-fiber nanosecond amplifier using a Master Oscillator and Power Amplifier (MOPA) configuration. This phase was funded by Southampton Photonics Inc. (SPI). The project was in close collaboration with SPI's engineering and product development teams. The target application parameters were a pulse energy of greater than 1mJ, an average power of more than 100W, for pulse lengths of a few tens of nanosecond, all with an optical conversion efficiency of more than 50%. The wavelength of operation was to be around 1070nm from a directly modulated laser diode. These pulses have peak powers of tens of kW which dictate the use of Large Mode Area (LMA) fibers to control the maximum optical intensity in the core in order to limit the effect of nonlinearities, especially Stimulated Raman Scattering (SRS). The second phase of the project was to improve the performance of the MOPA through active pulse shaping and use of the output in Raman pulse generation in a single mode fiber. The first step was to directly modulate the diode, then an EOM was used to carve the output of the diode to achieve higher extinction ratio, allowing shaping the pulse at higher gain saturation.

Later, a gain-switched diode was also investigated. This diode could be used as a picosecond source for the MOPA. A FROG technique using an Electro-Optic Modulator was built to fully characterise the output of the diode and its compressed pulse.

The project investigates the powerful combination of directly modulated semiconductor lasers in conjunction with amplifier cascades to generate mJ pulses. This allows the output pulses to be tailored to the requirements of specific applications.

The MOPA system comprises a seed source, a preamplifier and a postamplifier. This system allows the small output power of the directly modulated semiconductor diode laser, which provides peak power of a few hundreds of mW, to be amplified with very high gain (total of 50-60dB) to a few tens of kW peak power at the final output.

As a square pulse propagates in a high gain medium, the front of the pulsed is amplified more than the tail leading to distortion of the final output pulse [Wang and Po (2003)]. The distorted pulse develops a sharp leading edge and an exponentially decaying tail such that the front of the pulse is the first place for SRS to occur. This shape can be compensated using a seed pulse with a ramped leading edge such that the final output pulse can be a square pulse with much lower peak power for a fixed pulse energy, and hence lower nonlinear effects.

A fundamental limit of high peak power fiber laser operation arises from nonlinear

effects in silica, especially SRS. The targeted output is operating in single mode regime with a peak power of a few tens of kW. With this high peak power, large mode area fibers must be used in order to limit the generation of SRS in the post-amplification stage. This nonlinear effect is inversely proportional to mode area and proportional to length of the fiber. Therefore, this and other nonlinear effects can be reduced by using as large mode area and as short fiber as possible.

However, as the diameter of the core increases, the number of modes also increases due to the practical lower limit on fiber numerical aperture imposed by bend loss and other perturbations inside the fiber. For example, for an LMA fiber with a 30μm core diameter, and NA of 0.06, there are theoretically about 5 modes that can possibly propagate in the fiber [Snyder and Love (1983)]. High order modes, however, can be suppressed by introducing a large loss differential relative to the fundamental mode through bending at an appropriate radius [Koplow et al. (2000)].

Another way of reducing nonlinear effects is to flatten the fundamental mode by incorporating special features in the refractive index profile. This design can also increase the differential loss between the high order modes and the fundamental mode through bending. However, this technique requires significant investigation in the fabrication process to improve the control of the flatness of refractive index at very small index difference between the core and the cladding.

1.2 Review

The first rare-earth doped fiber lasers pumped by lamp were demonstrated in the early 1960s [Snitzer (1961), Koester and Snitzer (1964)] but after these pioneering efforts by Elias Snitzer work in fiber lasers virtually came to a stop due to the lack of suitable pump sources. This early work focused on Nd-doped silica fiber lasers operating at 1.06μm. However, rapid developments in fiber laser technology have only taken place since 1986 after the demonstration of practical Erbium doped fibers suitable for single-mode diode pumping and has been driven primarily by the need for low power efficient Er^{3+} amplifiers operating at the low loss telecommunication window [Mears et al. (1986)]. The next significant step forward in the development of fiber laser technology was the introduction of cladding pumping in 1988, again led by Snitzer [Snitzer et al. (1988)]. This technique led to a rapid increase in fiber laser power over the following decade: 2W in 1995 [Pask et al. (1995)], 20W in 1997 [Inniss et al. (1997)] and 35W in 1997 [Muendel et al. (1997)],

110W in 1999 [Dominic et al. (1999)], 1.3kW by Jeong et al. (2004) and kW cw commercial lasers have now been commercially developed.

Along with the development of cw lasers, short pulse high power Yb-doped double-clad fiber lasers have also been intensively investigated. Several mJ Q-switched Yb-doped fiber lasers have been developed over the past few years. In 2001, Renaud et al. (2001) reported multimoded output with a pulse energy of 7.7mJ for pulse durations of 300ns. Piper et al. (2004) produced near diffraction limit output with a pulse energy of 1.2mJ at 40ns pulse duration using a few-moded LMA fiber. The performance of this Q-switch nanosecond pulse source is beginning to be comparable to that of that of certain conventional solid-state lasers and is compatible with many industrial processing applications.

Ultrashort pulse generation using LMA fiber through Chirped Pulse Amplification (CPA) has attracted significant research in recent years because of its large number of applications. In the CPA technique, the femtosecond seed pulse is stretched before launched into the amplifiers to reduce nonlinear distortions in the fibers, the final output is then recompresed to the original pulse duration. Galvanauskas et al. (2001) demonstrated a 50μm-core Yb-fiber CPA that produced 380fs pulses with energies of 1.2mJ. Malinowski et al. (2004) reported a single mode operation of a parabolic amplifier system using 40μm core that produced a pulse energy of 400nJ at pulse duration of 110fs and repetition rate of 62MHz (25W average power, >3MW peak power).

Single mode operation of nanosecond regime amplifiers using Yb-doped LMA fibers has also been developed. Koplow et al. (2000) realised single mode operation of a bent multiple mode fiber in a cw amplifier configuration. In their experiment, an LMA fiber with a V number of 7.4 was coiled with a diameter of 1.58cm, the output was in a single mode with M^2 of 1.09. Later, pulsed operation in similar conditions gave single mode output with a pulse energy of 255μJ, peak power of 300kW with a pulse duration of 0.8ns (FWHM) [Di Teodoro et al. (2002)]. Limpert et al. (2002) demonstrated a Yb-doped high energy nanosecond fiber amplifier that is capable of producing 100W average power with 2mJ pulse energy (50kHz repetition and 90ns pulse duration) or 15W average power with 4mJ pulse energy (3kHz repetition rate, 90ns pulse duration) at near diffraction limited output. Avila et al. (2004) has reported a nanosecond regime polarisation maintaining LMA Yb-fiber MOPA producing near single mode output with a pulse energy of 200μJ at a pulse duration of 0.8ns, and a repetition rate of 13kHz. More recently, Di Teodoro and Brooks (2005) reported a MOPA systems operating at 1062nm, 1-ns pulse and 10kHz

repetition rate, which generated diffraction-limited pulses of energy $> 1mJ$, peak power $> 1MW$, average power of $> 10W$ and spectral linewidth ∼9GHz. On the theoretical side, a numerical model of nanosecond high-power Yb-doped double-clad pulse amplifiers has also been reported and used to analyze a range of nanosecond fiber amplifier systems very recently [Wang and Po (2003), Wang (2005a), Wang (2005b)].

1.3 Thesis Summary

This thesis is structured in a total of 8 chapters. Chapter 2 gives some back ground information on the basic principle of Yb-doped amplifiers and nonlinear effects in high power amplifiers focusing in particular on Stimulated Raman Scattering. Chapter 3 investigates some large mode fibers that can be used in high power amplifiers. The quality of the signal in the core is determined in detail for various fiber structures. Chapter 4 gives the detailed performance of an all-fiber MOPA with preamplifier and postamplifier in GTWave format. Raman spectra and pulse shape at the output of this MOPA are measured and described in Chapter 5. Chapter 6 deploys an active pulse shaping method by directly modulated the electrical signal sent to the seed diode. Chapter 7 further develops pulse shaping technique using an EOM, then uses the square pulse at the output to generate individual Raman order components. Finally, Chapter 8 investigates the performance of a gain-switched diode under both injection and self seeded operation. Also, in this chapter the EOM is used as a gate in a FROG technique, allowing me to fully characterise the output of the diode and its compressed pulse.

Chapter 2

Background Theory

2.1 Introduction

In this chapter, a brief review of the fundamental science behind Ytterbium doped silica fiber amplifiers is described. First, relevant spectral properties of Ytterbium ions in silica are reviewed. Then, pumping schemes for double clad and GTWave fibers are described. The amplifier operation is looked into in detail through the rate equations, and the resulting pulse shaping in a highly saturated amplifier is described and analysed. Finally, the Stimulated Raman Scattering is discussed.

2.2 Ytterbium Doped Silica Fiber

Ytterbium is one of the most versatile laser ions in a silica-based host. It offers several very attractive features, in particular an unusually broad absorption band that stretches from below 850nm to above 1070nm associated with the $^2F_{7/2} \rightarrow {}^2F_{5/2}$ transition. The absorption and emission spectrum is illustrated in Figure 2.1 . The energy level structure of the Yb^{3+} ion is simple compared to other rare-earth ions, consisting of only two relevant manifolds: the ground state $^2F_{7/2}$ (with 4 Stark levels) and a metastable state $^2F_{5/2}$ spaced by approximately 10000cm^{-1} [Hanna et al. (1990)]. The radiative lifetime of the $^2F_{5/2}$ state is typically in the range 700-1400μs, depending on the host [Digonnet (2001)].

The transitions between sublevels are not fully resolved for Yb^{3+} ions in a glass at room temperature due to strong homogenous broadening, although weaker inhomogeneous broadening is also observed as the emission spectra vary to some extent with pump wavelength. It is important to note that the detailed absorption and emission spectra depend to some extent on the host glass composition [Paschotta et al. (1997)]. The cross sections of Yb-doped germanosilicate fibers as shown in Figure 2.1 vary up to about 30% depending on the different content of germanium, aluminum and boron. The measured

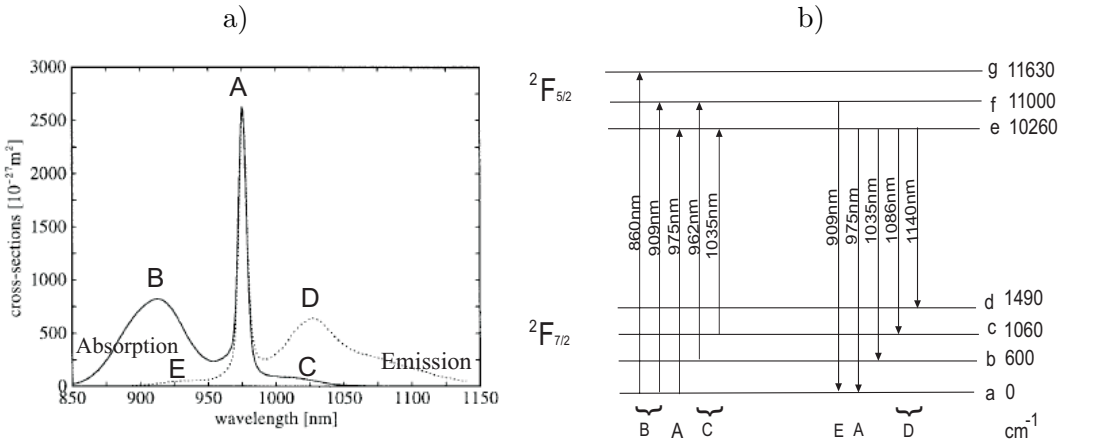

Figure 2.1: Ground-state absorption spectrum (solid line), emission spectrum (dotted line) and energy level diagram of Yb^{3+} in silica (From Ref. Paschotta et al. (1997) and Pask et al. (1995)).

fluorescence decay times of typically around 0.8ms also vary by about 30%. A higher content of germanium tends to decrease the lifetime of the excited state. Yb^{3+} in pure silicate glass has a lifetime of around 1.5ms. The value of the lifetime is important in this tens of kHz repetition rate MOPA system as it directly influences the amount of ASE produced.

Yb-doped silica fibers are excellent media for high power lasers and amplifiers. The absence of higher energy levels greatly reduces the effect of multi-phonon relaxation and Excited State Absorption (ESA). Yb^{3+} in silica also has much higher absorption and emission cross sections than multi-component glasses [Digonnet (2001), Suni et al. (1990)]. Furthermore, cooperative up-conversion, a process in which two near neighbour Yb^{3+} ions combine their excitation energy to emit a single photon in the green region of the spectrum, is very small even in strongly doped fibers (e.g., 10000ppm by weight) [Paschotta et al. (1997)]. This combination of advantages allows very high pump absorption and very short fiber lasers.

2.3 Large Mode Area Fibers

The obvious way to increase the energy storage and reduce the nonlinearity of single-mode fibers is to increase the fiber mode area. Scaling of fiber mode field area in single-mode fibers is ultimately limited by two factors [Broderick et al. (1999)]. First, the accuracy with which one can reliably control the index difference between core and cladding, which defines the maximum core dimension that supports pure single-mode guidance. The second limit is imposed by the fiber bend loss which increases rapidly with increasing mode field

area. Therefore, the maximum core size that rigorously supports just a single transverse mode is significantly constrained by physical limitations.

A single mode fiber requires to have a V parameter of less than 2.54; $V = (2\pi/\lambda).a.NA$, where a is core radius and $NA = \sqrt{n_{core}^2 - n_{cladding}^2}$ is numerical aperture. A standard single mode fiber at 1060nm has a core diameter of about 6μm and and NA of 0.1.

In practice, typical LMA fibers have diameters in the range of 20-40μm with numerical apertures of around 0.06 at $\lambda = 1\mu$m. These fibers can support 4 to 6 modes depending on the exact index profile. Therefore, it is necessary to employ specific techniques to achieve single mode operation of amplifiers using these fibers. There are two ways to preferentially excite the fundamental mode. The first is to selectively dope the core to give preferential gain to the fundamental mode [Broderick et al. (1999), Broderick et al. (1998)]. The second approach is to bend the fibers such that the bend loss of the fundamental mode is minimum while the bend loss for higher orders mode is high compared with their gains [Koplow et al. (2000), Di Teodoro et al. (2002)]. These two approaches can also be combined.

2.4 Double-Clad and GTWave Pump Schemes

Initially, fiber lasers and amplifiers were simple structures with a single core for guiding both the signal and the pump light. This requires single-mode pump diodes. However, the limited power of single-mode pump sources has restricted the output powers to ∼1W for core pumped systems. Consequently, cladding-pumping has been developed as a method to overcome this limitation [Snitzer et al. (1988)]. Cladding-pumped fiber lasers and amplifiers do not require single-mode pump sources, but can still produce a single mode laser output. A double clad fiber (DCF) has a core for guiding the signal, surrounded by a lower-index inner cladding, then a low index outer cladding. A schematic drawing of a double clad fiber is shown in Figure 2.2 a). Both the core and the inner cladding are made from glass, however the core is doped with active laser ions. The undoped-outer cladding is normally made from low index polymer or glass.

In principle an arbitrarily large amount of pump power can be launched if no restriction is made on the size of the inner cladding. However, the total length of the fiber used in an amplifier or a laser is an important factor and this is determined largely by the ratio of the core and inner cladding dimension. With a fixed core size, a reasonable inner cladding size has to be calculated so that the absorption per unit length gives a suitable total device length.

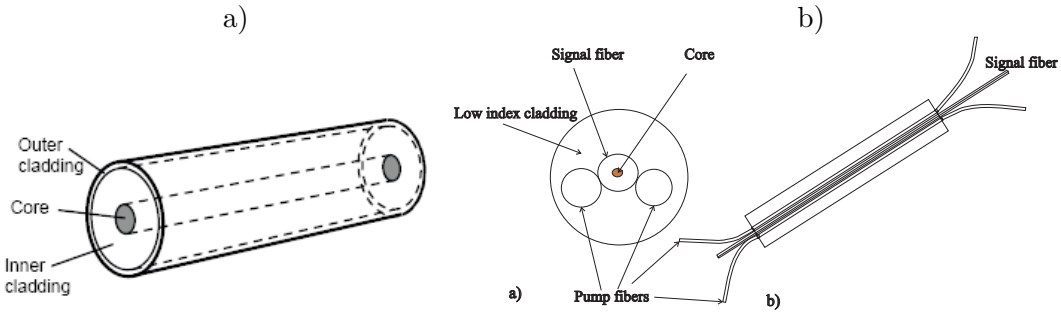

Figure 2.2: Schematic of a) double-clad fiber and b) GTWave fiber.

The mode profile within the fiber is not uniform and might follow the profile of a Gaussian beam for a single mode fiber. If the distribution of light intensity at a wavelength λ over the radial and azimuthal coordinates is given by $I_\lambda(r, \phi, z)$ the total power of the beam $P_\lambda(z)$ at the position z in the fiber amplifier is given by

$$P_\lambda(z) = \int_0^{2\pi} \int_0^{\infty} I_\lambda(r, \phi) r dr d\phi \tag{2.1}$$

The radial and azimuthal dependence of intensity make the calculation process much more complicated than the plane wave approximation. However, the intensity variation can be averaged out so that the average intensity in the fiber can be used for calculation. In the literature, the analysis of the performance of double clad fiber amplifiers and lasers is simplified by the introduction of an overlap integral Γ between the doped region and optical mode profile [Giles and Desurvire (1991), Barnard et al. (1994)]. The overlap integral can vary from zero (no overlap of intensity and doping profile) to one (exactly overlap) and can be generally calculated by:

$$\Gamma_n = \frac{A^d_{eff} \int_0^{2\pi} \int_0^{\infty} I_n(r, \phi) N_t(r, \phi) r dr d\phi}{\int_0^{2\pi} \int_0^{\infty} I_n(r, \phi) r dr d\phi \int_0^{2\pi} \int_0^{\infty} N_t(r, \phi) r dr d\phi} \tag{2.2}$$

where $N_t(r, \phi)$ is local total density of Yb^{3+} ions, $n = s$ for signal, $n = p$ for pump and effective doped area of $A^d_{eff} = \pi b^2$. In a core-pump fiber amplifier or laser, the pump and signal have similar value of overlap integral. However, in cladding-pump fiber amplifier the laser pump is guided in a multimode inner-cladding and only signal and ASE are guided in the core of the fiber. Therefore, the value of Γ_s, and Γ_p, are very different. For a fundamental mode approximated by a Gaussian profile with $I = (2P/\pi w^2 exp(-2r^2/w^2))$, the overlap of the mode with a uniform total ion profile N_t and with a radius of b is given

by Barnard et al. (1994):

$$\Gamma_t = 1 - e^{-2b^2/w^2} \tag{2.3}$$

For example, for a fiber with core of 30μm and cladding of 200μm, the typical value for $\Gamma_s \approx 0.8$, and $\Gamma_p \approx 0.05$.

The double clad structure as described above requires precise alignment of the signal when it is launched into the core. The setup arrangement is bulky and requires lenses and dichroic mirrors, and is quite lossy. An ingenious alternative technique was developed by Dr. Anatoly Grudinin and Paul Turner at the ORC called GTWave as shown in Figure 2.2 b). A fiber with a doped core is held in contact with pure silica dummy fibers, encased together in a low refractive index polymer outer cladding. The fiber pigtailed pump diodes are spliced directly to the dummy fibers and the input signal is spliced to the signal fiber using standard splicers. The pump power is transferred across to the doped fiber and absorbed as it propagates along the GTWave. There is almost no loss of the signal and the pump power due to launching. Furthermore, this technique avoids the injection of large amount of power into a small spot that can lead to fiber damage. A disadvantage of this structure is that it normally requires longer fiber to achieve the same level of pump absorption compared to a DCF because the overlap factor of the pump with doped area is generally smaller than in a DCF and the pump radiation needs to travel a distance to diffuse from the dummy fibers to the fiber with the core.

2.5 Long Pulse Propagation in Amplifier

In this section, a simple treatment of a long pulse propagation in a high gain medium will be analysed. It will help to understand the pulse propagation in the highly saturated cascaded amplifier. When an infinitesimal width pulse propagates in a high gain laser medium, which has uniform inversion along its length, the pulse grows exponentially with distance. However, if the width of the pulse is appreciable, one must take into account the fact that its tail sees a population which has been altered by its leading part. In this case, the amplification process is more complicated and must be described by nonlinear time-dependent radiation transfer equation [Frantz and Nodvik (1963), Siegman (1986) Chapter 10 and Chinn (1998)].

General Rate Equations

In a typical pulse fiber laser amplifier, a diode pump is used to invert the population of the Yb^{3+} in the fiber. A pulse signal source with a certain pulse duration and repetition rate is seeded at point z=0. There can be forward, backward or bidirectional pumping schemes. During the time between the two successive pulses, there is no seeded signal, the inverted population is continuously built up as time increases. The absorption cross section of the pump can be called σ_{ap}. At the same time, there will be down conversion from the upper state to ground state through pump stimulated emission and excited state spontaneous emission. The cross sections of pump stimulated emission is labelled σ_{ep}. The spontaneous emission rate is labelled γ or half lifetime $\tau = 1/\gamma$. In a very high gain amplifier, the spontaneous emission can be amplified when it is captured by the fiber core. This can result in amplified spontaneous emission (ASE) which extracts the population inversion to produce a continuous broad spectrum beam inside the fiber. When the next pulse arrives, the population inversion is then converted to the signal pulse though stimulated emission of the signal, at the same time it is also absorbed by the ground state in the signal stimulated absorption process. The cross sections for the two signal interactions are labelled σ_e and σ_a, respectively. Figure 2.3 shows the energy levels and the interaction between excited state and ground state in the presence of pump and signal light. The population densities of atoms at the two level are N_1 and N_2

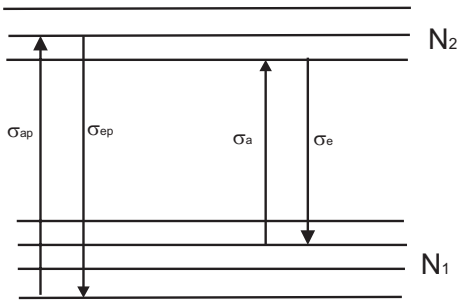

Figure 2.3: Energy band diagram with pump and signal interactions with Yb^{3+}

As long as ASE does not extract a large amount of power and purely homogenous broadening is assumed, then the rate equation of the Yb excited state and ground state population can be simply written in the form [Paschotta et al. (1997)]:

$$\frac{dN_2}{dt} = (\frac{\sigma_{ap}\Gamma_p I_p}{\hbar\omega_p} + \frac{\sigma_a\Gamma_s I_s}{\hbar\omega_s})N_1 - (\frac{\sigma_{ep}\Gamma_p I_p}{\hbar\omega_p} + \frac{\sigma_e\Gamma_s I_s}{\hbar\omega_s} + \gamma)N_2 \tag{2.4}$$

$$\frac{dN_1}{dt} = -(\frac{\sigma_{ap}\Gamma_p I_p}{\hbar\omega_p} + \frac{\sigma_a\Gamma_s I_s}{\hbar\omega_s})N_1 + (\frac{\sigma_{ep}\Gamma_p I_p}{\hbar\omega_p} + \frac{\sigma_e\Gamma_s I_s}{\hbar\omega_s} + \gamma)N_2. \tag{2.5}$$

The gain and loss for pump and signal at a given position z along the fiber is given by the equations:

$$\frac{dI_p}{dz} = \Gamma_p(\sigma_{ep}N_2 - \sigma_{ap}N_1)I_p \tag{2.6}$$

$$\frac{dI_s}{dz} = \Gamma_s(\sigma_e N_2 - \sigma_a N_1)I_s. \tag{2.7}$$

Analysis of Long Pulse Amplification in a Laser Medium

For the MOPA in this particular project, the amplifiers are continuously pumped by diodes operating at 915nm, the signal source is a directly modulated diode operating at 1077nm, the pulse duration can be varied in the range from 20ns to 2000ns, and a repetition rate of 20kHz is normally applied. The delay time between two successive pulses is 50μs. The length of the power amplifier is around 7m. The lifetime of the excited state is around 1ms. From these numbers it is reasonable to assume that during the time the pulses travel in the amplifier, the additional build up of the excited state due to the pump is negligible, and the amount of ASE is very small. Figure 2.1 shows that the value of the emission cross section at 1080nm is much larger than that of the absorption cross section. Therefore, during the time the pulse travels through the laser medium, only the cross section of the signal is taken into account.

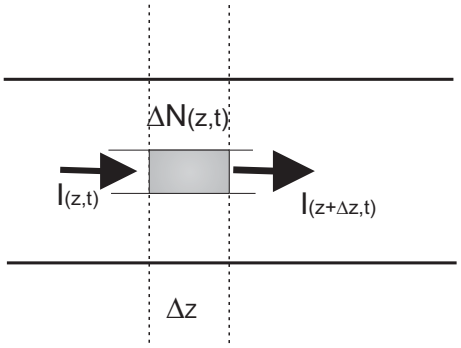

Figure 2.4: Optical amplification in laser medium

The following analysis is based on Siegman (1986) and Frantz and Nodvik (1963). We can consider a short pulse with signal intensity $I(z,t)$ traveling in the +z direction through a laser medium with inverted population density $\Delta N(z,t) = N_2(z,t) - N_1(z,t)$. Considering a short segment of length Δz in the laser medium as shown in Figure 2.4.

The photon transport equation are then [Siegman (1986) page 364]

$$\frac{\partial I(z,t)}{\partial t} + v\frac{\partial I(z,t)}{\partial z} = \sigma_e \Gamma_s \Delta N(z,t) I(z,t) \tag{2.8}$$

and

$$\frac{\partial \Delta N(z,t)}{\partial t} = -\frac{\sigma_e \Gamma_s}{\hbar\omega} \Delta N(z,t) I(z,t) \tag{2.9}$$

where v is speed of light in the fiber and ω is the angular frequency of the signal light.

The two basic Equations 2.8 and 2.9 can be solved with the aid of a transformation

$$\hat{z} = z \qquad \text{and} \qquad \hat{t} = t - z/v. \tag{2.10}$$

The new coordinate system moves with the forward travelling pulse. In this new coordinate system, the pulse is essentially stationary in time, the gain medium moves at speed v. Note that the delayed time coordinate $\hat{t}$ is centered on the pulse's arrival time at each plane z. For instance, if the pulse starts out at an input plane $z = 0$ centered at time $t = 0$, and arrives at some plane z centered at time $t = z/v$, then the pulse written in the delayed time coordinate $\hat{t}$ is centered on $\hat{t} = 0$ at every plane along the amplifier.

We can now rewrite the two Equations 2.8 and 2.9 as

$$\frac{\partial \hat{I}(\hat{z},\hat{t})}{\partial \hat{z}} = \sigma_e \Gamma_s \Delta \hat{N}(\hat{z},\hat{t}) \hat{I}(\hat{z},\hat{t}) \tag{2.11}$$

$$\frac{\partial \Delta \hat{N}(\hat{z},\hat{t})}{\partial \hat{t}} = -\frac{\sigma_e \Gamma_s}{\hbar\omega} \Delta \hat{N}(\hat{z},\hat{t}) \hat{I}(\hat{z},\hat{t}) \tag{2.12}$$

where these equations are now expressed in the transformed or moving coordinate at the speed of light in the fiber. From this point on the algebra will originate only from Equation 2.11 and 2.12, therefore, for simple typing the hat ($\hat{}$) is now removed.

Equation 2.11 can be integrated and gives

$$\int_{I=I_{in}(t)}^{I=I_{out}(t)} \frac{dI}{I} = \sigma \Gamma_s \int_{z=0}^{z=L} \Delta N(z,t) dz \tag{2.13}$$

where, $I_{in}(t)$ is the input pulse intensity profile at the point $z = 0$, and $I_{out}(t)$ is the corresponding signal intensity profile at the output plane z=L both measured in the delayed time coordinate t.

The solution can be written in the form:

$$I_{out}(t) = I_{in}(t)e^{\sigma\Gamma_s N_{tot}(t)} = G(t)I_{in}(t) \tag{2.14}$$

where $N_{tot}(t) = \int_{z=0}^{z=L} \Delta N(z,t)dz$ represents the total population inversion per area in the amplifier at time t and $G(t) = e^{\sigma\Gamma_s N_{tot}(t)}$ is the time-varying gain at any instant within the pulse.

Equation 2.12 then now can be rewritten as

$$\frac{\partial}{\partial t}\int_{z=0}^{z=L} N(z,t) = \frac{dN_{tot}(t)}{dt} = -\frac{1}{\hbar\omega}\int_{z=0}^{z=L}\frac{\partial I(z,t)}{\partial z}dz \tag{2.15}$$

which is equivalent to

$$\frac{dN_{tot}(t)}{dt} = -\frac{1}{\hbar\omega}[I_{out}(t) - I_{in}(t)]. \tag{2.16}$$

Substituting Equation 2.14 into Equation 2.16 we have either of the alternative form

$$\begin{aligned}\frac{dN_{tot}(t)}{dt} &= -\frac{1}{\hbar\omega}[e^{\sigma\Gamma_s N_{tot}(t)} - 1]I_{in}(t) \\ &= -\frac{1}{\hbar\omega}[1 - e^{-\sigma\Gamma_s N_{tot}(t)}]I_{out}(t)\end{aligned} \tag{2.17}$$

At this point it is necessary to introduce some additional parameters. Suppose the total initial inverted population density N_0 in the laser medium at the real time $t_0 = 0$ prior to the arrival of any input pulse energy is given by

$$N_0 = \int_{z=0}^{z=L} N(z, t=0)dz \tag{2.18}$$

The initial single-pass power gain of the amplifier is then $G_0 = e^{\sigma\Gamma_s N_0}$.

We can also write the accumulated signal energies per unit area $U_{in}(t)$ and $U_{out}(t)$ in the input and output pulses, from the starting time t_0 up to the normalised time t as

$$U_{in}(t) = \int_{t_0}^{t} I_{in}(t)dt \qquad \text{and} \qquad U_{out}(t) = \int_{t_0}^{t} I_{out}(t)dt \tag{2.19}$$

It is also convenient to define a saturation energy per unit area U_{sat} as

$$U_{sat} = \frac{\hbar\omega}{\sigma\Gamma_s} \tag{2.20}$$

The first line of Equation 2.17 can be then integrated in the form

$$\int_{N_0}^{N_{tot}} \frac{dN_{tot}}{e^{\sigma\Gamma_s N_{tot}} - 1} = -\frac{1}{\hbar\omega}\int_{t_0}^{t} I_{in}(t)dt = -\frac{1}{\hbar\omega}U_{in}(t) \tag{2.21}$$

to give the useful relation

$$U_{in}(t) = U_{sat}ln[\frac{1 - e^{-\sigma\Gamma_s N_0}}{1 - e^{-\sigma\Gamma_s N_{tot}}}] = U_{sat}ln[\frac{1 - 1/G_0}{1 - 1/G(t)}] \tag{2.22}$$

The second line of Equation 2.17 gives

$$U_{out}(t) = U_{sat}ln[\frac{e^{\sigma\Gamma_s N_0} - 1}{e^{\sigma\Gamma_s N_{tot}} - 1}] = U_{sat}ln[\frac{G_0 - 1}{G(t) - 1}] \tag{2.23}$$

Gain Saturation

Equation 2.22 can be rewritten in the form

$$\sigma N_{tot}(t) = ln[\frac{G_0}{G_0 - (G_0 - 1)e^{-U_{in}(t)/U_{sat}}}] \tag{2.24}$$

which gives

$$G(t) = e^{\sigma\Gamma_s N_{tot}(t)} = \frac{G_0}{G_0 - (G_0 - 1)e^{-U_{in}(t)/U_{sat}}} \tag{2.25}$$

For a given input pulse shape $I_{in}(t)$ and a given initial gain (small signal gain) G_0 we can use this equation to calculate the output pulse shape $I_{out}(t) = G(t)I_{in}(t)$. Alternatively, the output pulse shape $I_{out}(t)$ can be specified and the gain can be calculated as

$$G(t) = 1 + (G_0 - 1)e^{-U_{out}(t)/U_{sat}} \tag{2.26}$$

and the input pulse shape from $I_{in}(t) = I_{out}/G(t)$. The value of initial gain G_0 must be calculated using the data from the fiber properties and pump power level.

2.6 Pulse Reshaping in High Gain Laser Medium

This section considers some special cases of pulse distortion by amplifier gain saturation assuming some typical input pulse shapes of square and Gaussian pulses. In this section the practical value of pulse energy $E(t)$ is used instead of the energy per unit area $U(t)$.

The relation between these parameters can be written in simple linear equation

$$E(t) = \int_{t_0}^{t} A_{eff} I(t) dt = A_{eff} U(t) \tag{2.27}$$

where A_{eff} is the effective mode area of the fiber.

For the special case of a square input pulse, the output pulse shape can be calculated using Equation 2.26. Figure 2.5 a) illustrates the case where the input power is large $G_0 E_{in} \gg E_{sat}$. The pulse is greatly distorted with a spike on the leading edge of the pulse. Then the power drops significantly at the tail of the pulse to a power that is much lower than the peak power. The pulse duration at full width half maximum (FWHM) is substantially reduced to about 10ns from the original width of 100ns. The instantaneous gain $G(t)$ follows the exact shape of the output pulse in this case.

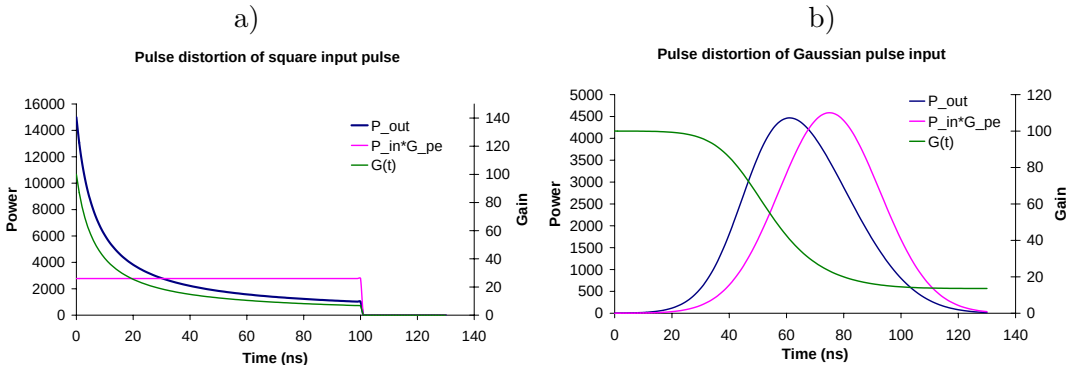

Figure 2.5: Reshaping of a) square pulse and b) Gaussian pulse input with $G_0 = 100 = 20dB$, and $E_{sat} = 0.1$mJ, energy gain a)$G_{pe} = 18.5 = 12.7$dB and b) $G_{pe} = 30 = 14.8$dB

In the case of a Gaussian pulse or any other shape with a rounded leading and trailing edge, the output pulse appears to be very little changed even under significant saturation effects as shown in Figure 2.5 b). Hence the pulse duration remains practically the same. Although the pulse does seems to move forward slightly in time. The pulse is not really advanced in time, but merely appears so because the leading edge receives essentially full amplification, whereas the gain is significantly reduced during the peak and trailing edge of the pulse.

Pulse Energy Extraction and Energy Gain

In pulse amplifiers, each pulse can only extract a limited portion of the power stored in the fiber. The amount of power extracted by one pulse is measured by

$$E_{extr} = E_{out} - E_{in} = E_{sat} ln \frac{G_0}{G_f} \tag{2.28}$$

where G_f is the residual gain at the end of the pulse and

$$E_{sat}(t) = \frac{A_{eff}\hbar\omega}{\sigma\Gamma_s} \tag{2.29}$$

The maximum amount of energy from the amplifier is obtained when the residual gain is saturated all the way down to $G_f = 1$. Hence, the maximum available energy that can be extracted from the amplifier, assuming an input pulse is strong enough to completely saturate the initial inversion is given by

$$E_{avail} = E_{sat} ln G_0 = A_{eff}\hbar\omega N_0 \tag{2.30}$$

The above expression confirms the physically obvious result that the available energy from the amplifier is the total initial inversion energy stored in the fiber before the pulse enters the amplifier.

The overall energy or pulse-averaged gain $G_{pe} = E_{out}/E_{in}$ can also be also calculated through the expression

$$G_{pe} = \frac{E_{out}}{E_{in}} = \frac{U_{out}}{U_{in}} = \frac{ln[(G_0 - 1)/(G_f - 1)]}{ln[(G_0 - 1)/(G_f - 1)] - ln[G_0/G_f]} \tag{2.31}$$

The two values of G_{pe} in examples in Figures 2.5 a) and 2.5 b) are 12.7dB and 14.8db, which are obviously much smaller than the initial gain G_0 of 20dB and 30dB, respectively.

2.7 Nonlinear Effects in Optical Fiber

The response of a dielectric to light becomes nonlinear for intense electromagnetic fields. The high peak intensity within the amplifier is no exception. The origin of the nonlinear response is related to anharmonic motion of bound electrons under the influence of an applied field. The total polarisation **P** induced by the electric field is not linear with

electric field **E** but follows a more general relation

$$\mathbf{P} = \epsilon_0(\chi^{(1)}.\mathbf{E} + \chi^{(2)} : \mathbf{EE} + \chi^{(3)}\vdots\mathbf{EEE}) \tag{2.32}$$

where ϵ_0 is the vacuum permittivity and $\chi^{(j)}$(j=1,2,3...) is the j^{th} order susceptibility. The linear susceptibility provides the dominant contribution to **P**, and its effects are included through the refractive index n, and the attenuation coefficient α. The second-order susceptibility $\chi^{(2)}$ is responsible for second-harmonic generation, sum-frequency generation and difference frequency generation. However, centro-symmetric materials such as SiO_2 show a zero value of $\chi^{(2)}$. Therefore, silica fiber does not exhibit second-order nonlinear effects. The lowest-order nonlinear effects in optical fibers originate from the third order susceptibility $\chi^{(3)}$, which is responsible for phenomena such as third-harmonic generation, four-wave mixing, and nonlinear refraction. The nonlinear processes that involve phase matching to generate new frequencies such as in third-harmonic generation and four-wave mixing are generally not efficient in optical fiber unless attention is paid to the fibers dispersion properties, therefore, they are ignored. Most of the nonlinear effects in an optical fiber therefore originate from nonlinear refraction.

Nonlinear Refractive Index

In its simplest form, the refractive index can be written as

$$n(\omega, E) = n(\omega) + n_2|E|^2 = n(\omega) + n_2 I \tag{2.33}$$

where $n(\omega)$ is the linear part given by the Sellmeier equation:

$$n^2(\omega) = 1 + \sum_{j=1}^{m} \frac{B_j \omega_j^2}{\omega_j^2 - \omega^2} \tag{2.34}$$

with ω_j is the resonance frequency and B_j is the strength of the j^{th} resonance; $|E|^2$ is the optical intensity inside the fiber; and n_2 is the nonlinear-index coefficient (Kerr nonlinearity coefficient) related to $\chi^{(3)}$ by the relation

$$n_2 = \frac{3}{8n} Re(\chi^{(3)}_{xxxx}). \tag{2.35}$$

The value of n_2 in silica fiber is about $2.5 \times 10^{-20} m^2/W$. The intensity dependence of the refractive index leads to a large number of interesting nonlinear effects. The two most

widely looked at are self-phase modulation (SPM) and cross phase modulation (XPM). Self-phase modulation refers to the self-induced phase shift experienced by an optical field during its propagation in optical fibers. Cross-phase modulation refers to the nonlinear phase shift of an optical field induced by another field having a different wavelength, direction, or state of polarisation.

Stimulated Inelastic Scattering

Another important nonlinear process in optical fiber is stimulated inelastic scattering. The stimulated inelastic scattering again is governed by the third-order susceptibility. In silica fibers, there are two main nonlinear processes that limit the peak power: Stimulated Brillouin Scattering (SBS) and Stimulated Raman Scattering (SRS)[Agrawal (2001)]. In pulse fiber amplifiers, the amplified signal becomes the pump for these nonlinear processes.

SBS originates from scattering of photons with acoustic phonons resulting in a frequency shift. The peak value of the gain occurs for the Stokes shift of $\approx 10GHz$ (4×10^{-2}nm) at 1060nm. The peak gain for silica is $\approx 6 \times 10^{-11}$m/W. However, the SBS gain spectrum has an extremely narrow gain bandwidth of only $< 100MHz$ (4×10^{-4}nm) at 1060nm. The peak gain decreases by a factor of $\delta\nu_p/\delta\nu_B$ for a broad-bandwidth pump, where $\delta\nu_p$ is the pump bandwidth and $\delta\nu_B$ is the Brillouin-gain bandwidth. For a bandwidth of 3nm, the effective SBS gain coefficient is reduced by $\approx 10^4$. Therefore, for a large bandwidth pump, the effect of SBS is not observed.

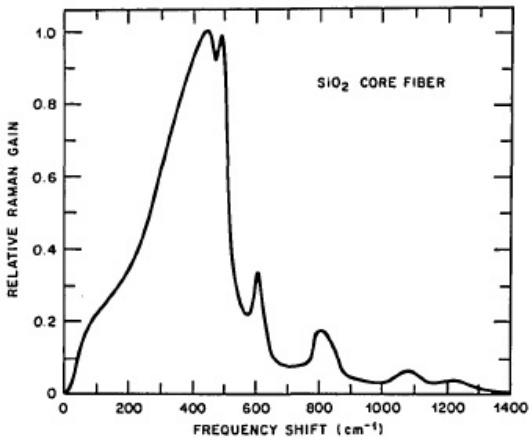

Figure 2.6: Raman gain curve of a silica-core single-mode fiber. This curve is normalized to 1.0 at 440 cm^{-1}. The peak gain at 440 cm^{-1} for a pump wavelength of 532 nm is 1.86×10^{-13} m/W and varies with pump wavelength as $1/\lambda$ (from Ref. Stolen and Lee (1984)).

On the other hand, SRS originates from scattering of photons by optical phonons, the Raman gain spectrum is very broad, extending out to 30THz (112nm) with a peak shift

in frequency of 13THz (48nm) at 1060nm. The peak gain of SRS is $g_R \approx 10^{-13}$m/W at a pump wavelength of 1μm. Figure 2.6 shows the Raman-gain spectrum for fused silica. This figure shows the coefficient for fused silica as a function of the frequency shift at a pump wavelength $\lambda_p = 0.526\mu$m, however, for other wavelengths g_R can be obtained by using the inverse dependence of g_R on λ_p. The spontaneous Raman scattering generates photons within the entire range of the gain spectrum, all frequency components are amplified. However, the frequency component at which g_R is maximum builds up most rapidly. It turns out that when the pump power exceeds a threshold value, this component builds up almost exponentially. As a results, the pump is quickly converted into the Raman Stokes. SRS is the main barrier preventing high peak powers to be obtained in optical fibers within the nanosecond regime. It is possible to estimate the value of the SRS threshold and hence the maximum achievable peak power in a fiber amplifier.

2.8 Stimulated Raman Scattering

Coupled Equations

To find the Raman threshold the nonlinear interaction between the pump and Stokes waves should be considered. Assuming a CW or long pulse light travelling in a fiber amplifier with a constant gain coefficient along its length. The signal of the amplifier now acts also as the pump for the SRS Stokes wave. In the CW or quasi-CW case (ie. a pulse duration of more than 1ns), the walk off length L_W generally exceeds the fiber length L, therefore, the interaction can be consider instantaneous and is governed by the following set of equations [Agrawal (2001)]:

$$\frac{dI_s}{dz} = g_R I_p I_s + \alpha_s I_s \tag{2.36}$$

$$\frac{dI_p}{dz} = -\frac{\omega_p}{\omega_s} g_R I_p I_s + \alpha_p I_p \tag{2.37}$$

where α_s and α_p are the total constant fiber gain (or loss, a positive value for gain and negative for loss) at the Stokes and pump frequencies, respectively. The pump deletion must be included for a complete description of SRS, however, it can be neglected for the purpose of estimating the Raman threshold. The pump can then be expressed simply as

$$\frac{dI_p}{dz} = \alpha_p I_p \tag{2.38}$$

or

$$I_p(z) = I_p(0)e^{\alpha_p z} \tag{2.39}$$

where $I_P(0)$ is the the incident pump intensity at z=0. Then Equation 2.36 can be easily solved and the result is written as

$$I_s(L) = I_s(0)e^{[g_R I_P(0) L_{eff}(0) + \alpha_s L]} \tag{2.40}$$

where L is the length of the fiber and

$$L_{eff}(0) = \frac{e^{\alpha_p L} - 1}{\alpha_p}. \tag{2.41}$$

is the Raman effective length.

Equation 2.40 can be also expressed in terms of the output power of the pump at the point L using expression 2.39 to give

$$I_s(L) = I_s(0)e^{[g_R I_P(L) L_{eff}(L) + \alpha_s L]} \tag{2.42}$$

where

$$L_{eff}(L) = \frac{1 - e^{-\alpha_p L}}{\alpha_p}. \tag{2.43}$$

In a real system, the pump for SRS (which is also the signal of the amplifier) does not usually have a constant gain coefficient along the amplifier because the amplifier pump power is inserted at the ends of the fiber accordingly to either a forward, backward or bidirectional scheme. The fiber amplifier gain coefficient at the point of pump entrance will be highest then exponentially reduces with the rate of pump absorption. Figure 2.7a) shows an example of how the pump power is distributed in a high gain amplifier with a length of 7m, a pump absorption of 2dB/m, an input peak power of 150W and a total signal gain of 20dB. Figure 2.7 b) shows the calculated SRS effective length within the fiber as a function of power signal gain in the amplifier for the forward and backward pumping schemes. The effective length in the case of the backward pumping case is much smaller that that of the forward pumping. For instance at 20dB gain, the difference is by a factor 4 times. It is obvious from these figures that the backward pumping scheme is preferable as the nonlinear effect will be much smaller even though the output power of the signal is the same for both cases.

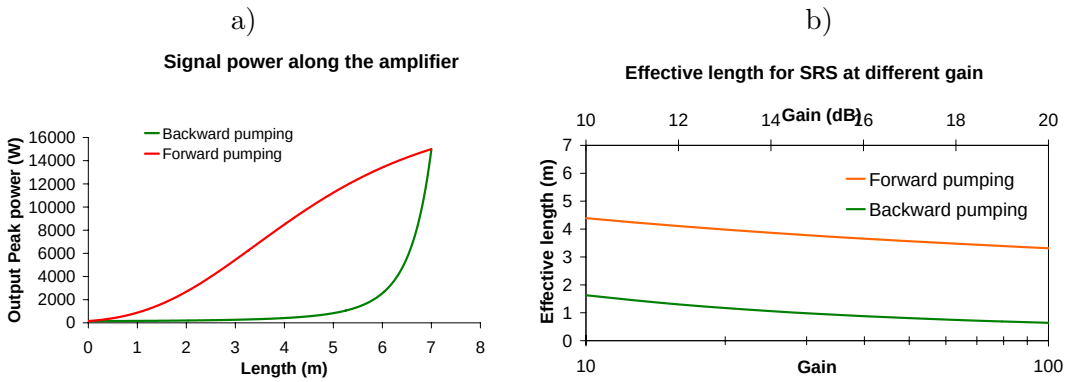

Figure 2.7: a)The growth of signal power and b)SRS effective length in a fiber amplifier with forward and backward pumping schemes with pump absorption of 2dB/m, total signal energy gain of 20dB and input peak power of 150W.

Threshold

The use of Equations 2.40 or 2.42 requires an input intensity $I_s(0)$ at $z = 0$. In a real system, SRS builds up from spontaneous Raman scattering which occurs throughout the fiber length. Smith (1972) has shown that this process is equivalent to injecting a fictitious photon per mode at the input end of the fiber. Then, the Stokes power is calculated by considering amplification of each frequency component of energy $\hbar\omega$ according to Equations 2.40 or 2.42 and then integrating over the whole range of the Raman-gain spectrum. The total Raman power at the output end of the fiber is given by

$$P_s(L) = \int_{-\infty}^{\infty} \hbar\omega e^{[g_R(\omega_p-\omega)I_p(L)L_{eff}(L)+\alpha_s L]} d\omega. \tag{2.44}$$

The Raman threshold power P_0^{cr} is defined as the pump power at the amplifier output which generates the same amount of Stokes power at the amplifier output, $P_s(L) = P_p(L)$. The Raman gain is strongly peaked at frequency shift of 13.4THz from the pump, and by assuming that the Raman gain profile can be approximated by a strongly peaked Lorentzian gain profile, Smith (1972) has calculated P_0^{cr} to be given approximately by

$$P_0^{cr} = 16\frac{A_{eff}}{g_R L_{eff}} \tag{2.45}$$

where A_{eff} is the effective mode area of the SRS pump.

A similar analysis can be carried out for the backward SRS. The threshold condition in that case is still given by Equation 2.45 but the numerical factor of 16 is replaced with 20. As the threshold for forward SRS is reached first at a given pump power, backward

SRS is generally not observed in a fiber laser amplifier. Also, the above derivation assumes that the polarisation of the pump and Stokes wave is maintained throughout the fiber. If the polarisation is completely scrambled, the SRS threshold increases by a factor of 2.

Equation 2.45 is very useful in determining the Raman threshold power in the amplifier. This theory cannot explain the growth of the Stokes wave beyond the Raman threshold as it neglects pump depletion. However, it has been shown that the threshold condition remains relatively accurate [Agrawal (2001)]. When the Raman threshold is reached, the power is transferred from the pump to the Stokes wave very rapidly. The theory predicts a complete transfer from the pump to the Stokes wave. In practice, the lower Raman Stokes pulses can serve as a pump to generate a higher-order Stokes pulses if its power is large enough to satisfy the condition 2.45. This process of cascade SRS can generate multiple Stokes wavelengths. The number of high order Stokes components depends on the input pump power. Thus, the SRS threshold determines the maximum pump power level that can travel in the fiber without significant loss of its power to Raman Stokes.

Equation 2.45 also suggests two ways of increasing the pump power without generating SRS. The first is to increase the effective mode area A_{eff}. This leads to the use of large mode area fiber. The second is to use a shorter amplifier. This condition is achieved by using a higher dopant concentration in the fiber. Both of these two methods have some limitations. Generally, single mode operation of fiber is preferred in most applications due to high brightness. When the diameter of the core is increased, the numerical aperture must be kept very small in order to maintain the single mode condition. However, a very low numerical aperture can result in significant fiber loss due to radiation of the mode caused by bending or other perturbations within the fiber. Single mode operation is further compromised when a high level of Yb^{3+} is needed in the fiber because it increases the refractive index of the core, hence the numerical aperture. Very high Yb^{3+} concentrations also can lead to concentration quenching in the fiber resulting in a loss in amplifier efficiency.

2.9 Conclusion

The basic theoretical treatment in this chapter is the basis for the experimental investigations which will be detailed in the following chapters. The dynamics of the pulse travelling through the MOPA is first characterised. Then the SRS at the output of the high peak power pulse is measured. Using this knowledge of the MOPA performance, active pulse

shaping of the output is performed.

Chapter 3

Large Mode Area Fiber Characterisation

3.1 Introduction

This project was funded by Southampton Photonics Inc. (SPI). One essential aspect of the project was to use the GTWave pumping scheme. Traditionally, SPI GTWave technology involves conventional fibers of 125μm outer diameter (OD). This technology is able to produce the fiber core with a diameter of up to about 25μm before signal light traveling in the core being disturbed by the outer structure of the fiber.

The aim of the project was to develop an all fiber MOPA system that is capable of operating with more than 1mJ output pulses, an average power of more than 100W, a pulse duration of few tens of nanoseconds and a repetition rate of few tens of kHz. With these requirements, fiber core size of up to 40μm might have to be used. Therefore, this required new fabrication process of the GTWave fiber to incorporate a much bigger OD, of order more than 300μm, in the GTWave bundle. Understanding the characteristics of large mode area (LMA) fibers in terms of their mode quality, bend loss will help better design and fabrication development of GTWave fibers.

Some existing LMA fibers were characterised to provide guidance for the development of the new larger core fibers. The experimental measurements were performed with the aid of a simulation code developed by the research and development team at SPI. The measurement results can be compared to the calculated results. Most important properties of LMA fibers including number of supported modes, propagation constants, bend loss, beam propagation factor (M^2) and mode field diameter were characterised.

3.2 Fibers Description

A series of LMA fibers were available for the characterisation work. The fibers were drawn previously from the preforms with the index profiles as shown in Figure 3.1. The preforms were made using the modified chemical vapour deposition (MCVD) and solution doping technique. Figure 3.1 a) shows the profile of preform called LF128 which was doped with a Yb^{3+} concentration of 8000ppm (weight). The fibers from this preform have a D-shape cladding and a core to cladding dimension of 1/10. There are three fibers with core diameter of 20, 30 and 40μm. The 40μm fiber has been used in a Q-switch fiber laser previously [Piper et al. (2004)]. The index profile of preform HD669 is shown in Figure 3.1 b), the dopant concentration is 3000ppm (weight). A fiber from this preform had a core diameter of 20μm with rectangular cladding of 120×150μm with NA=0.4. The next set of fibers with core diameters of 20, 30, 40μm with core to cladding ratio of 1/10 were drawn from preform LF214 (Figure 3.1 c)). Finally, fibers from preform L20398 from SPI with a profile as shown in Figure 3.1 d) were investigated. These fibers are produced in three formats with a core and cladding sizes of 20μm/125μm, 20μm/300μm and 20μm/125μm in a GTWave format.

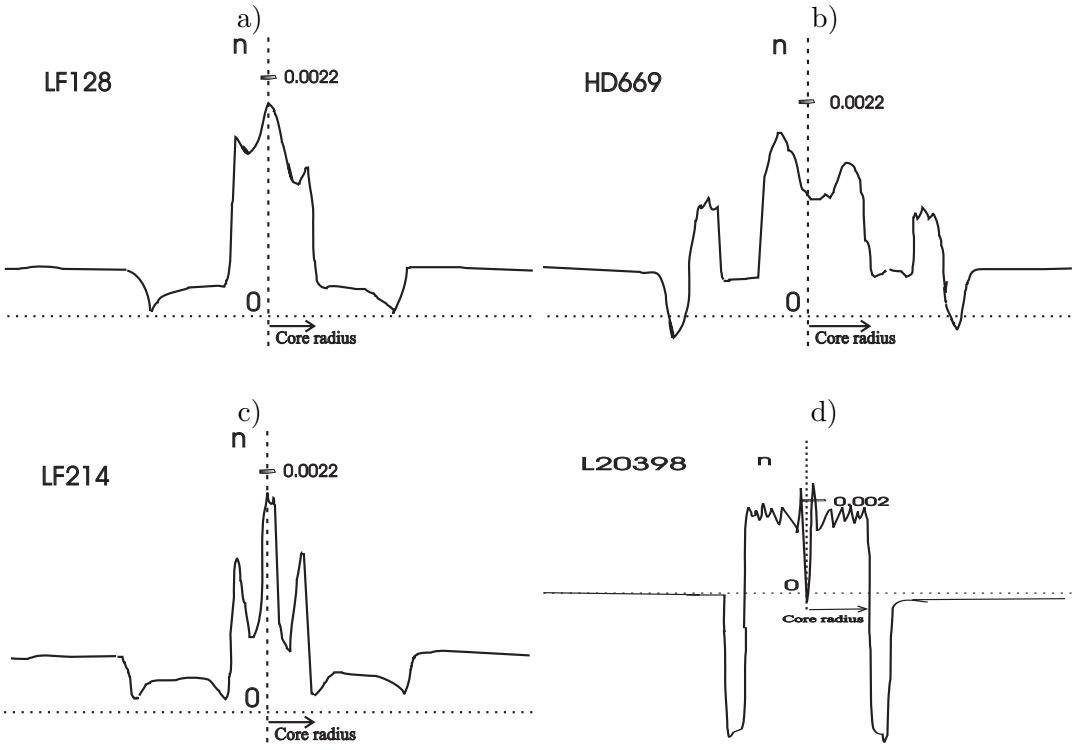

Figure 3.1: Profiles of the fibers used in characterisation.

3.3 Mode Observations

The simulation of the modes was done using a code written by Dr Fabio Ghiringhelli (SPI) based on a model by Sakai and Kimura (1978). The simulation calculations give the number of modes that a fiber can support, together with the effective refractive index and bend loss for each mode. The results are shown in Figure 3.2 and 3.3. From the bend loss results it is clearly shown that single mode operation of these fibers should be possible by bending the fiber at an appropriate bend radius. There is a cut off point for each mode where the bend loss rises rapidly. For single mode operation, the fiber should be bent so that the higher order modes have very high bend loss while the single mode remains nearly lossless. In order to verify the plausibility of this method a simple experiment was set up to observe the modal output at different bend radii.

The experimental setup is as shown in Figure 3.5. The apparatus incorporated a pigtailed cw Nd:YAG laser operating at 1064nm. The beam was coupled to the fiber with a length of about 1.5m using a pair of microscopic lenses with focal lengths of 15mm. The fiber was placed on a raised stage and could be coiled in a circle defined by a series of pins pushed into the platform. The bend radius could be varied by moving the pins to the circles pre-drawn on the platform. The two ends of the fiber were stripped and painted with adhesive graphite to remove the cladding modes. The output end of the fiber was secured on a micro-stage, which was held on a translational rail. The output end of the fiber was collimated using a $\times 20$ microscopic lens. A CCD camera (Cohu7512) was used to collect the images of the output and displayed them on a computer monitor.

The images showing the core structures and the output mode transformation as the fibers were bent are in Figure 3.2 and 3.3. It was very clear that for LF128 20, 30, and 40μm fibers single mode operation was obtained at radii in good agreement with the simulation results. Single mode output was obtained with the bend radii of 9cm, 5cm and 3cm, respectively. Further bending below these critical radii produced a single mode but with much lower power output due to induced bend loss for the fundamental mode. These single modes were stable against launch and fiber perturbation.

However, other fibers, HD669 μm, LF214 20, 30 and 40μm with much more complicated index profile, produced distorted output. The output profile tended to follow the index profile structure. In the HD669 20μm, there is a large ring outside the core. This ring was designed to increase the bend loss differential between the fundamental and the second order mode. The experimental image (Figure 3.3) shown clearly that a ring mode formed

a) LF128 20μm

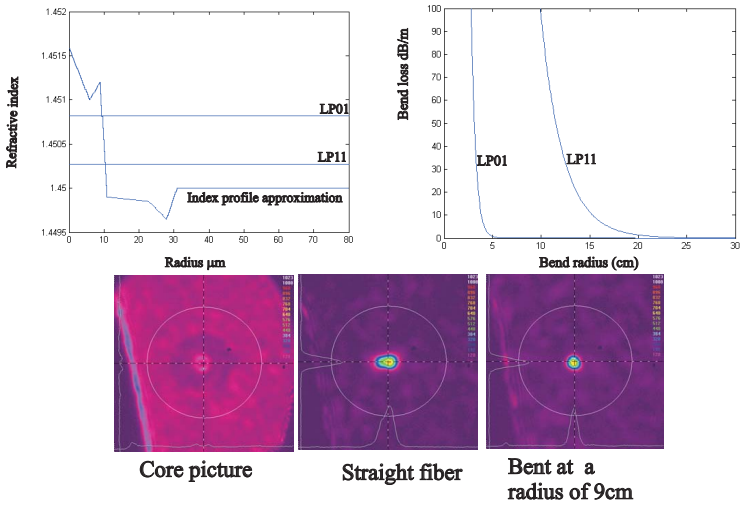

b) LF128 30μm

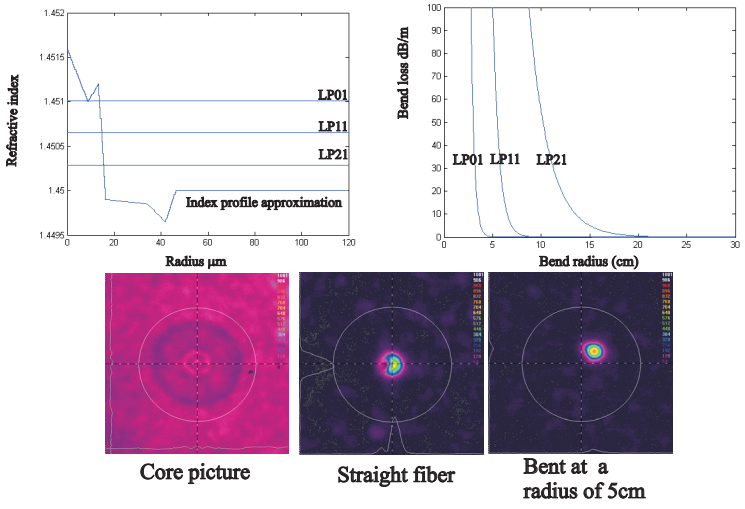

c) LF128 40μm

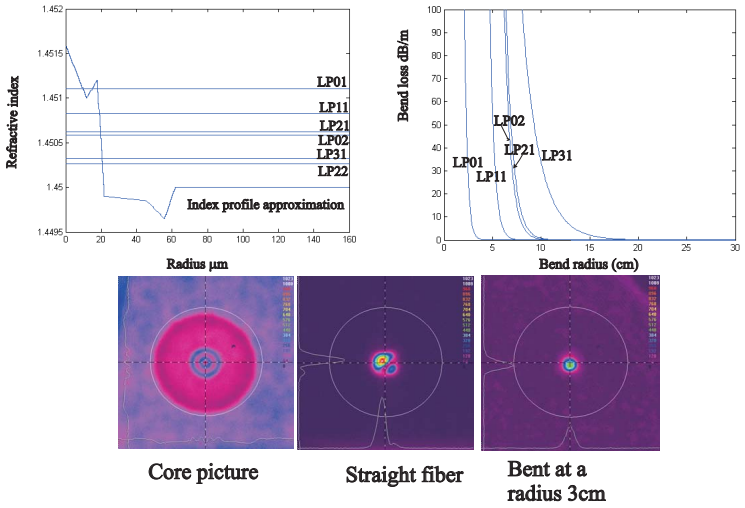

Figure 3.2: Effective refractive indices of the modes and their bend loss and output mode images of LF128 fibers.

a) HD669 20μm

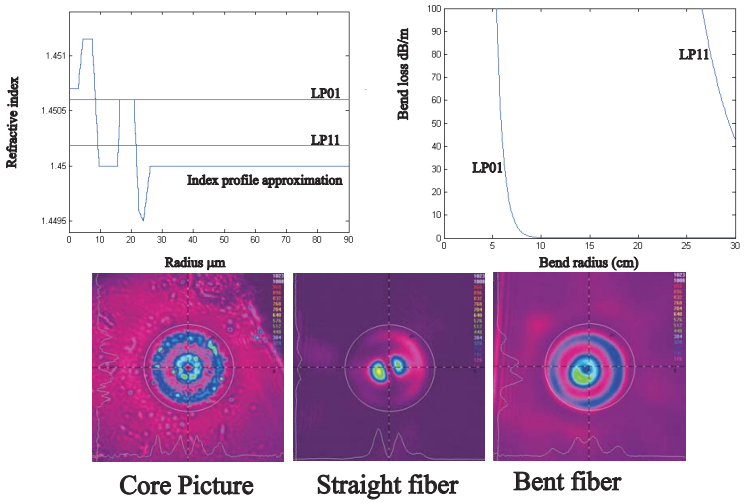

b) LF214 40μm

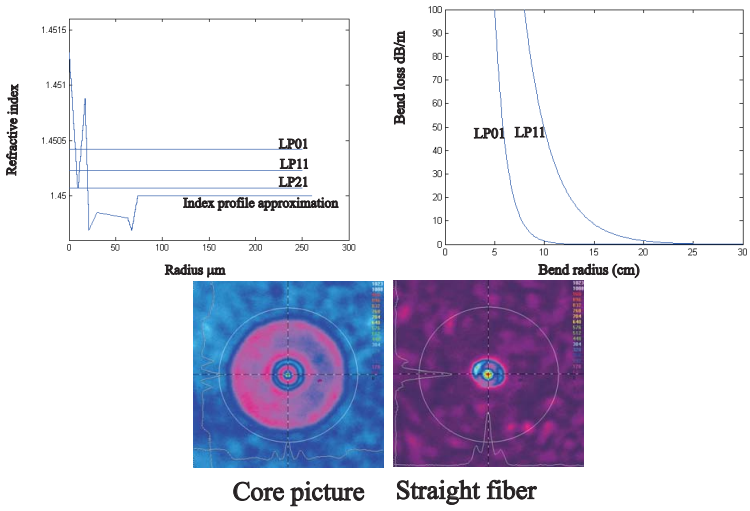

Figure 3.3: Effective refractive indices of the modes, their bend loss and output mode images DH669 and LF214 fibers.

and propagated in this raised index ring. The effect increased when the fiber was bent with relatively large bend radius (∼20cm). Light was only very weakly guided in the 20 and 30μm LF214 fibers. The 40μm LF214 fiber supports one mode, however it follows the index profile such that there is a peak in the middle and a ring; the mode distorted further on large bend radius. Fibers from preform L20398 were also investigated. This fiber supported two modes with a bend loss as in Figure 3.4. The typical output beam has the profiles as shown on the same figure. It emerged that it was not possible to obtain single mode operation even with very small bend radii (below 2cm) for these fibers.

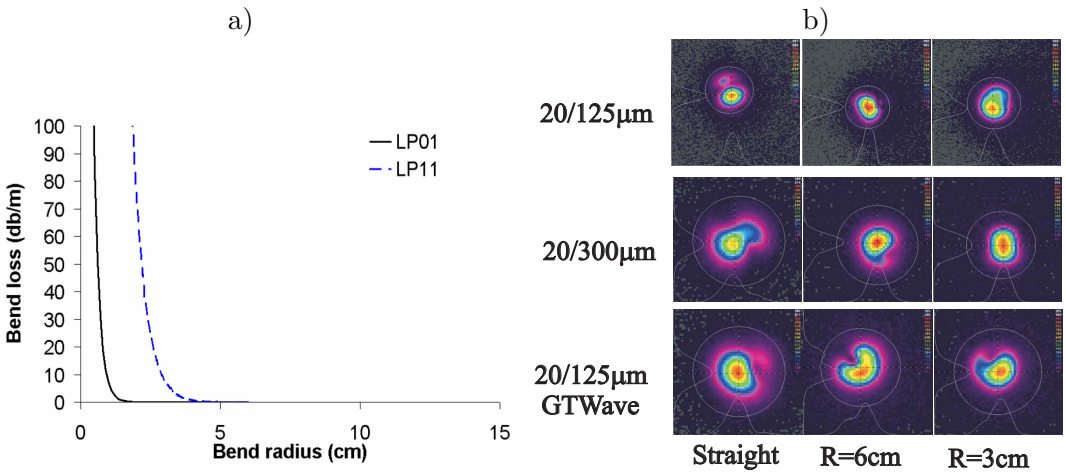

Figure 3.4: Calculated bend loss a) and observation of output modes b) of three fibers made from preform L20398.

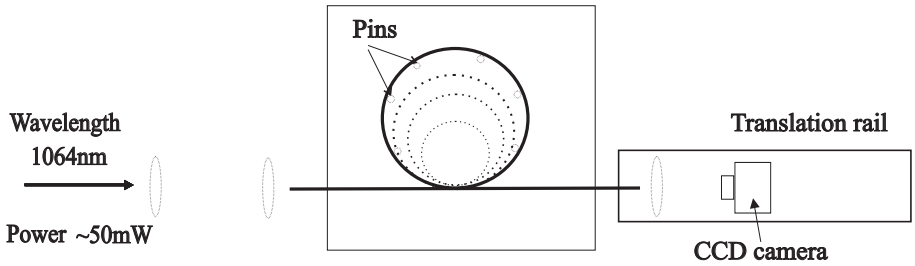

Figure 3.5: Schematic of the experimental setup to observe output modes, and measure bend loss.

3.4 Bend Loss

From the mode quality investigation above, it was decided that the best LMA fibers for use in further measurement of bend loss and M^2 were LF128 20, 30 and 40μm and L20398 20μm. These fibers supported modes that are confined relatively strongly within the core. The rest had a very bad output beam structure that are thus not useful in applications.

The bend loss measurement setup was very similar to the one in Figure 3.5. A detector was placed at the camera position. Both ends of a section of fiber approximately 1.5m in length were stripped and painted with black adhesive graphite. The fiber was first laid straight, the launch power was optimised to give maximum output power. Then the fiber was coiled into one loop of radius R on the platform. The height of the platform was kept the same as the launch and detection optics to ensure that the fiber lays flat along its entire length. A series of measurements of transmitted power were recorded for different bend radii. During the measurement, the launch conditions were carefully monitored to ensure that there was no significant drifting away from the optimum launching condition.

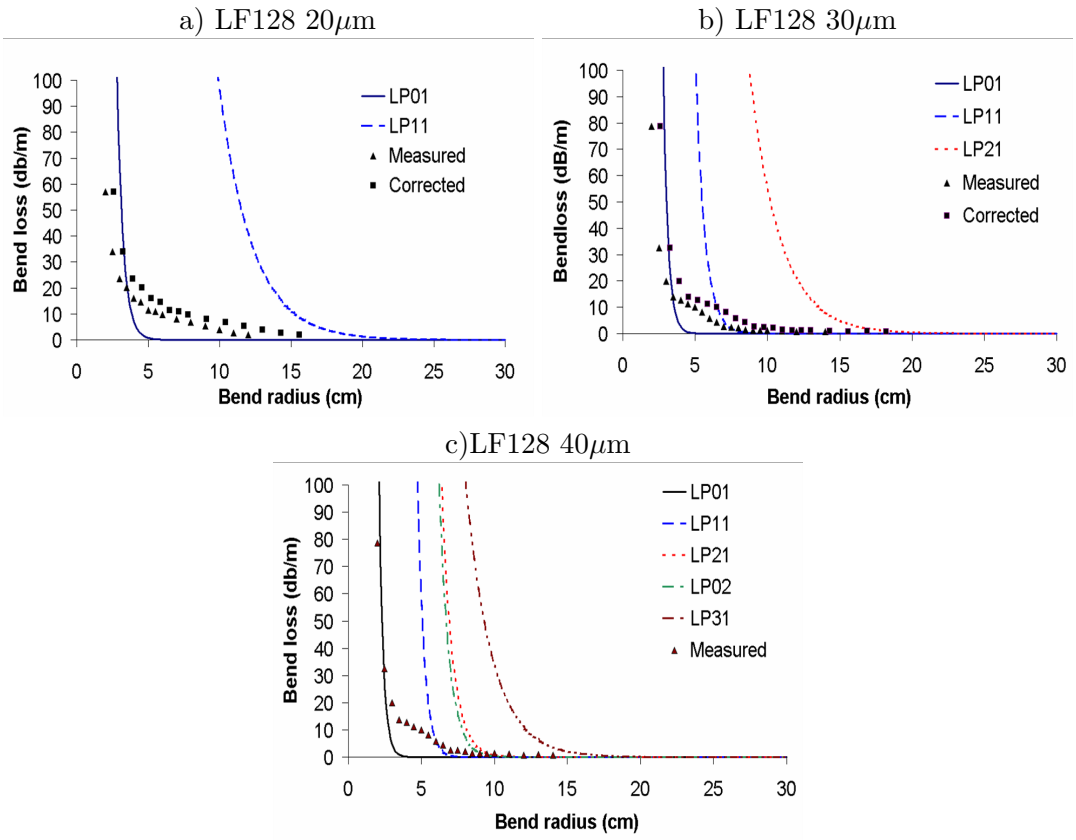

Figure 3.6: Bend loss results of the LF128 fibers with core diameter of a) 20μm b) 30μm and c) 40μm; the solid lines are the simulation results and the discrete data is measurement results.

Figure 3.6 a) b) and c) show the results for LF128 20, 30 and 40μm diameter fibers. The results were in very good agreement with the simulation results. It is clearly shown that single mode operation was obtained when the fibers were bent below the critical radii. There were steps in the measured data, these indicated that there were more than one mode propagating in these fibers when straight. These steps were at the position of the cut off radii of the second mode. There was no indication of higher order modes other than the LP11 mode in these fibers. For the 40μm fiber, the measured data fitted the simulation best, the critical radius of the fundamental mode was at about 2.5cm.

However, in the 20 and 30μm fibers the experimental data was slightly off the simulation results, the measured critical data was lower than expected from the simulation results. These observations can be explained by the fact that there is a stress induced refractive index change due to bending [Nagano et al. (1978)]. This effect increases the refractive index contrast between the core and the cladding leading to lower bend loss than predicted. This effect is much more profound in lower index difference or smaller core or more single-mode fiber than in more multi-moded fiber. This explains why there

was a greater difference between the measurement data and the simulation results in 20 and 30μm fibers than in 40μm fiber. This effect could be accounted for by elastooptical correction [Sharma et al. (1984), Renner (1992)]; the ratio of the theoretical radius over the experimental one is in the range from 1.27-1.31. So by using the transformation $R/R_{exp} = 1.3$, the second curves were plotted on the 20 and 30μm fibers. Those curves are now more consistent with the predicted values.

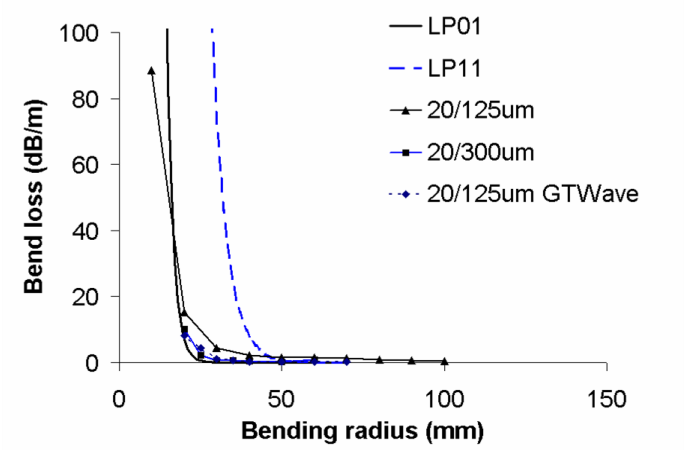

Figure 3.7: Bend loss measurement result for fiber L20398 with 20μm core in three cladding format: 125μm, 300μm and 125μm GTWave.

The bend loss of fiber L20398 20μm was also measured, the result is presented in Figure 3.7, which shows all three formats with the same 20μm diameter core but different cladding diameters: 125μm, 300μm, and 125μm in GTWave format. The graphs indicate that, there was only one mode in the fiber. However, from the modal observation, there was clearly more than one mode in the output beam at any bend radii. The 125μm cladding could be bent at much smaller radii because of its flexibility. The two others appear to have slightly lower bend loss. These fibers were designed with a very deep dip ring at the edge of the core, this ring might help the mode coupling process upon the application of external stress. It could also trap the energy that radiated from the core due to bend loss giving rise to results that are hard to interpret further.

3.5 Beam Propagation Factor M^2

The beam propagation factor or beam quality factor, M^2, is a common measure for the quality of a laser beam. It is a number to indicate how close to diffraction-limited a laser beam is. A diffraction-limited beam has an M^2 of 1. Any other beam has an M^2 of greater than 1. To measure M^2 of a beam, a single lens is used to form a beam waist then a CCD

camera is then used to characterise the size of the beam in a few Rayleigh ranges on both side of the beam waist.

The experimental set up is as shown in Figure 3.8. Light was launched into one end of the fiber and other end was firmly secured at one end of a long translation rail. The fiber was positioned so that the diverging beam from the end was aligned parallel to the translation rail. Two lenses were then used to create a beam waist. The COHU 7512 silicon CCD camera was mounted on the rail and scanned through the beam waist. It was important to choose a lens combination such that the beam waist was not too small for the resolution of the camera (6×6μm) nor not too big for for the size of the CCD chip (3×3mm).

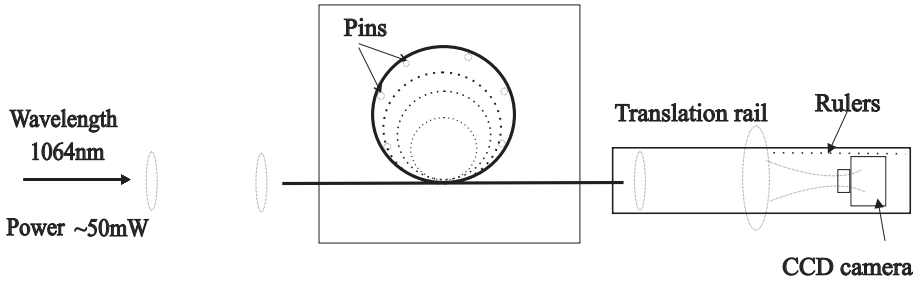

Figure 3.8: Schematic of the experimental setup to measure M^2.

There are two methods to measure the width of the beam. The first one is to approximately fit the Gaussian profile obtained on the camera. The width is determined by the size of the profile at which the power drops by $1/e^2$. This method is only accurate when the beam is very close to a Gaussian function. The second method is to use the ISO 11146 standard called 4-Sigmal. According to this method the beam width is defined via a second-order moment of the power-density distribution (σ). For x and y directions σ is given by

$$\sigma_x = \frac{\int_\infty^\infty (x-x_0)^2 I(x,y)dxdy}{\int_\infty^\infty I(x,y)dxdy}, \quad \sigma_y = \frac{\int_\infty^\infty (y-y_0)^2 I(x,y)dxdy}{\int_\infty^\infty I(x,y)dxdy} \tag{3.1}$$

This method allows accurate measurement of a beam of any profile whether it is near Gaussian or non-Gaussian. However, the disadvantages of this method is that it requires a very clean beam, meaning that there is no background light present since this can give rise to a large error. In the case of a low index coating LMA fiber, it is difficult to remove the cladding mode totally despite the use of clad light stripping agents, therefore, some background light might lead to inaccurate value of the width.

The M^2 value can be calculated once the beam width is known by fitting the following

equation to the data obtained:

$$W_x^2(z) = W_{0x}^2 + M_x^4(\frac{\lambda}{\pi W_{0x}})^2(z - z_0)^2$$
$$W_y^2(z) = W_{0y}^2 + M_y^4(\frac{\lambda}{\pi W_{0y}})^2(z - z_0)^2 \quad (3.2)$$

where W_{0x} and W_{0y} are the beam width in the x and y directions at the beam waist ($z = z_0$).

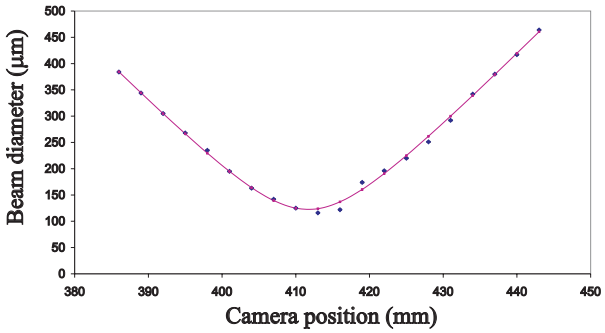

Figure 3.9: Typical curve obtained from the M^2 measurement, the solid line is the fit and the dots are the measurement data, the fitting gives M^2 of 1.2 (LF128 40μm bent at radius of 25mm).

Beam propagation factors for the fibers made from preform LF128 and fibers from L20398 were measured at different bend radii to determine the single mode operation in conjunction with the bend loss data. A typical result for the M^2 measurement curves is shown in Figure 3.9. Table 3.1 summarises the measured value of M^2 at the bend radius that produced a single mode for each fiber and the simulation results for the fundamental modes for each fiber. The value of M^2 shows that the output is quasi-single mode. A portion of cladding mode might still be in the background during the measurement and thus slightly increase the value of M^2.

Furthermore, these fibers are active fibers. When they are used in laser set ups there will be gain differentials between different modes, which might lead to the fundamental mode being preferentially amplified, hence lowering the values of M^2 to even closer to the predicted values. The values of M^2 obtained for this preform are consistent with the mode observation and bend loss measurement results.

On the other hand the results for preform L20398 varied greatly from the expected values, the numbers also varied from measurement to measurement, as seen in Table 3.1. The mode observation in Figure 3.4 indicated that it was impossible to obtain single mode operation for this preform. At this stage no other explanation has been put forward to

establish this discrepancy other than the possibility of an unusual trapping effect caused by the dip ring outside the core.

Preform	**Fiber core/cladding** (μm)	**Bend radius** (mm)	**Measured** M^2	**Predicted** M^2
LF128	20/200	70	1.25±0.05	1.00
	30/300	40	1.10±0.05	1.01
	40/400	25	1.20±0.05	1.02
L20398	20/125	30	1.3-1.5	1.03
	20/300	30	1.3-1.6	1.03
	20/125 GTWave	30	1.5-1.8	1.03

Table 3.1: M^2 values of LF128 and L20398 fibers at bend radii for single mode outputs.

3.6 Mode Field Diameter

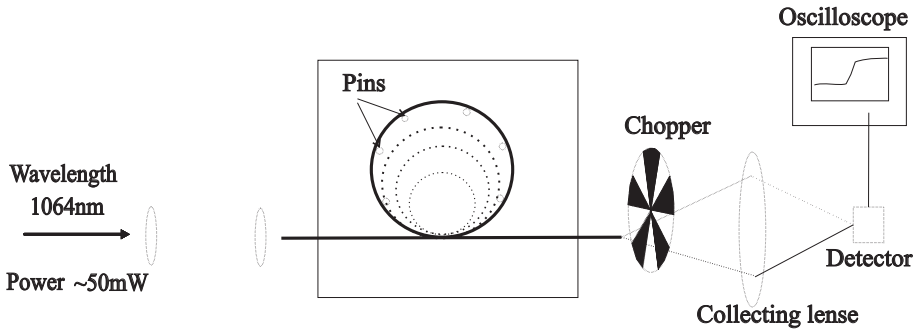

Figure 3.10: Schematic of the experimental setup to measure mode field diameter.

The mode field diameter was measured using a scanning knife-edge technique [Otten et al. (1986), Artiglia et al. (1989)]. The setup is shown in Figure 3.10. The output beam from the fiber core is modulated by an optical chopper and then focused into a photo diode detector by a large collecting lens. The output beam radius ω at a distance z from the end of the fiber can be calculated from a knowledge of the distance from the beam to the centre of the chopper r, the frequency f of the signal on the oscilloscope from the detector, the number of holes in the chopper N and the rise time τ from the displayed shape in the oscilloscope from the equation:

$$\omega = 2\pi \frac{f}{N} r\tau \tag{3.3}$$

The linear plot of ω against distance z gives the slope of θ_0 as:

$$\theta_0 = \frac{\Delta\omega(z)}{\Delta z} = \frac{\lambda}{\pi\omega_0}. \tag{3.4}$$

Hence the mode field diameter and mode field area are:

$$MFD = 2\omega_0, \qquad A_{eff} = \frac{\pi}{4} MFD^2 \tag{3.5}$$

Mode field diameters of LF128 20, 30 and 40μm were measured using the setup as shown in Figure 3.10. A typical set of obtained data is as shown in Figure 3.11 and the summary of the results is shown in Table 3.2. On this table the measured MFD column is the value calculated directly from the slope of the graph of diameter against distance of the chopper to the end of the fiber without taking into account the value of M^2. However, the adjusted MFD column is the value that is calculated by dividing the measured value of MFD over the measured value of M^2. The last column of the table shows the simulated result or the MFD of the fundamental modes of these fibers. The MFD values of fundamental modes of the 30μm and 40μm core diameter fibers are very similar despite the large increase in the core size. Therefore, there is a practical limit on the MFD of fundamental mode in these LMA fibers. From these numbers, one can confidently confirm that the simulation gives good results for these particular fibers.

The mode field diameters of the fibers from preform L20398 were not investigated because of the distorted output beam. The techniques which were used in this measurement are only accurate for a near-Gaussian beam.

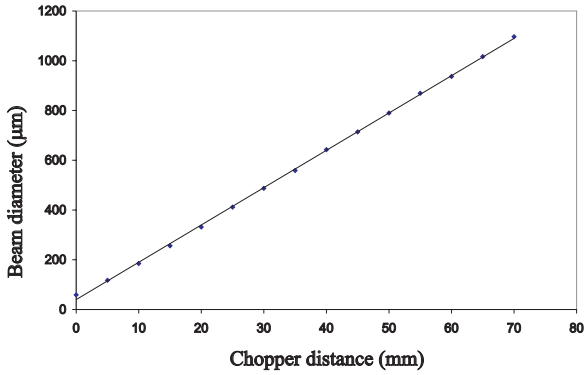

Figure 3.11: Typical output of a mode field diameter measurement (here, LF128 30μm bent at 40mm radius).

Fibers LF128	**Bend radius** (mm)	**Measured** (μm)	**Adjusted** (μm)	**Calculated** (μm)
20/200 μm	70	20± 1	16± 1	17
30/300 μm	40	22± 1	20± 1	21
40/400 μm	25	30± 1	25± 1	22

Table 3.2: MFD of fundamental mode of LF128 fibers.

3.7 Conclusion

The properties of various LMA fibers have been investigated in detail. Measurements made include output mode observation, bend loss, M^2 and mode field diameter. It has been found that the simulation results are in good agreement with the experimental results. The preform LF128 gives single mode operation for all fibers of 20, 30, and 40μm core diameters by bending them to an appropriate radius. The output is quasi-single mode with an M^2 close to 1. The flat top index profile is found to be the preferred choice relative to a more complicated profile since the mode profile tends to follow the refractive index profile for large core sizes.

Based on the above results progress has been made towards the fabrication of the LMA fibers for the 1mJ project. A preform with a near flat top index has been produced. The GTWave drawing process has also been modified in order to produce large OD fibers with large diameter cores.

Chapter 4

Nanosecond Pulsed Fiber MOPA

4.1 Introduction

In this chapter I describe work I performed to qualify the performance of a 0.5mJ MOPA system, close to that commercialised by SPI laser. The characterisation was done under a variety of different operating conditions. Various operating limitations of this system were also considered.

A number of experiments was conducted on an 0.5mJ MOPA system. This MOPA comprises a direct-modulation seed semiconductor diode, a single mode GTWave preamplifier stage and a large mode GTWave postamplifier stage. The performance of this system was systematically studied at various pulse durations and repetition rates. The backward pump scheme was used to produce the most stable output with the least nonlinear distortion, specially the effect due to SRS. SRS was found to be the fundamental limit to the peak power of the output. The generation of SRS Stokes occurred in the passive delivery fiber at the end of the postamplifier and in the forward direction.

4.2 Setup

The MOPA consisted of a direct modulated diode, a preamplifier and a postamplifier. Figure 4.1 shows the detailed configuration of the MOPA. This amplifier was built as a demonstration of 0.5mJ system. The final stage amplifier used existing fibers similar to L20398 due to commercial needs. The fabrication of the fiber was done before the results of the fiber characterisation work as described in the Chapter 3.

An electrical pulse of a duration of a few tens of nanoseconds drove a semiconductor diode operating the wavelength range from 1064nm to 1080nm (tuned by temperature). The power to the diode is supplied by an electrical board which has a rise time of about 20ns. The signals that drove the pulses were programmed on a Sony Tektronix Arbitrary Waveform Generator (AWG2021) which had a time step resolution of 4ns. Therefore, the

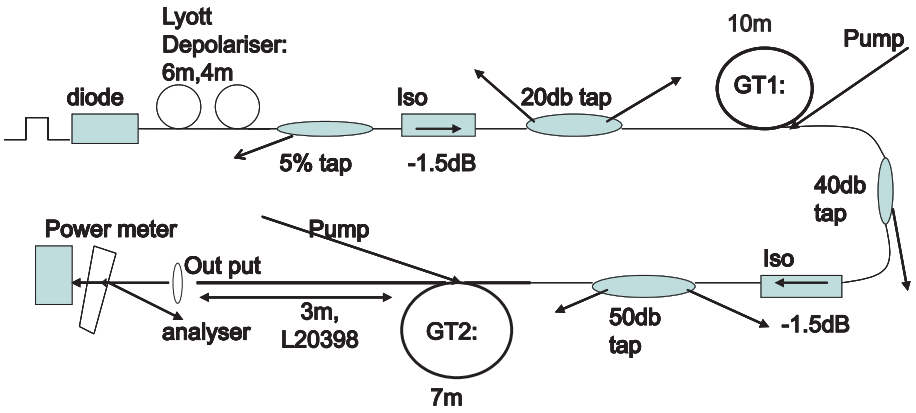

Figure 4.1: Detail setup of the 0.5mJ MOPA consists of a seeding diode, a preamplifier (GT1), a postamplifier (GTWave 2), isolators to prevent backward amplification and taps to monitor the pulses.

diode was capable of producing pulse durations from 10ns to a few hundreds of nanoseconds at repetition rates in the range from a few hundred hertz to a few hundreds of kHz.

The output of this diode was fed into the preamplifier which was made from a single mode GTWave 1 fiber of 6μm core, 125μm cladding and 10m length. The output of the preamplifier was then amplified further as it travelled in the GTWave 2 amplifier. This GTWave device had an LMA signal fiber with a core of 20μm in diameter, cladding of 125μm and length of 7m. The GTWave 2 had a core made from a doped preform which has a refractive profile similar to the one of preform L20398 (see page 26). The fiber can support two modes which have critical bend radii at about 2cm and 4cm for LP01 and LP11, respectively. The core was strategically ring doped with an inner radius of 5μm and an outer radius of 10μm. The aim was to flatten the fundamental mode in order to reduce the peak power, and hence, to reduce nonlinear effects. There was a length of passive delivery fiber made from preform L20398 spliced to the end of the postamplifier. The passive fiber had a core diameter of 20μm. Initially, this fiber had a length of 3m.

Both GTWave amplifiers were backward-pumped to reduce the effect of nonlinearity. With this pump configuration, the signal gained power most rapidly at the end of each amplifier, therefore the high peak power travelled the least distance and the effect of nonlinearity is significantly reduced. The GTWave 1 was pumped with power of up to 5W by a pigtailed diode pump at 915nm. The postamplifier was pumped by a 915nm pigtailed diode with power of up to 30W.

There were also various taps to monitor the power, pulse shape and spectrum of the laser beam distributed through the system. The isolators were used to prevent backward

amplification that could otherwise reduce the efficiency of the MOPA and potentially damage the seed diode. This MOPA had gain within the two GTWave amplifiers, and loss on the splices, taps and isolators. The losses on the taps and splices were relatively low compared with those on the two isolators whose loss was 1.5dB each.

4.3 Experiment Method

This system was characterised by monitoring the pulses in term of their power, pulse shape, and spectral content as they propagated from the diode to the output of GTWave 2. The energy gain on each stage at each pump condition was calculated from average power data measured through the taps. The final output was analysed further to determine the relative content of ASE and SRS in the output beam.

The output beam contained the amplified optical pulse and a background ASE. The ASE content was measured using a time resolved measurement. In this technique, the extracted output beam was sent though an Acousto-Optic Modulator (AOM) as shown in Figure 4.2. This AOM was driven by a Stanford Research System pulse generator and was triggered by the signal from the seeding pulses. The AOM could be controlled to gate only the pulses or only the ASE, which is a continuous signal, to the OSA and oscilloscope. The AOM responded effectively only to electrical drive pulses of more than 400ns duration. A shorter pulse did not deflect the optical pulse effectively enough due to the slow response time of the AOM. An appropriately synchronised electrical signal pulse was turned on to control the rf signal supply to deflect the optical pulse, the ASE signal or both. A square electrical pulse with background voltage of 0V and the peak voltage of 4V was applied to deflect the optical pulse. An inverted square pulse with background of 4V and a dip at 0V was used to deflect the ASE. A constant DC signal could be used to deflect both the signal and the ASE components of the output beam.

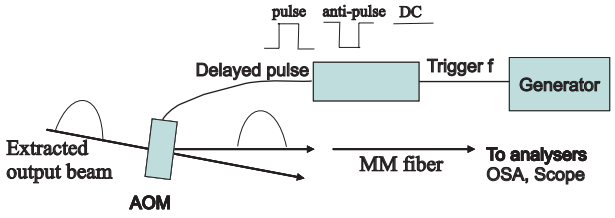

Figure 4.2: Set up to measure ASE by using an AOM to separate the pulse and ASE content.

4.4 Long Pulse Amplification

The amplification of relatively long pulses of 100ns duration was first investigated. The diode was modulated with square electrical drive pulses of 100ns at repetition rate of 20kHz. The average output power of the diode was 657μW. The output pulse shape is shown in Figure 4.3 a). The output signal was a relatively square pulse with a rise time of about 30ns. After 30ns, the pulse was flat for nearly the whole duration. The relaxation time at the tail of the pulse was about 15ns.

Figure 4.3 b) shows the spectrum of the diode output. The signal peak wavelength was at 1076nm with a bandwidth of 3nm (FWHM).

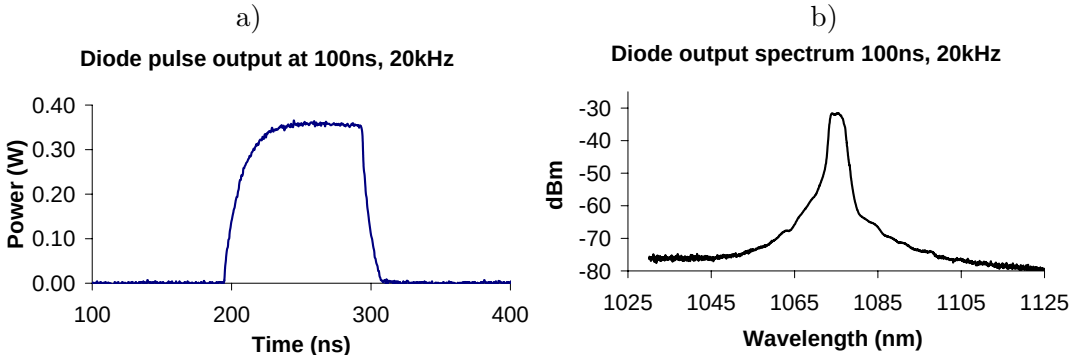

Figure 4.3: Output pulse shape a) and spectrum b) from the diode at 100ns, 20kHz.

The pulse shape and spectrum of the output at 27dB gain (3.5W pump power) are shown in Figure 4.4. The pulse shape kept the original form and the spectrum was also very similar to the output of the diode. There was no sign of the Raman effect on the spectrum at this level of gain.

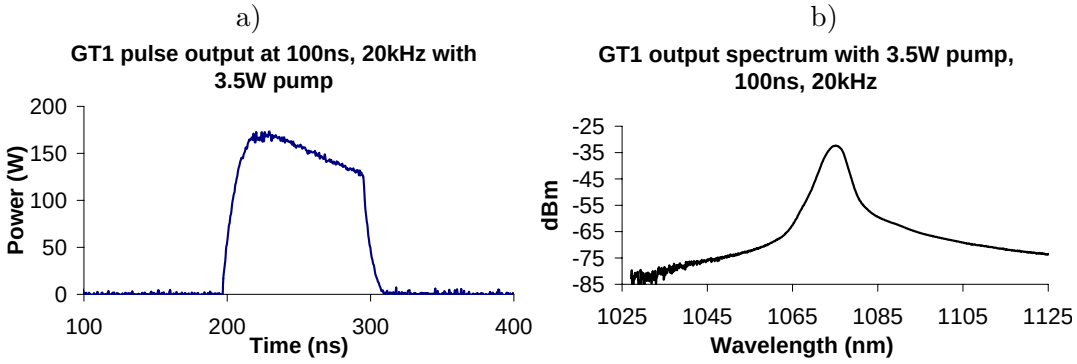

Figure 4.4: Output pulse and spectrum from the GT1 with 3.5W pump.

GTWave 1 was then pumped at various power levels up to 4W. The output power and the gain on this preamplifier are shown in Figure 4.5. A maximum signal gain of about

29dB was obtained. Higher gain could be obtained, however, a lower gain was preferred to avoid instability or the generation of backward pulses that could damage the seed diode.

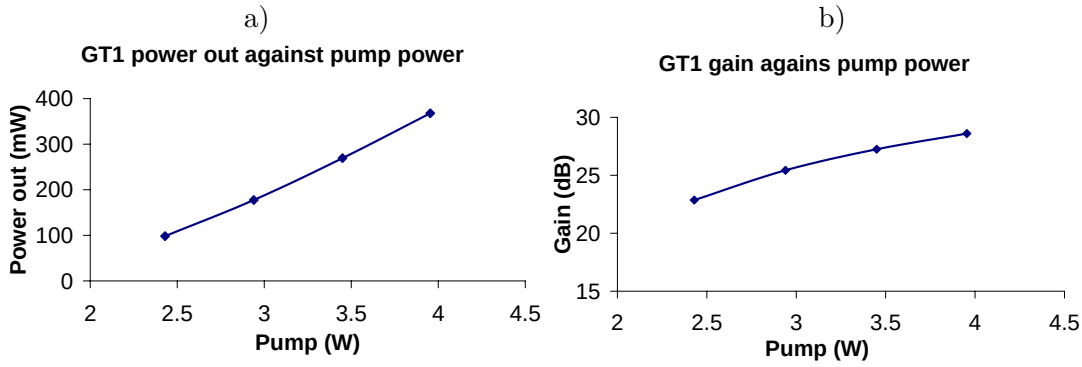

Figure 4.5: Power output and gain from the GT1 against pump power.

There is a slight gain saturation effect in the preamplifier, therefore, it is useful to apply the calculation in Section 2.5 on page 15. The value of saturation energy and initial gain can be extracted by least square fitting the Equation 2.25 to the experimental data obtained in Figures 4.3 a) and 4.4 a). The result of the calculations are shown in Figure 4.6. In the figure, there are 4 plots against time along the pulse: gain (in dB), scaled input pulse (the initial pulse from the diode multiplied by the overall energy gain of 27dB), the predicted output pulse, and the measured output pulse. The gain was decreased gradually from 28dB to 26dB across the pulse. There is some pulse distortion as it propagates through the high gain amplifier. The experimental result and the predicted curve show a high level of consistency. The saturation energy of the fiber was calculated to be 2.7×10^{-2}mJ, and the initial gain was 27.7dB.

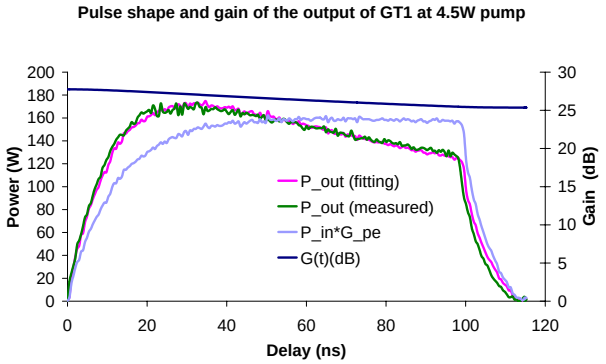

Figure 4.6: Saturation of gain in GTWave 1 during the pulse, the initial gain was at 28dB then dropped down to 26dB at the end of the pulse.

The pre-amplified pulses with spectrum and shape as shown in Figure 4.4 was then launched into the postamplifier GTWave 2. In the postamplifier, the pulse gains most of

its energy with the power growing from few hundreds milliwatts to a few watts. Due to the high input energy compared with the saturation energy in the GTWave 2, there was a high level of gain saturation in this fiber.

The output power and signal gain of the postamplifier stage plotted against the pump power are shown in Figure 4.7; the output spectrum and pulse shape at various pump levels are shown in Figure 4.8. The spectra clearly show that there was very a low level of SRS in the pulse (30dB lower than the peak). The pulse energy of 0.42mJ was generated with a peak power at 11.5kW. The pulse shape distorted significantly from a nearly square pulse to a pulse with an exponential tail and a very high peak at the front. The peak at the leading edge was the main driver of the SRS effect. The effective pulse width was reduced to about 25ns (FWHM) at 25.7W of pump.

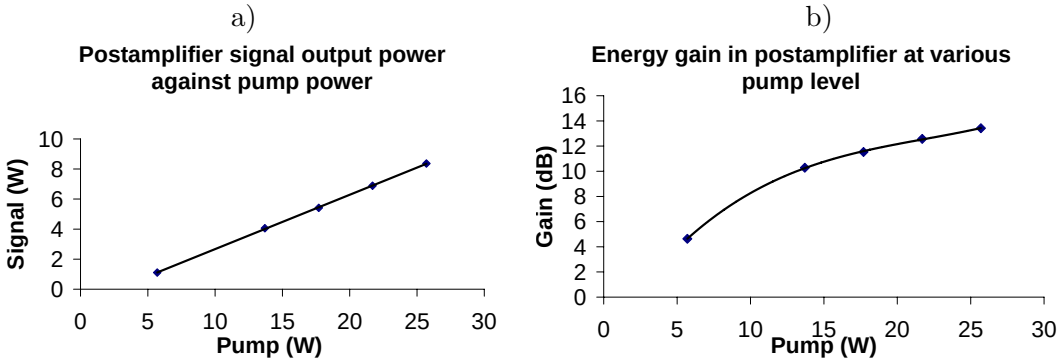

Figure 4.7: Power output and gain on GTWave 2 as a function of pump power.

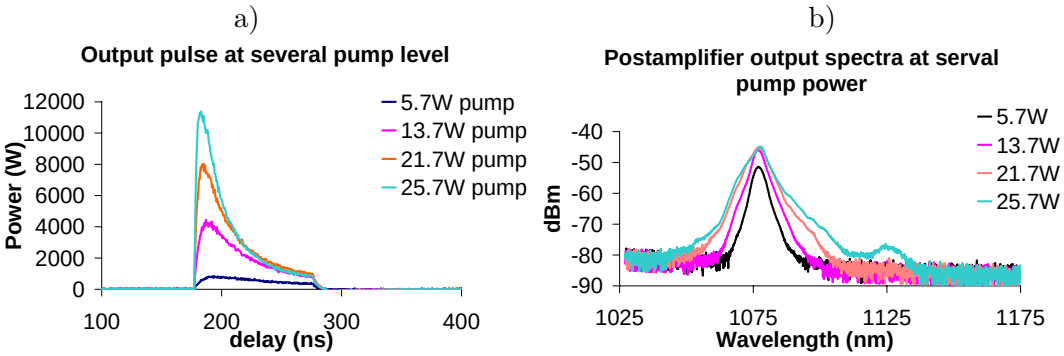

Figure 4.8: Output of postamplifier: Pulse shapes and spectra function of pump powers.

The same gain saturation analyses of the final output pulse was done as in the preamplifier case. The dynamics of the gain and pulse in the postamplifier along the pulse is shown in Figure 4.9. Unlike in the GTWave 1, there were significant pulse distortion in GTWave 2. The gain at the beginning of the pulse was as high as 24dB then dropped significantly down to just 9dB at the end of the pulse. The saturation energy was calculated

to be equal to 0.11mJ. This value was comparably smaller than the output pulse energy of 0.35mJ. A higher pulse energy could be obtained with a higher pump power as the maximum extractable energy has been suggested to be as high as 10 times the saturation energy [Renaud et al. (2001)]. Above this level, any additional pump power is simply lost as ASE between the pulse without significantly increasing the stored energy.

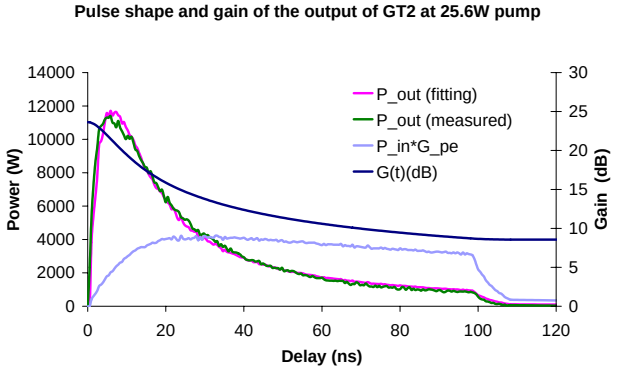

Figure 4.9: Saturation of gain in the GT2 during the pulse, the initial gain was at 24dB then drop down to 9dB at the end of the pulse. The saturation energy was 0.11mJ, the pulse energy was 0.35mJ.

In order to estimate the amount of ASE present in the spectrum, the time resolved measurement, as in Figure 4.2, was done using a 5V electrical signal of 400ns. The output spectra of the pulse only, ASE and whole beam at a pump power of 27W are shown in Figure 4.10. It is clear that the total of ASE power was about 20dB lower than the signal power. The signal pulse contained the main signal peak at 1077nm, the first order SRS peak at 1130nm.

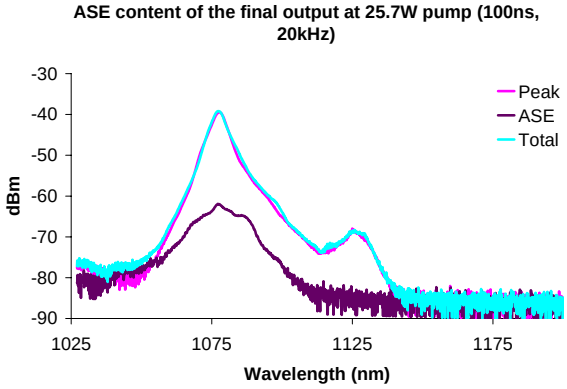

Figure 4.10: Time resolve measurement of the spectrum to measure ASE level, 25.7W GT2 pump, or 8.4W output signal.

The result for long pulse amplification shows that it is possible to generate pulses of 0.5mJ with very small amount of nonlinear effects and ASE. A peak power of 11kW was

achieved. The pulse energy could be much higher if the input was pre-shaped such that there is a ramped leading edge on the initial seed pulse. My measurements showed that the output power can be at peak of more than 11kW, hence, 1mJ pulses should ultimately be possible using the square pulse of 100ns.

4.5 Short Pulse Amplification

The next set of experiments were done with a pulse duration of 20ns and a repetition rate of 20kHz. The modulated signal was a square pulse of 20ns, 20kHz. Since the rise time of the diode was about 30ns the output of the diode has a ramped lead and a sharp tail as shown in Figure 4.11 a). The spectrum was the same as in the case of 100ns pulse duration. The pulse peak was at 1077nm, with bandwidth of 3nm (FWHM) as shown in Figure 4.11 b).

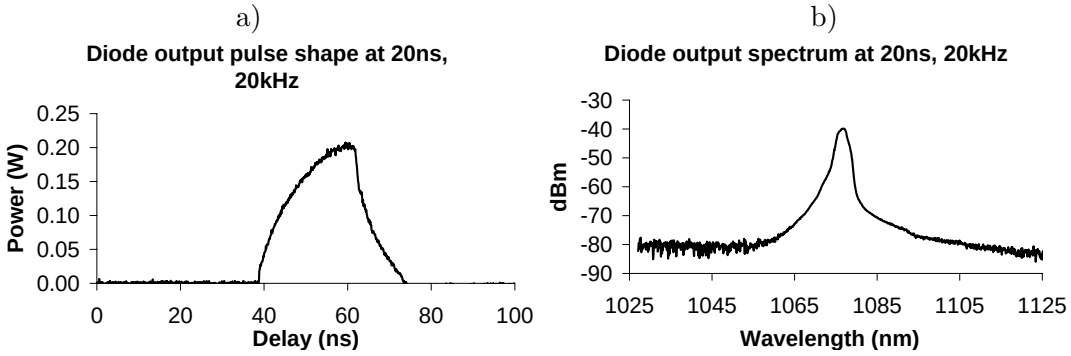

Figure 4.11: Output pulse shape a) and spectrum b) from the diode with at 20ns, 20kHz.

There was no gain saturation and no reshaping as the pulse propagated in GTWave 1. Figure 4.12 shows the pulse shape and the spectrum at the output of the preamplifier and Figure 4.13 shows the measured and calculated pulse shapes together with the gain during the pulse duration. The pulse received a gain of 27dB. The peak power of the pulse was 100W and the average power was 63mW, corresponding to 3.2μJ pulse energy.

Finally, the pulse was amplified further in the postamplifier. Figure 4.14 shows the output power and the gain in the amplifier plotted against the pump power. The gain was higher than in the case of 100ns pulses due to the reduced pulse energy that leads to greater population inversion residual after each pulse. The maximum signal energy obtained with 30W of pump power was 9.2W. This leads to the pulse energy of about 0.45mJ or 4.5 times the saturation energy of GTWave 2.

Figure 4.15 shows the pulse output and the spectrum of the pulse (ASE has been

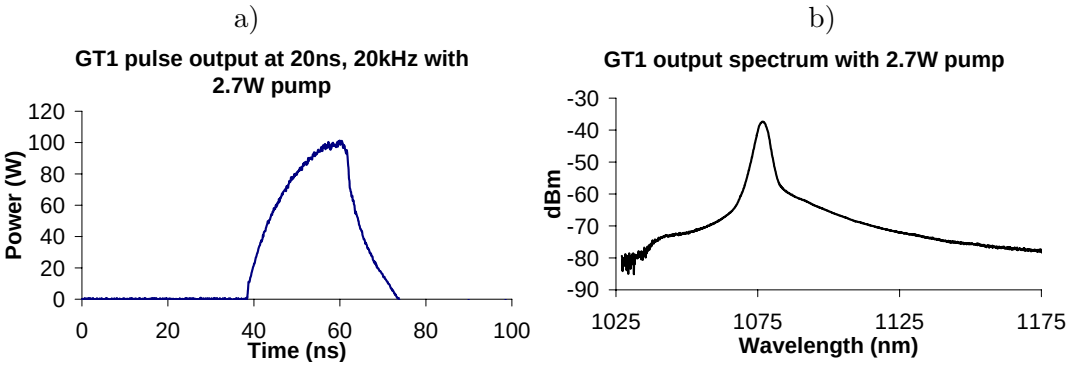

Figure 4.12: Output pulse and spectrum from the GT1 with 2.7W pump.

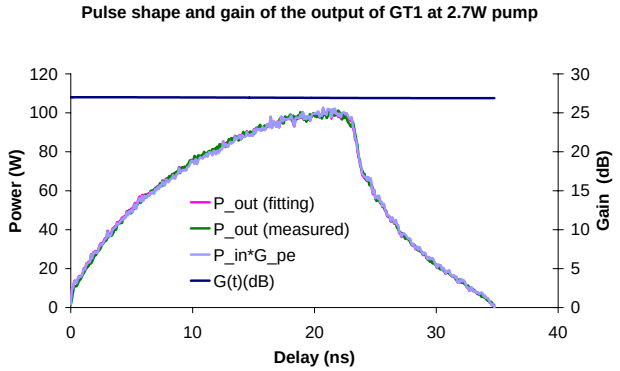

Figure 4.13: Saturation of gain in the GT1 during the pulse. There is no change in gain during the pulse, the gain stayed at 27dB.

removed using the time resolved technique). At low power level, there was some pulse reshaping but it was not very significant. There was a significant degree of pulse distortion at high power even though the pulse is only 20ns long. As the pump power increased, the peak power grows and eventually reaches the SRS threshold. The signal power quickly transferred the energy to new nonlinear components. The power in the peak at 1077nm transferred to the first order SRS peak first, then as the power increased further a second SRS peak was generated. From this point, the more power pump in GTWave 2, the greater the SRS components in the spectrum, at the same time the power of the peak at 1077nm wave reduced.

The same analysis of gain saturation was done on the signal pulse output at 13.7W and 21.7W pump powers. Figure 4.16 shows a significant change in the gain during the pulse. The SRS Stokes was only significant when the peak power was higher than the threshold, which is 13.5kW in this case. At peak powers lower than the SRS threshold, eg. in the 13.7W pump case the signal peak power was 7.5kW and the prediction was very consistent. However, at 21.7W pump or total signal and SRS peak power of 18kW, it also showed

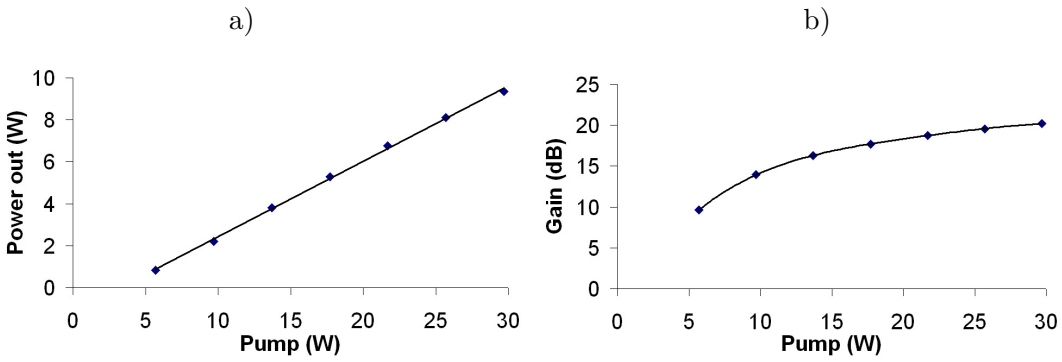

Figure 4.14: Power output and gain on GTWave 2 as a function of pump power.

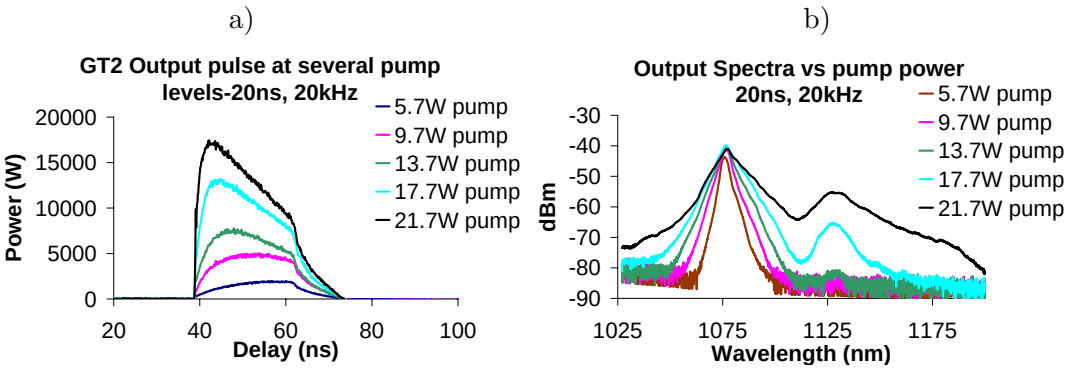

Figure 4.15: Final output power shape and spectrum at several pump powers.

that the predicted and experimental pulses are not consistent. The discrepancy can be explained by the fact that at high peak power, the pulse now contains nonlinear SRS Stokes components. In the simple theory in Chapter 2, the gain was assumed to be homogenous but in this case, the effect of SRS has modified this condition significantly. In addition, the responsivity of the detector is also wavelength dependent, therefore, the measured pulse might be slightly different in the presence of a large amount of new wavelength components generated through nonlinear processes.

The ASE level was also measured using the time resolved measurement. The result is shown in Figure 4.17. The level of ASE was still very small compared with the peak and SRS components. It also indicates that the peak at 1050nm on the overall spectrum belongs to the ASE signal.

4.6 Conclusion

The performance of the MOPA has been investigated for both long pulse and short pulse amplification. For long pulses of 100ns and repetition rate of 20kHz, nonlinearity is experienced, however, the output pulse was reshaped significantly. An output of more than

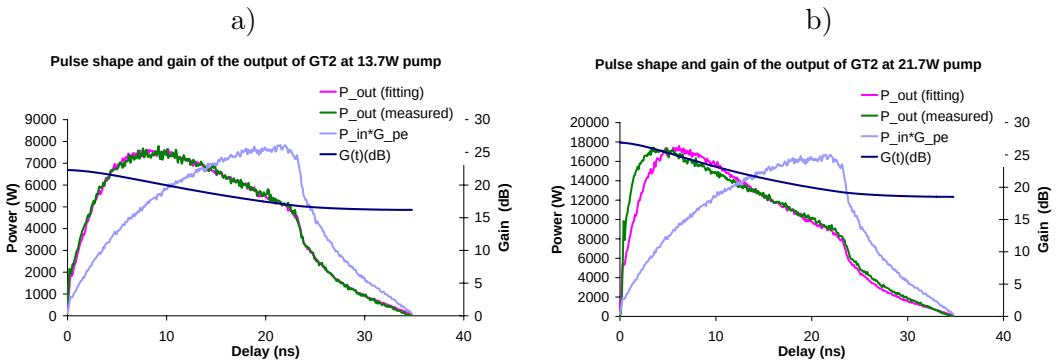

Figure 4.16: Saturation of gain in the GT2 during the pulse at 13.7W and 21.7W pump power with saturation energy of 0.1mJ. The discrepancy in measured and predicted curves the later plot is due to the effect of SRS on the gain distribution.

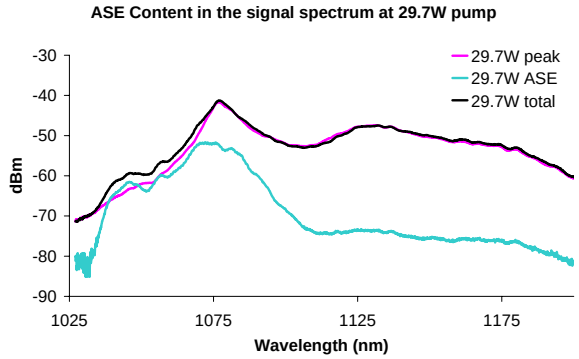

Figure 4.17: Time resolved measurement of the spectrum to measure ASE level, 29.7W GTWave 2 pump, or 9.3W output signal; the amount of ASE was very small at 10dB lower than the peak, but a significant amount of SRS is observed.

0.4mJ has been achieved with the available pump power of 30W. However, the shorter pulse of 20ns at a repetition rate of 20kHz produced a significant amount of SRS at high pump power. The peak power limit was at 13kW with a 3m passive delivery fiber. These results on the amplification work have been used for the SPI pulsed fibre laser product launch at CLEO Europe 2005 in Munich [Ghiringhelli et al. (2005)]. The next chapter investigates the distribution of SRS within the pulse and the dependence of the SRS on the length of the passive delivery fiber.

Chapter 5

Stimulated Raman Scattering in Nanosecond Pulsed Fiber Amplifiers

5.1 Introduction

The previous chapter introduced some characteristics of the MOPA up to the point where SRS starts to affect the output of the postamplifier. This chapter will present results of the investigation on SRS dynamics within the amplifier and the beam delivery fiber by characterizing the temporal shapes of the Stokes and the dependence of the nonlinear effect on the length of the beam delivery fiber.

Setup

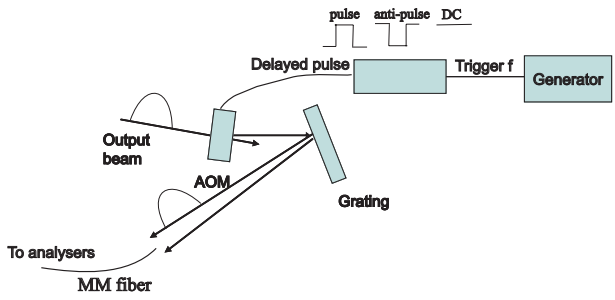

Figure 5.1: Set up to scan the spectrum of the output pulse.

In order to separate different components of the spectrum to analyse each part in detail the setup in Figure 5.1 is used. The AOM was used to gate only the pulse so that no ASE reached the detector. A Bragg grating with 600lines/mm was placed in the path of the extracted output beam. The grating diffracts different wavelengths to different angles.

The spectral content could then be scanned by turning the grating along the vertical axis. A multimode fiber was used to collect the first order diffracted signal. The collected spectral bandwidth of this sytem was about 8nm. This was large enough to catch some of the main feature of the output spectrum including: the signal at 1077nm, the first-order SRS Stokes at 1130nm and the second-order SRS Stoke at 1170nm. At each of these wavelengths, the pulse shape was recorded using an HP Digital Communication Analyser containing a 20GHz bandwidth InGaAs detector.

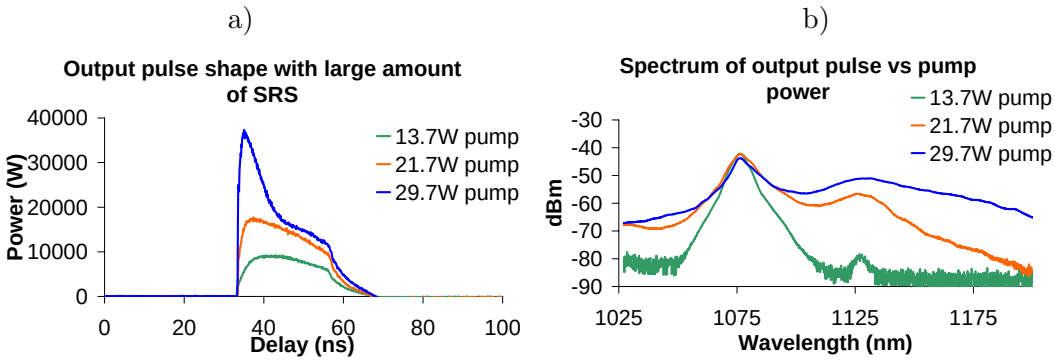

Figure 5.2: Pulse shape and spectrum of the output at very high peak power. The spike of the pulse at 19.7W was due to the higher responsivity of the detector with high wavelength

The delivery fiber at the end of the GTWave 2 was initially left at 3m long. The seed pulse to the directly modulated diode was kept at 20ns, 20kHz. The pump condition for the preamplifier GTWave 1 was also kept as in Section 4.5. The spectra at three different pump levels at which different amounts of SRS were generated were scanned. First the pulse was measured without the grating and results are shown in Figure 5.2 a) for the pulse shape and b) for the spectrum. The two graphs clearly show that there was a large amount of SRS generated when the peak power goes beyond the SRS threshold, which was later measured to be about 13kW.

It is clear that at low powers, ie. below the SRS threshold, there was little pulse distortion. But at very high level of pumping, there are significant pulse distortion on top of the gain saturation as considered in previous chapters. At 29.7W pump power for example, there is a spike at the beginning of that pulse that does not correspond to gain saturation. This spike can be explained based on the responsivity of the detector. The responsivity of an InGaAs detector is relatively flat but increase slightly in the range of the spectrum form: 1000nm to 1200nm. The typical values at 1177nm, 1130nm and 1170nm are about 0.6, 0.62 and 0.7 A/W, respectively. The peak of the pulse contains a large amount of SRS. The detector is more sensitive at higher wavelengths and therefore sees

high power at the peak. The plot in Figure 5.2 indicates the total peak power of about 38kW at 29.7W pump power. However, the calculation did not taken into account the different responsivity of the broad spectrum. When this is done the actual peak power was estimated to be about 30kW.

5.2 Scan for Temporal Shape of Raman Stokes

The next step was to scan the spectrum at the three key points at different levels of nonlinearity. Figure 5.3 shows as an example of the sampling process. The grating spreads different components of the spectrum into different angles. Therefore, it is possible to measured each component separately.

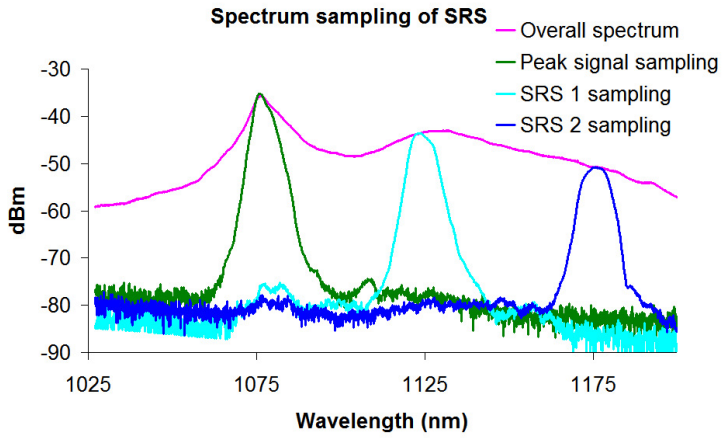

Figure 5.3: The spectrum of the output with high level of SRS was sampled at the signal wavelength, first order and second order SRS.

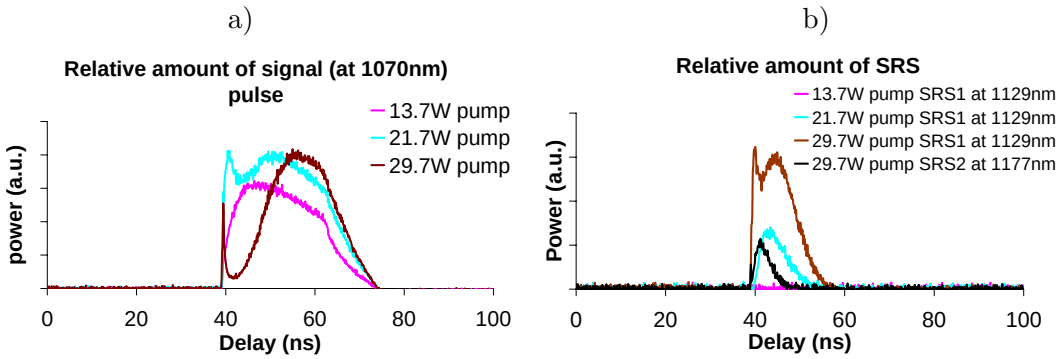

Figure 5.4: The 1077nm signal pulse and SRS Stokes components at various pump powers. The higher Stokes peaks grown at the expense of the lower one (signal wavelength as the zeroth order).

The results are shown in Figure 5.4 a) for the 1077nm signal peak and b) for the Stokes at various pump levels. At low peak power, ie. at 13.7W pump, there was only a very

small amount of SRS generated, at 40dB down from the peak. Therefore the pulse shape of the peak at 1077nm is exactly that of the whole spectrum. However, as the pump power increases, more first-order Raman Stokes was generated. The energy from the peak of signal starts to be transferred to SRS leaving a dip in the middle of the pulse. This dip grows rapidly when more pump power is put into the amplifier. At the maximum power, the dip in the middle of the pulse almost touches zero (ie. complete depletion), the signal pulse starts to widen to encompass leading and trailing edges of the signal pulse. The development of the signal at 1070nm, first and second order SRS component are schematically shown in Figure 5.5. This process is consistent with the simulation done by Wang (2005a).

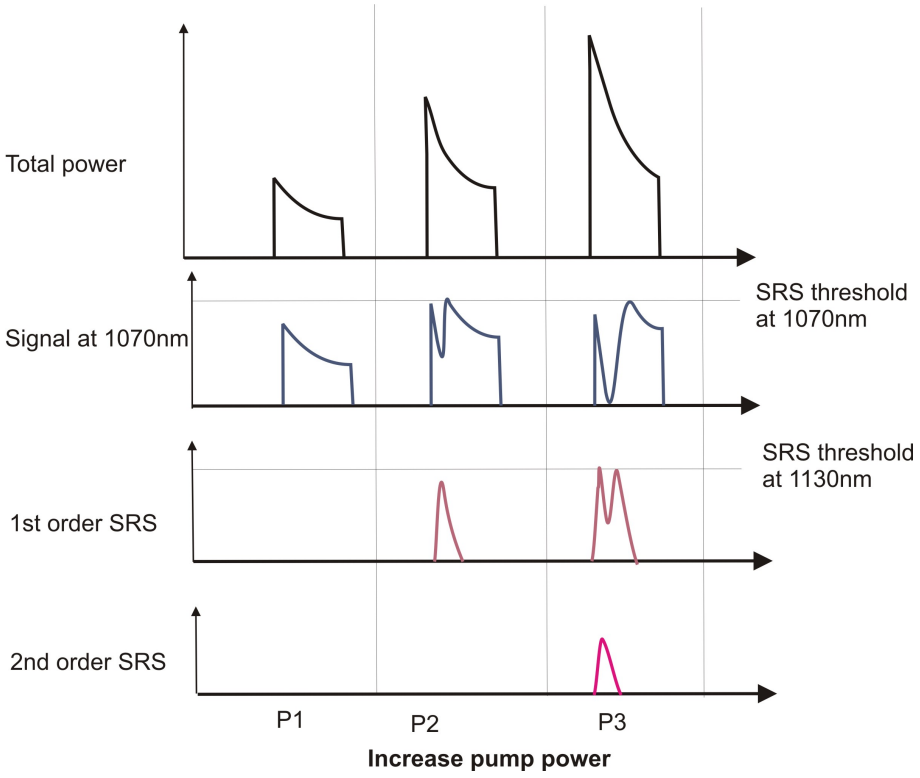

Figure 5.5: The development of different components of the temporal pulse as the pump power increases.

However, at even very large level of pump power, the trailing edge of the pulse is almost unaffected by the nonlinear conversion because the peak power at the tail is relatively smaller than the SRS threshold due to the high level of gain saturation. When the first-order Raman Stokes peak power reached the threshold of around 13kW, a second-order Raman Stokes is generated. The maximum peak power can be achieved at the signal wavelength of 1077nm was 13kW. The more the pump input power to the amplifier, the more the nonlinear components grown and thereby reducing the power at the input signal

wavelength.

Scanning of spectra with a large amount of SRS as done in the previous section has some disadvantage because at each point the collected spectrum only has the bandwidth of about 8nm. At very high levels of pump, the peak signal wavelength broadens significantly and the bandwidth of the SRS components was also much larger than 8nm. When the multimode fiber collects light at the signal wavelength it misses light in the pedestal on both sides of the peak area. Also, data from a scan of three points within the spectrum does not allow full calculation of the true peak power of the pulse.

In order to understand the dynamic of SRS further and to measured the SRS threshold more accurately, a Thorlabs fast silicon and an InGaAs detector were used. The silicon detector has a spectral response which cuts off at 1100nm, while the InGaAs detector responds to the whole spectrum. Therefore, the silicon detector only detects the 1077nm peak of the pulse and does not respond to the SRS components. The pump power was adjusted so that the SRS peak was at 20dB and 10dB below the peak level. The pulse shapes at these points were recorded by the InGaAs and the Silicon detectors. The two sets of data were then scaled on the same graph to get accurate values for peak power and pulse shapes of the pulse at 1077nm. The results are shown in Figure 5.6. The signal detected by the silicon detector levels out at a peak power of about 13kW. A gap at the peak between the pulses detected by the Silicon and InGaAs detectors developed as the pump power increased. The power associated with this gap equals the total power of the SRS components.

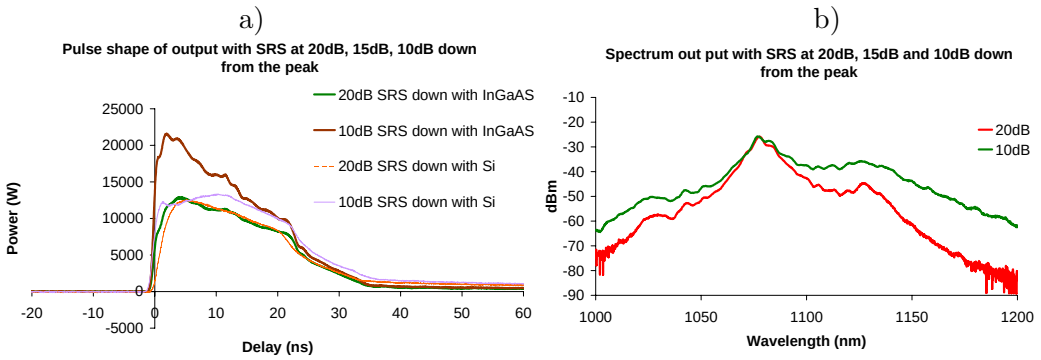

Figure 5.6: Pulse shapes detected by Silicon and InGaAs detectors with SRS level at 10dB, 15dB and 20dB lower than the peak.

5.3 Dependence of SRS on Length of Fiber

The amplification of Raman Stokes is very sensitive to the input power at the wavelength of the Stokes wave. The spectrum of the output of the preamplifier has a pedestal that extends as far as 1200nm as seen in Figure 4.12 b). In order to determine the effect of the ASE from the preamplifier on the amplification of SRS a Wavelength Division Multiplexing (WDM) coupler that separates 1077nm and 1130nm was spliced to the input of the postamplifier. This allows only wavelength in the region of 1077nm to enter the postamplifier and removes the component at 1130nm so that first order SRS Stokes does not have any initial seed intensity. The results showed that, the effect of the WDM was very minimal. There was no change of the threshold of SRS in the presence of the WDM. Therefore, it is safe to conclude that SRS was only generated in the postamplifier and the beam delivery fiber.

The nonlinear effect depends on both the peak intensity of the pump and the length of the interaction. The above set up was done on a fixed length of delivery fiber. It has been believed that the SRS was generated mainly within the delivery fiber because the GTWave 2 was counter pumped, the signal only received significant amount of energy right at the end of the amplifier. In order to give any conclusion about this assumption, the SRS threshold was measured against the length of the delivery fiber. Several lengths of delivery fiber were used in the experiment similar to the ones in last section where an InGaAs and a Silicon detector was used to measure the SRS threshold.

The SRS threshold Equation 2.45 can be written in the form:

$$P_0^{cr} = 16\frac{A_{mode}}{g_R L_{eff}} = \frac{C}{l_{eff} + L} \tag{5.1}$$

where $C = 16A_{mode}/g_R$ is a constant value depending only on the fiber characteristics, l_{eff} is an effective length where the pulse travels within the amplifier and L is the length of the beam delivery fiber. The total effective length taken as a sum of l_{eff} and L was a reasonable approximation as the loss on the delivery fiber is relatively small. As an indication, the mode field diameter of the fiber was calculated to be 17μm, or $A_{eff} = 231\mu m^2$. $g_R = 1 \times 10^{-13}$m/W at $\lambda = 1077$nm then $C = 8.1 \times 10^4$Wm. The total length of the amplifier was about 7m, the total gain of the pulse is generally at about 20dB, but because it operates with a backward pumping scheme the effective length was much shorter as the signal pulse only received the power right at the end of the amplifier. The calculation of

exact value of l_{eff} requires the detailed gain distribution in the postamplifier and the value of l_{eff} changes with different total gains or pump powers. However, it can be estimated by using the expression

$$l_{eff}(L) = \frac{1 - e^{-\alpha_p L_0}}{\alpha_p}, \tag{5.2}$$

where L_0=7m is the length of the amplifier, α_p is the gain calculated by $\alpha = ln(G)/L_0 = 0.65$ for $G = 20dB$ case. Therefore l_{eff} is approximately 1.5m.

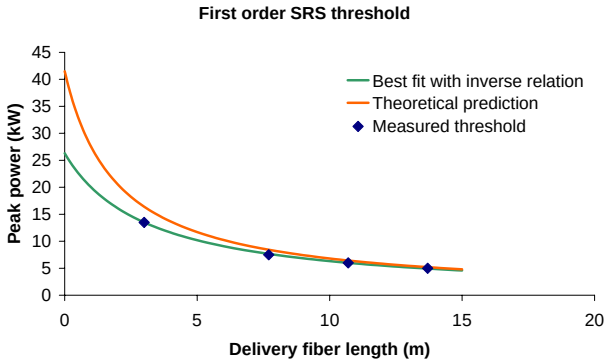

Figure 5.7: The peak power of the signal at 1077nm at the output of the delivery fiber at various lengths. The diamond points are the measurement data, the green curve is the best fit line using Equation 5.1, with C=8.3×10^4Wm and l_{eff} = 3.6m. The red curve is the theoretical prediction with l_{eff} = 1.5m and C=8.1×10^4Wm.

Figure 5.7 shows the experiment results and the prediction using the parameter just as discussed. It clearly indicates that at long delivery fiber length, the calculated value agrees with the measurements very well. However, at short length, there was large discrepancy between measurement and theory. The reason behind that was due to the dependence of the value of l_{eff} on the total signal gain. At very long fiber length, the value of l_{eff} has little impact on Equation 5.1. l_{eff} was actually decreasing as the pump power (energy gain) increased. Therefore, a constant value of l_{eff} only gives a rough approximation of the effective length.

The experimental result clearly indicates that the SRS threshold would be reached at a value of 25kW even when the beam delivery fiber is very short. However, in this experimental setup cutting the beam delivery fiber further was not possible due to the fact that it was protected in a steel tube of a length of about 3m.

5.4 Photonic Bandgap Fiber for High Power Delivery

The above experiment has shown that the amount of SRS generated in the delivery fiber was very significant. To achieve high peak power without nonlinear effects, a very short beam delivery fiber must be used. This is not favoured in industrial applications where long delivery fiber must be used to guide the beam from the laser source to the working area. One possible solution is to use the Photonic Bandgap fiber (PBGF). The PBGF confines light into a hollow air core surrounded by array of air hole at even spacing. It guides light by the photonic bandgap effect. Because the light wave only travels in the air core, there should not be any nonlinear effect introduced even at very high peak intensity. This simple experiment will try to verify this statement.

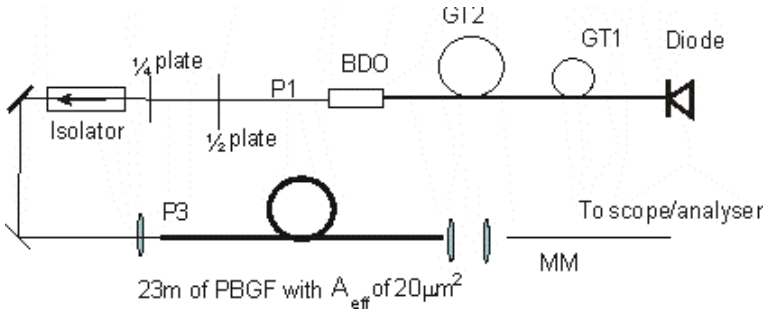

Figure 5.8: The setup of SRS generation in the PBGF. The output beam of the beam delivery optics (BDO) is coupled into 23m of bandgap fiber.

A piece of 23m of PBGF was used in the setup as shown in Figure 5.8. The PBGF has a mode field area of $20\mu m^2$ and a loss of 0.3dB/m. Hence the effective length for this fiber is 11.5m. The transmission of the PBGF is as shown in Figure 5.9, the centre wavelength is around 1100nm. The lower cutoff wavelength is below 1050nm and the upper cutoff wavelength is above 1200nm. Because of several factors including the use of the isolator, the two waveplates, coupling lens and the mismatch between the modes of the BDO and of the PBGF, the power coupled into the core of the PBGF was only 10% of the power at the output of the postamplifier. However, due to the different mode diameters, the intensity within the PBGF was very similar to that inside the beam delivery fiber. The length of the beam delivery fiber was 5m. The output of the postamplifier contains large amount of SRS Stokes before it enters the the PBGF. The spectrum at the output of the PBGF was recorded and compared with the input.

Figure 5.9 shows the measurement result. It clearly shows that the SRS level stayed the same after travelling a length of 23m (effective length of 11m) of fiber. There was no

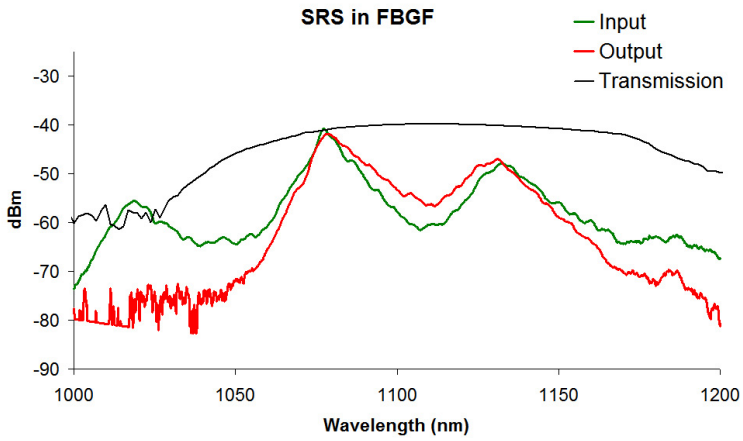

Figure 5.9: The spectra of the input pulse and output pulse of the PBGF and the transmission of the PBGF.

additional amount of SRS generated within the PBGF. There is only a filtering effect on the output spectrum due to the pass band of the fiber.

This indicates that it is possible to use the PBGF as the beam delivery fiber without introducing any SRS components. The PBGF can be spliced directly into the signal fiber of GTWave 2. However, to reduce the loss due mode mismatch, the mode diameter of the PBGF should be increased to match that of the delivery fiber in the setup. Also, more work on the handling of the PBGF should be investigated as it is not possible yet to splice the PBGF directly to the beam deliver fiber. However, PBGF is certainly a candidate to consider for delivering high peak power pulse without introducing unwanted nonlinear effects.

5.5 Conclusion

This section has investigated in detail the dynamics of SRS generated by high peak power pulses. It is shown that, the signal energy transferred to the Raman Stokes signal vary rapidly once the SRS threshold has been reached. The maximum peak power of the signal the end of the beam delivery fiber should ideally be kept below the SRS threshold. The amount of SRS generated depended greatly on the length of the delivery fiber. The use of a suitable PBGF would reduce the effect of SRS significantly.

Chapter 6

Active Pulse Shaping with Directly Modulated Diode

6.1 Introduction

In this chapter we demonstrate active shaping of the driving electrical pulses in a laser diode to produce customised output optical pulse shapes from a fiber amplifier, compensating for the pulse shaping effect of gain saturation. One of the many advantages of a MOPA system is the capability of directly controlling the seed source. The directly modulated diode can be seeded with a waveform from an arbitrary waveform generator (AWG) so that the output pulse achieves a specific desired pulse shape. This capability allows the adaptive pulse shaping algorithm to be performed. Three different types of output pulse are targeted in this demonstration: square, triangular and two-step. The adaptive process is performed automatically using a computer code written in Matlab.

6.2 Setup

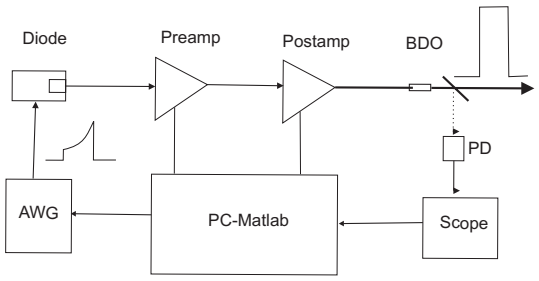

Figure 6.1: Setup for active pulse shaping in fiber MOPA.

In the previous chapter, the directly modulated diode is driven by a board which has a voltage trigger. This board supplies a constant current to the diode for the duration when the trigger voltage is greater than a threshold voltage. Therefore, it is not possible

to produce arbitrary pulse shapes using the capability of the AWG. A new electrical driver board was thus built to make pulse shaping possible. The diode driver delivers an instantaneous current to the diode that is proportional to the instantaneous voltage from the AWG. The output of the diode generally follows the seeded input pulse other than for some fast ripple due to the drive electronics. In order to avoid electrical noise from the power supply board passing to the diode, the board was designed with a cutoff voltage, where below this level no electrical current can be passed to the diode. The cutoff voltage set by the drive electronics is 10% of full voltage, so the system effectively has 10dB dynamic range.

Figure 6.1 shows the setup of the experiment. The output from the diode is seeded to the cascaded amplifier consisting of a preamplifer and a postamplifier as that in the previous chapter. The two amplifiers are controlled directly by the computer. The drivers of the pumps of the two amplifiers are turned off whilst the AWG is reprogrammed to avoid self-pulsing in the absence of a signal. The output of the system is monitored by measuring the signal pulse shape using a fast InGaAs photodetector using a digital scope and the corresponding data transferred to the computer. The photodetector does not distinguish between power at the signal wavelength and power at Stokes shifted wavelengths due to SRS. However, we know from spectral data that SRS was minimal for all pulses where the peak power does not exceed ∼13 kW for 3m of delivery fiber. The computer analyses the output pulse shape and compares it with the desired pulse shape. It then determines the fitness factor and decides a new pulse shape to feed to the AWG using the Simulated Annealing (SA) optimisation method. The loop keeps searching until the final output pulse is within the specified tolerance of the desired pulse shape. Simulated Annealing is preferred over other optimisation methods such as Simplex Method and Genetic Algorithm. The Simplex Method tends to get lock onto local maxima or minima. Genetic Algorithms search global maximum or minimum but requires a large number of iterations.

Figure 6.2 a) shows the diode output when it was driven by a square electrical pulse of 100ns. The fast ripples on the pulse are due to the drive electronics, this is intrinsic to this driver board design and cannot be corrected by the AWG. The preamplifier is set with the gain at about 27dB. The output of the final amplifier at various pump power levels is shown in Figure 6.2 b). Figure 6.3 shows the theoretical fitting the pulse shapes at the output of the postamplifier [Siegman (1986) and Frantz and Nodvik (1963)]. It clearly

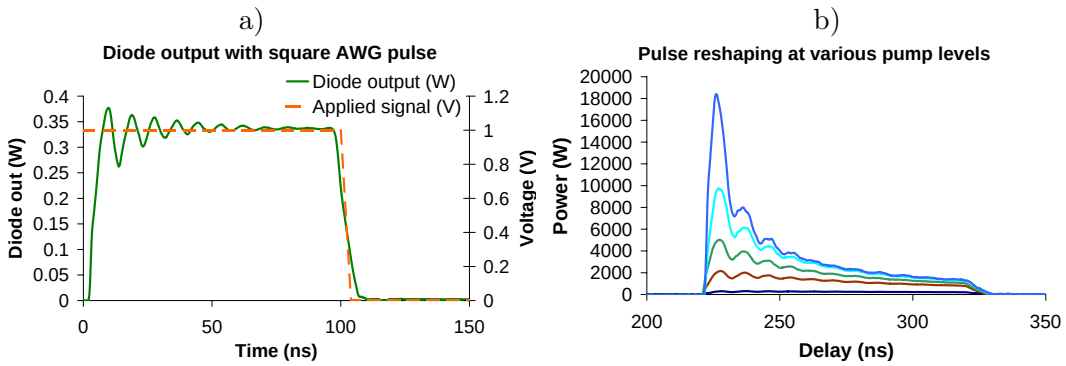

Figure 6.2: Output pulse shapes of the diode and the of the postamplifier at various pump powers.

shows that despite the ripples on the input pulse, the simple theory of the gain saturation considered in the previous chapter is still consistent with the experiment.

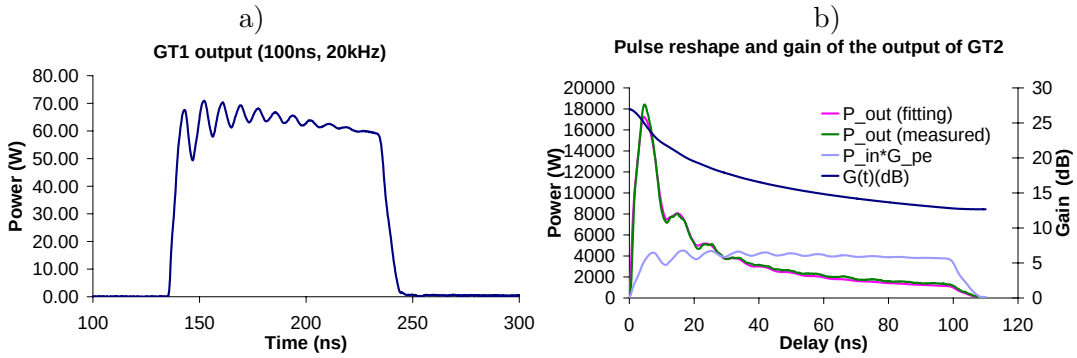

Figure 6.3: The experimental and theoretical output pulse shapes of the amplifiers with a square AWG output.

One of the main targets of this project is to improve the pulse energy and peak power of the output without introducing too much SRS power. To do so, the output pulse should be as square as possible so that there is no spike to initiate the nonlinear effect. As we know from the previous chapter a square input pulse to the amplifier will produce an output pulse with a spike at the leading edge of the pulse and the pulse tail will follow an exponential drop. Therefore, it follows that in order to produce a square pulse an exponentially ramped pulse should be used as an input for the postamplifier to achieve a square pulse at the final output. Figure 6.4 shows an example of an exponentially ramped input pulse that produces a square output pulse that keeps the total pulse energy (the total energy gain) the same, but for which the peak power has been reduced significantly and therefore that allows SRS to be eliminated.

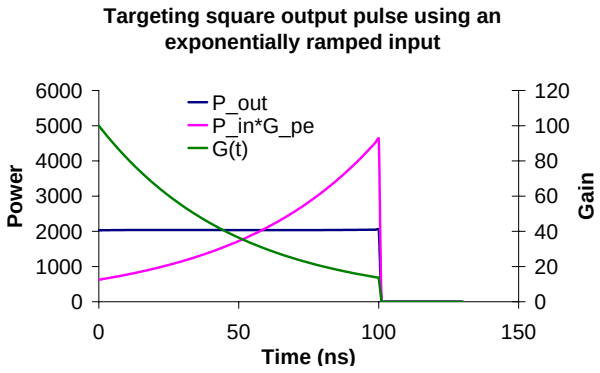

Figure 6.4: An exponential ramp input to produce a square output pulse.

6.3 Pulse Shaping Parameters

The Tektronix AWG 2021 can produce any arbitrary waveform with a resolution of 4ns. For a typical pulse duration of 100ns, the AWG output signal can be formed by specifying the amplitudes of 25 points. So in adaptive process, 25 variables could be used. For this particular experimental set up, the amplifiers have to be turned off during the waveform transfer from the computer to AWG, which takes a reasonable amount of time and so an algorithm which involve 25 variables would take a very long time to finish. Therefore, an alternative with many less variables has to be used.

A sensible option is to use a pulse consisting of several smooth curves which use a small number of variables to define. Because gain saturation follows an exponential term, exponential curves are suitable choice. In this experiment, each curve between the two points A (T_0, l) and B (T_f, l) as seen in Figure 6.5 is characterised by

$$y(t) = l + \frac{h - l}{e^{\alpha(T_f - T_0)}}(e^{\alpha(t-T_0)} - 1) \tag{6.1}$$

where T_0 is the starting time, T_f is the the end time of the curve, $T = T_f - T_0$ is the duration of the curve; t is the time between T_0 and T_f; α is an exponential factor, if α is positive the curve is concave, if α is negative the curve is convex and α cannot equal zero but it can approach a very small number to give a straight line between the two points A and B.

Figure 6.6 shows examples of the input pulses applied to the driver board in order to produce a square, a triangular or a two-step pulse. To achieve a square pulse, it is only necessary to change two variables: l the high of the front of the pulse and the α exponential term of the main curve as shown in Figure 6.6 a). Similarly, by choosing the

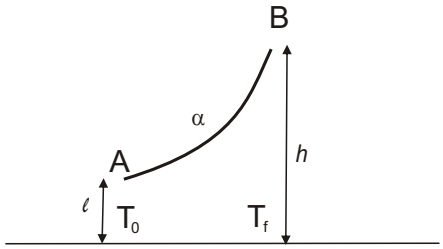

Figure 6.5: Element curves to characterise the AWG output.

right variables the triangular and two-step pulses also require only two variables to be used in the adaptive process to achieve a reasonably good quality output pulse. This makes the adaptive process much quicker than using individual co-ordinates for each point on the pulse. Furthermore, much less information is needed to be transferred between the computer and the AWG, again speeding up the optimisation process.

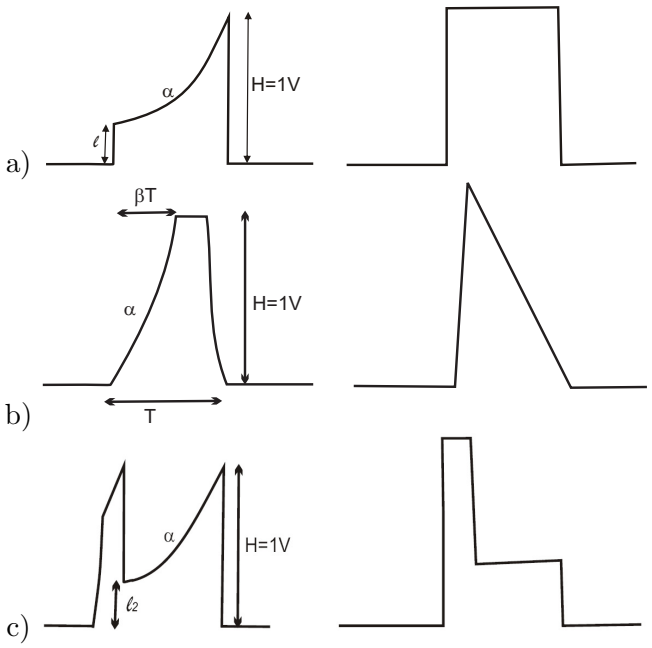

Figure 6.6: Estimate of the inputs (on left) to give desired square, triangular and step pulses (on right).

6.4 Simulated Algorithm for Active Pulse Shaping

The search method used in this demonstration is based on the Simulated Annealing method, which was invented by Kirkpatrick et al. (1983). This method was inspired by the annealing method in metallurgy, in which a material is heated up and slowly cooled down to maximise the size of the crystal and to minimise the amount of defects. This

process is equivalent to reducing the energy state of the system down to a minimum value. Due to random motion of the atoms in the materials, a system initially stuck in one local state might jump out of that state to a new one. If the new state has lower energy than the initial one the system stays there, but if the new state has higher energy, there is only a low probability that it will stay at the new state. By some random upward jumps to higher energy levels and slow lowering of the temperature, the system slowly evolves to the local minimum of total energy.

For the Simulated Annealing method to work a fitness factor (which is equivalent to the energy of the system) has to be specified. The simplest one is the percentage of area difference between the actual output pulse and the target pulse over the area under the target pulse. To be more specific, assume the actual pulse shape is specified by the function Y(i), where i is the index (equivalent to time), and the desired pulse is specified by the function D(i), then the fitness factor is defined as:

$$F(l, \alpha) = \frac{\sum_i |Y(i) - D(i)|}{\sum_i D(i)} \tag{6.2}$$

where l and α are the two variables that are being searched to give the minimum fitness factor.

Only one variable is searched at any time to find a minimum value of the fitness factor F. During that run, the fitness factor is measured for every new value of the variable. Then it is compared with the previous values, if the new fitness value is smaller than the previous one, the new state is chosen to continue. However, if the new fitness value is greater than the previous one, a random number is generated and compare with a fixed number to decide whether the new waveform will be chosen to continue or not.

The pseudocode can be described as following:

```
START with initial values of variables
MEASURE F
WHILE (F < target value and iterations < set maximum)
    SEARCH variables 1 until F is MINIMUM
        WHILE (number of iterations < a set number)
            GET new values of of variable 1
            MEASURE F
            DECIDE where to go next
                MOVE (always) to next state if F decreased
```

```
            MOVE (occasionally) to next state if F increased
        ENDWHILE
    SEARCH variables 2 until F is MINIMUM
        WHILE (number of iterations < a set iteration)
            GET new values of of variable 1
            MEASURE F
            DECIDE where to go next
                MOVE (always) to next state if F decreased
                MOVE (occasionally) to next state if F increased
        ENDWHILE
    SEARCH ...continue to all other variables.....
REDUCE the temperature
ENDWHILE
RETURN THE BEST PULSE
```

6.5 Results

Figures 6.7 to 6.9 show the results for three cases of a square, a triangular and a two-step pulse. The final output pulses are shown on the right and the input pulses are shown on the left. It required ∼15 measurements of the fitness factor F to converge to an optimum condition.

The output pulse from the diode is significantly different from the applied input due to the response of the drive electronics and the diode. The final output pulses of the MOPA were close to the targeted pulses. Clearly, the ripple on the diode pulse, which was too fast to be fully compensated for by the AWG, reduced the quality of the output pulses to some extent. This should be improved upon with better designed drive electronics.

The output of the square pulse has an energy of 0.2mJ with a peak power of 2.6kW, Figure 6.7. These numbers are much less than the possible power provided by the MOPA at full power. The limitation in achieving higher energy square pulses was imposed by the restricted usable dynamic range of the diode. The square output peak power obtained was relatively small. This was due to the fact that the postamplifier could not be pumped at higher powers because of instabilities in the output pulse. The diode threshold is about 0.1V. Therefore, the input electronic ramp pulse as shown in Figure 6.7 led to the fact that the leading part of the pulse was at a level that was very close to the threshold. The pulse contained an oscillatory leading edge which introduced a high level of instability

when travelling through the high gain amplifiers. Despite of this the final F factor is only 0.08 (8%) corresponding to 92% agreement.

The dynamic range of the source should be increased in order to get higher peak power at the output with a square pulse. However, the system worked well for pulses that did not required a low front-end input.

As a demonstration of the versatility of the system, a triangular and a two-stepped pulse with duration of 100ns and 200ns, respectively, were obtained. In order to make the modifications to the program simple, only two parameters were used in the algorithm for both pulses. The other parameters were chosen based on experience. For the triangular pulse, the input consisted of three sections: an exponential rising edge, a flat top and a linearly decreasing tail. The two variables used in shaping are the exponential factor α and the duration T of the first section. The output triangular pulse fitted to the target very well with an agreement of 96% (F=0.04) as seen on Figure 6.8 b). The pulse has a peak power of 10kW and a pulse energy of 0.45mJ.

The two-stepped pulse could be considered as two consecutive square pulses at different power levels. In this case, the target durations of these pulses were 50ns and 150ns. This two-step pulse required 8 parameters to fully define it. However, only two critical parameters were used. They were the height of the initial point l and the exponential factor α of the second rising feature. The front part of the pulse was fixed. An example of the resulting two-stepped pulse is shown on Figure 6.9 b). The first part has a peak power of 4kW, and the second part has peak power of 1kW. Again, the output was very close to the desired target, with F=0.05.

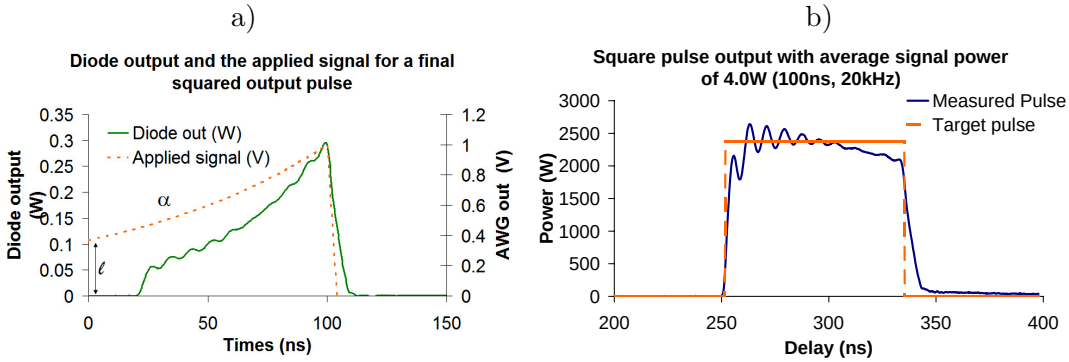

Figure 6.7: Shaping to achieve square pulse at the output.

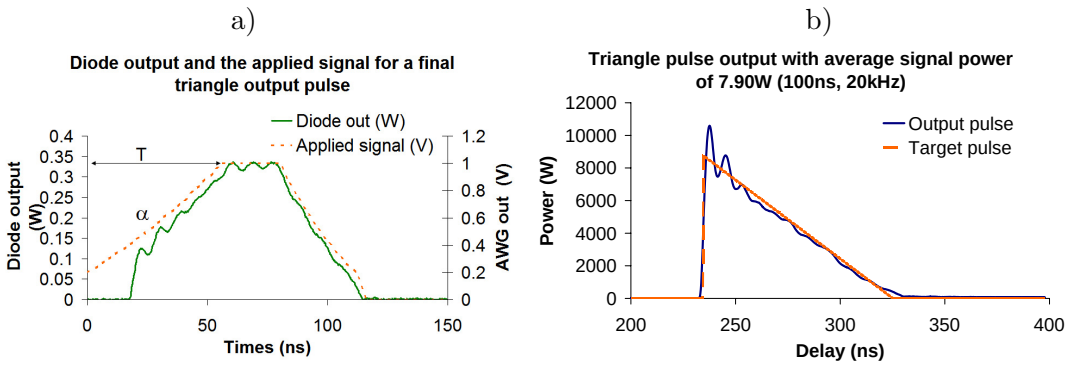

Figure 6.8: Shaping to achieve triangle pulse at the output.

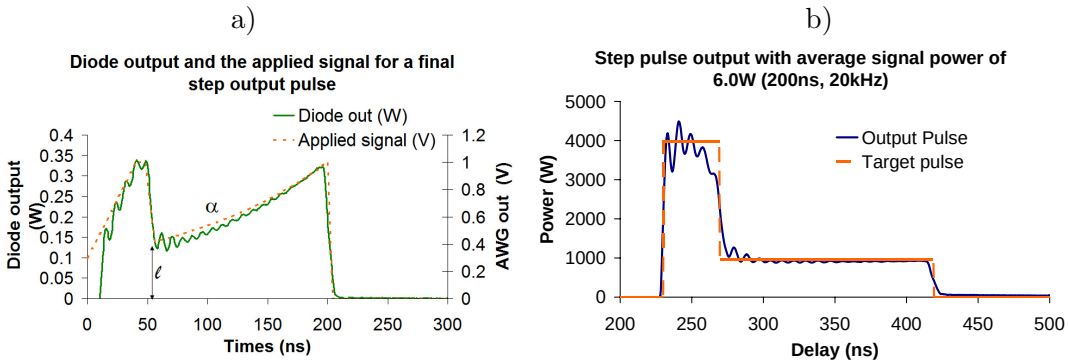

Figure 6.9: Shaping to achieve two-stepped pulse at the output.

6.6 Conclusion

It is clear that direct modulation is an effective and versatile method of controlling pulse shape in fiber amplifiers. The main limitation is the dynamic range of the diode output before noise becomes a significant issue. Improved drive electronics for the diode or a method of shaping the pulses at a point between the diode and the amplifiers using an Electro-Optic Modulator should allow even better pulse shape control. Next chapter will focus on using an Electro-Optic Modulator to shape the input pulse. This provides a much higher extinction ratio as required for shaping of pulses at high level of gain saturation.

Chapter 7

Active Pulse Shaping of 1mJ MOPA Using EOM and Raman Pulse Generation

7.1 Introduction

Chapter 6 demonstrates the principle of active pulse shaping. However, with the oscillatory output of the diode, the shaped output pulses were not as clean as they should ideally be. Also, the dynamic range of the diode is inadequate. Since the oscillation lasts for about 100ns, after this period the diode output is generally a flat pulse. Using an Electro-Optic Modulator (EOM) with the response of few gigahertz, it is possible to carve the smooth part of the pulses to an arbitrary shape with high resolution, and to suppress the oscillatory feature to high extinction ratio. Therefore, this chapter further develops pulse shaping techniques using an EOM as a shaping component. With a much higher extinction ratio and fast response to the arbitrary electrical signal, this shaping method has much higher capability to create higher quality pulses at the output of highly saturated amplifiers. Furthermore, the number of variables used in the adaptive process can in principle be arbitrary. Once the output pulse is square and at high power, the Raman-free pulse at the output can then used to pump a long piece of single mode fiber to generate Raman peaks. This chapter will demonstrate that it is possible to generate only one Raman peak at a time unlike the data in Chapter 5 where only a broad band of Raman was generated.

7.2 Pulse Shaping with an EOM Setup

First, a MOPA with a new postamplifier configuration was set up as as shown in Figure 7.1. The seed diode is the same diode as used in the previous chapter, a directly-modulated

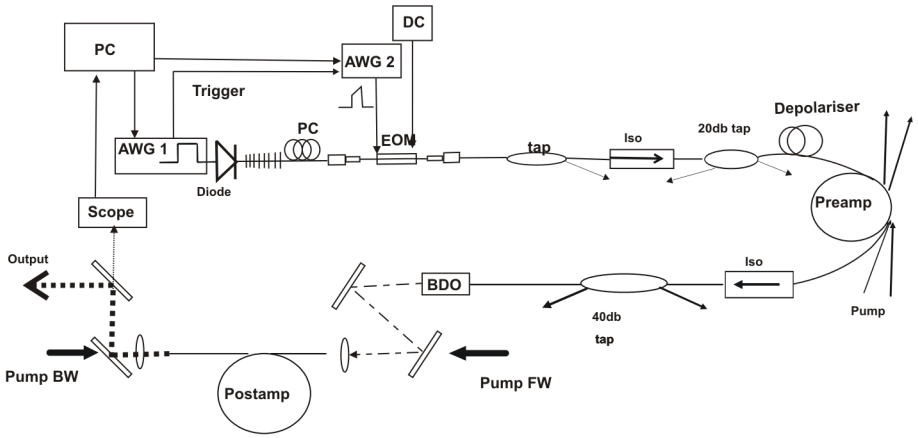

Figure 7.1: Active pulse shaping with EOM setup.

diode mounted on a print circuit board seeded by an electrical signal from a square pulse generator (AWG 1). This set up is capable of producing pulse with duration ranging from a few nanoseconds to a few microseconds at repetition rates from a few Hz to few hundred kHz. The diode is grating-stabilized to produce a laser output at a wavelength centred at 1077nm with a bandwidth of 0.3nm. An arbitrary pulse generator (AWG 2), a Tektronix AWG2021, is used to drive the EOM. The AWG 2 was triggered with a sync signal of the AWG 1. The AWG 2 was controlled by a Matlab code on a PC. The AWG 1 was programmed to generate a square pulse of sufficient long duration for the EOM to shape the pulse. The waveform generated on the AWG 2 was programmed to shape the smooth part of the diode output pulse and suppress the rest of the diode output.

The diode has a peak output power of 200mW. After some loss within the EOM, connectors and the isolators, the peak power before the preamplifier is around 25mW. The preamplifier is also the same one that has been used in the previous chapters. It is a single mode GTWave amplifier with a gain of around 28dB. This amplifier produced the peak power of around 20W after the beam delivery optics (BDO).

The postamplifier was configured in an end-pumped configuration. The fiber has a core diameter of 30μm and a cladding diameter of 300μm. The numerical apertures of the core and cladding are 0.06 and 0.4, respectively. This fiber was characterised in Chapter 3 as fiber LF128. The index profile of the fiber is shown in Figure 3.1 a). Due to the relatively large core size, the output of the fiber is slightly multimoded at the coiling radius of 20cm in diameter.

The postamplifier was pumped at both ends with a total amount of incident power of up to 33W at 915nm. The fiber has an absorption of 1.8dB/m at 915nm. The length

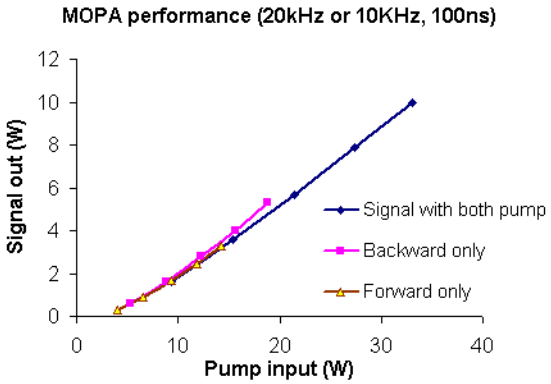

Figure 7.2: Output power of MOPA.

of the fiber was 3.5m. This restricted length had to be used due to the shortage of large mode area fiber after the Mountbatten building fire which destroyed not only the fiber drawing facility but also all of ORC reserve fibers. The slope efficiency of this fiber was approximately 66%. Figure 7.2 shows the performance of the MOPA when it was operated at 100ns pulse width at a repetition rate of 20kHz or 10kHz. The highest average output signal used was 10W. This clearly shows that it is straight forward to achieve a 1mJ pulse if the MOPA is operated at 10kHz.

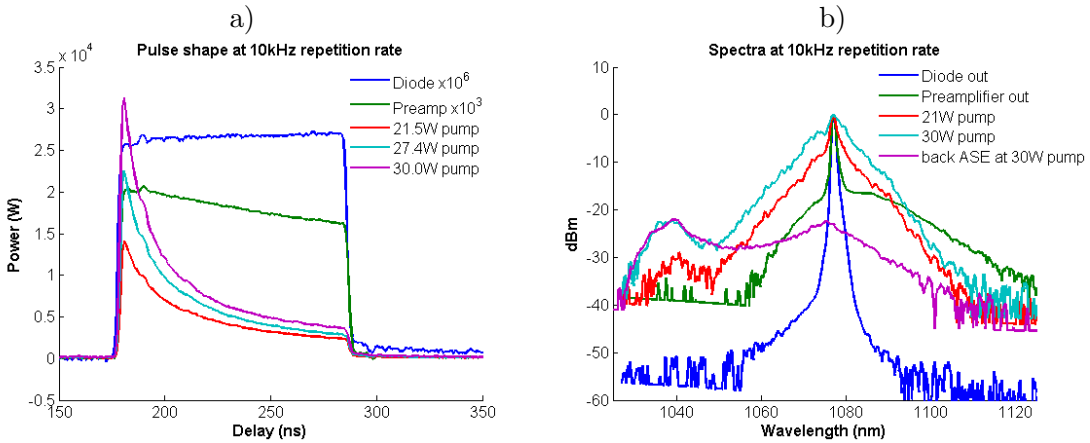

Figure 7.3: Output pulses and spectra of MOPA run in an unshaped mode

Figure 7.3 shows the pulses and spectra of the MOPA at different pump power. The AWG 2 was programmed to generate a square pulse of 100ns at 10kHz. The Figure 7.3 a) shows the shapes of the diode, preamplifier and postamplifier outputs at different pump powers. The peak power could reach as high as 32kW at the peak of the pulse at the maximum pump power of 30W. Also, the pulse energy reached 1mJ when maximum power of 30W of the pump was used. Figure 7.3 b) shows the spectra of the diode, preamplifier, postamplifier outputs and the backward ASE of the postamplifier. These graphs indicate

that there is very a small amount ASE. Also, the spectrum of the postamplifier output was greatly broadened at high peak power. This broadening is caused by self-phase modulation.

7.3 Pulse Shaping Algorithm

As seen in Figure 7.1, my adaptive setup consists of two important components: the shaping part (AWG 2 and EOM) and the detection part (detector and oscilloscope). The AWG 2 is a Tektronix 2021 AWG series arbitrary pulse generator with a maximum resolution of 250MHz (4ns). The signal is then acquired by a digital oscilloscope, Tektronix TDS5032B, which has a resolution of 350MHz.

As discussed in Section 6.3, a waveform can be divided into a number of segments, each segment can be described mathematically by 3 parameters: final y-coordinate, exponential term and duration of the segment as shown in Equation 6.1, and Figure 6.5 and Figure 6.6. The initial y-coordinate is not required because it is equal to the final y-coordinate of the previous segment. The initial y-coordinate of the first segment is always set at 0. An arbitrary number of segments can be chosen for any target pulse shape. Examples are shown in Figure 7.4 for the two cases of a simple square pulse and a two-stepped pulse. The square pulse only requires two segments (6 variables) while the two-stepped pulse requires 4 segments (12 variables).

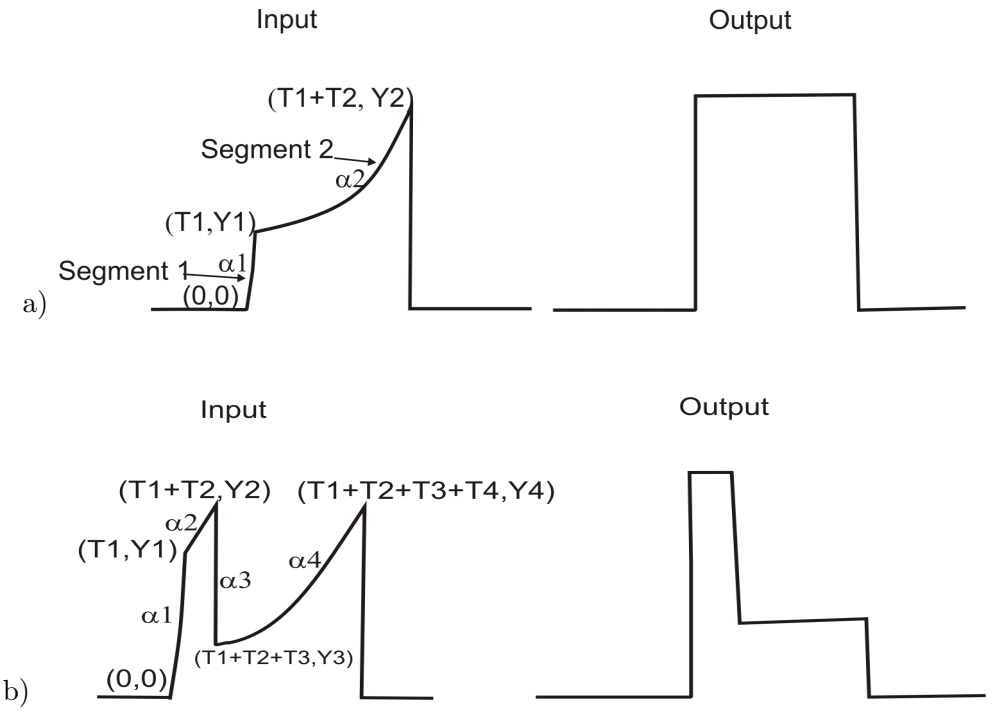

Figure 7.4: Estimate of the inputs (on left) to give desired square, and step pulses (on right).

Despite the significant increase in the number of variables needed to generate these pulses, the number of iterations does not need to increase correspondingly because the algorithm allows the customisation of iterations for each variables. For instance, for the case of a square pulse, the exponential and duration of the first segment can be fixed to a minimum value and the only variable that need to be changed during the run is the y-coordinate. It is, therefore, wise to set the maximum number of iterations for the exponential and duration to be a minimum, say 1. The total number of iterations required is then reduced significantly.

The main algorithm to search for the optimum waveform is based on the Simulated Annealing (SA) method [Kirkpatrick et al. (1983)]. Section 6.4 describes the algorithm in more detail. Since the number of variables can be arbitrary, the algorithm has been also generalised to accommodate this changes. The pseudocode is described as following:

```
START with initial values of variables
MEASURE Fitness F
WHILE (F < target value and iterations < set maximum)
    FOR i=1 to Number of variables SEARCH variable i until F is MINIMUM
        WHILE (number of iterations < a set number)
            GET new values of of variable i
            MEASURE F
            DECIDE where to go next
                MOVE (always) to next state if F decreased
                MOVE (occasionally) to next state if F increased by some probability
        END WHILE
    END FOR
REDUCE the temperature for annealing
ENDWHILE
RETURN THE BEST PULSE
```

The fitness factor F is calculated by the absolute difference between the target and the obtained pulse by Equation 6.2.

In order to provide the adaptive process the best starting point, a simple gain, saturation calculation and a simulation was done to estimate the best initial starting point. To work out the gain of the system, an initial input was chosen and the output was then fitted with a small signal gain G_0 and a saturation parameter U_{sat} using Equation 2.25. The fitting was entirely based on the acquired input and output pulse shapes and powers.

These gain and saturation parameters were then used to simulate the adaptive process on the computer using the Simulated Annealing algorithm described above. The result of this simulation was an input waveform that was generally quite close to the required input. This waveform was then finally fed to the experimental adaptive process where the computer took real measurements and looked for the minimum fitness factor.

7.4 Properties of EOM

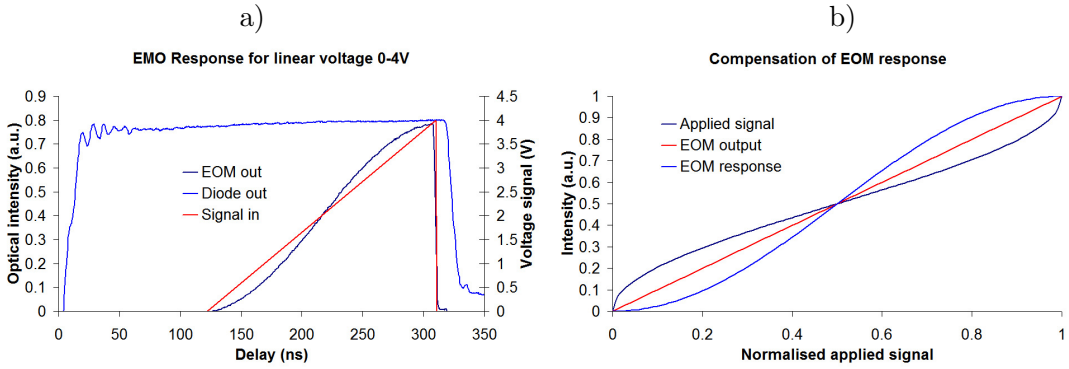

Figure 7.5: Properties of EOM: a)Response of EOM, b)EOM response compensation.

The previous section assumes a linear dependence of the optical output of the EOM to the waveform sent to the AWG 2. However, the response of the EOM to modulation is generally not linear. The response function of the EOM is sinusoidal with respect to the applied modulation. The nonlinear response of the EOM has to be compensated for by applying an appropriate transformation.

The EOM gave the highest transmission when the maximum voltage was set at 4V. Therefore, all waveforms from the AWG 2 were scaled such that their amplitudes are at 4V. Also, a DC offset was required in order to maximised the extinction ratio of the EOM preventing the suppressed parts of the diode output being amplified.

Figure 7.5 a) shows the response of the EOM to a signal input, which was a linearly ramped pulse from 0V to 4V in 200ns. It shows clearly that the response is a function that can be written in form:

$$y = 0.5(1 - cos(\pi x)) \tag{7.1}$$

where x is the normalised voltages (x=0:1 corresponding to voltage=0:4V). Hence, to

achieve a linear dependence of the output with time a calibration function can be used:

$$y = \frac{1}{\pi} arcos(1 - x/2) \tag{7.2}$$

This compensation is applied on all waveforms sent to the EOM. Figure 7.5 b) shows the effect of this compensation. The final result is a straight line which indicates that the EOM response can be compensated very effectively.

7.5 Square and Very Long Two-Stepped Pulse Shaping

The generalisation of the waveform into segments will allow much more flexibility to generate more complicated pulses if required. However, in most applications, the most desired pulses are still the square and two-stepped pulses. Square pulses allow high energy pulses to be generated without significant nonlinear effects. Square pulses can be also used to increase the effectiveness of nonlinear frequency conversion such as Raman Scattering. Two-step pulses are useful for applications such as welding that require a high initial power spike to ignite the process then a low constant power to maintain the process most effectively. This chapter will only report these two pulses. However, any other pulse shapes can also be generated upon specification.

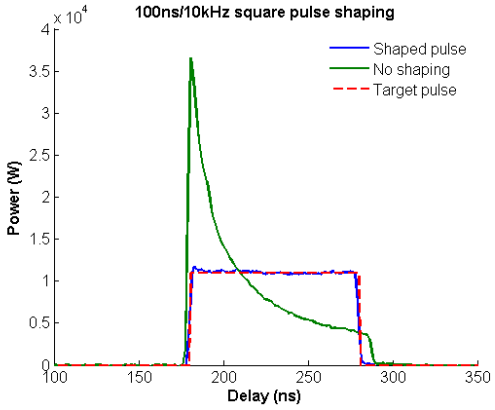

Figure 7.6: Shaping square pulse.

Figure 7.6 shows the output of the MOPA operating at maximum power with 33W pump producing 10W signal at 10kHz. With no active pulse shaping, a square input to the MOPA resulted in a highly distorted pulse with a spike at the front with a peak power reaching 35kW and a very low power of 3kW at the tail of the pulse. These pulse will generally generate large a amount of nonlinear effect if they propagates further

into materials with some nonlinear optical properties such as silica fiber. The nonlinear processes will occur unevenly across the pulse as seen in Chapter 5.

However, with the effective pulse shaping, a pulse with much lower peak power could be obtained whilst the pulse energy is maintained, in this case at 1mJ. The peak power had reduced significantly from more than 35kW to only 11kW across the whole pulse. It took about 40 iterations to converge to the final result. Because of the uniform power across the pulse, any nonlinear effects that depend on peak power will occur across the whole pulse. Also, since the peak power has been reduced significantly, much higher pulse energies can be achieved before nonlinear effects start to be significant. The next section of this chapter will investigate Raman generation rather than avoidance using this square pulse.

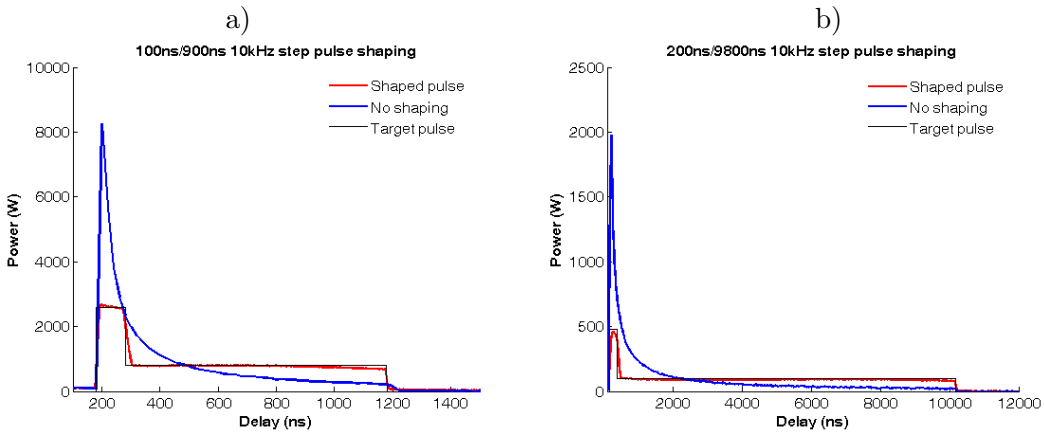

Figure 7.7: Shaping long step pulses.

Shaping of a 1μs long two-stepped pulse with initial peak of 100ns and the second part of 900ns is shown in Figure 7.7 a). The peak power ratio of the first part to second is 3:1. Figure 7.7 b) shows another result for the two-stepped pulse where the total duration was 10μs which comprised of 200ns initial peak and a 9.8μs tail with peak power ratio of 5:1. Again, the obtained pulses fitted the target output shapes very nicely. The shaped pulse had the same energy as the non-shaped pulse but with energy of the front spike transferred to the tail of the pulse. For non-shaped pulse, the initial spike has a very high peak power but the power is almost exponentially decreased to a very lower power at the tail of the pulse. These shaped pulses are useful for applications that require a high initial power then a constant power for the rest of the pulse period.

7.6 Individual Raman Stokes Component Generation Using Shaped Square Pulse

So far, significant effort has been invested in controlling the peak power of the amplifier output to reduce the nonlinear effects, especially Raman scattering, because they result in unwanted broadening of the output spectrum and limit the peak power of the desired signal. However, with appropriate control method, useful Raman Stokes can be generated. In this section, the high peak power square pulse of the output of the amplifier is used to pump a single mode fiber to produce individual Raman Stokes components.

The output of the MOPA was then launched into a 41m single mode fiber, Corning Hi1060. The maximum total power launched into the fiber was limited to only 1.8W when the MOPA was operating at 20kHz and 30W pump. There are reasons for this relatively low launched power. Firstly, a birefringent polarisation isolator was used to prevent back reflection to the MOPA; this isolator only allowed one polarisation of the beam to be coupled into the fiber resulting in a 3dB loss. Also, the postamplifier output was slightly multimoded, which led to reduced coupling efficiency into the single mode Raman fiber.

According to Equation 2.45 on page 22, the threshold for first order Raman peak is calculated to be around 450W. Therefore, with the average available power of up to 1.8W (900W peak power with 100ns/20kHz pulse), large amount of SRS can still be generated.

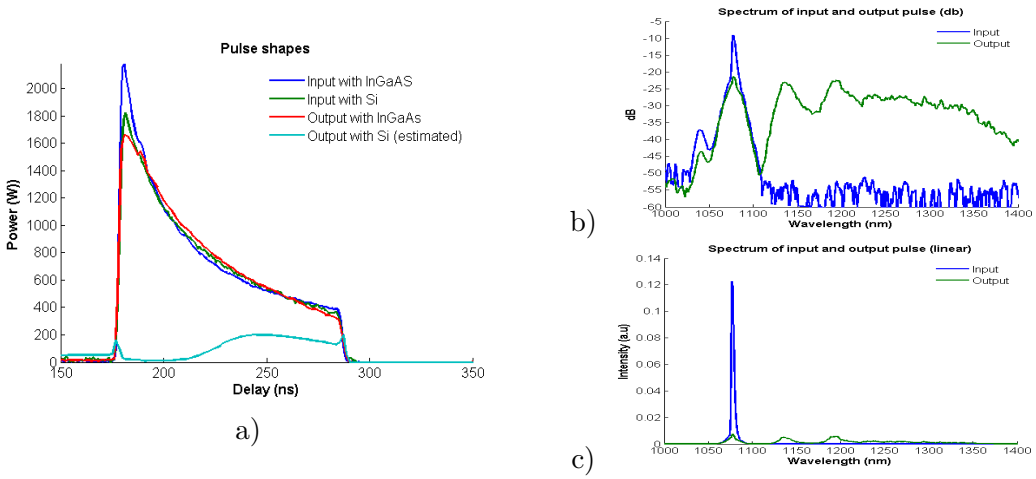

Figure 7.8: Shaping long step pulses.

Figure 7.8 shows the results of Raman generation when no active pulse shaping was applied. The launched pulse has a duration of 100ns, peak power at the front of around 2kW and a tail power of 400W as shown in Figure 7.8 a). Figure 7.8 b) and c) shows the measurement of the spectrum on log and linear scales. The plots have been normalised

to have the same area under the curves. These graphs clearly show that large amount of Raman was generated, however, there were many orders of Raman Stokes present in the pulse due to the variation of the power across the pulse.

Two detectors were used to measure the input and output pulses of the Raman fiber. The InGaAs detector works with broadband spectra while the Silicon detector only detects wavelengths less than 1100nm. Therefore, the InGaAs detector detects both pump at 1077nm and higher Raman wavelengths and the Silicon detector only measured the pump at 1077nm. The pulse energy measured with the Silicon detector was estimated based on the energy of the part of the spectrum up to 1100nm. Figure 7.8 a) shows clearly that at the output of the Raman fiber, the pump pulse has been depleted unevenly across the pulse. The point where the spike was in the input pulse is now depleted the most, while the tail of the pulse is depleted much less. The spike was the main cause for high order SRS. The distribution of Raman peaks for this type of pulse was analysed in Section 5.2.

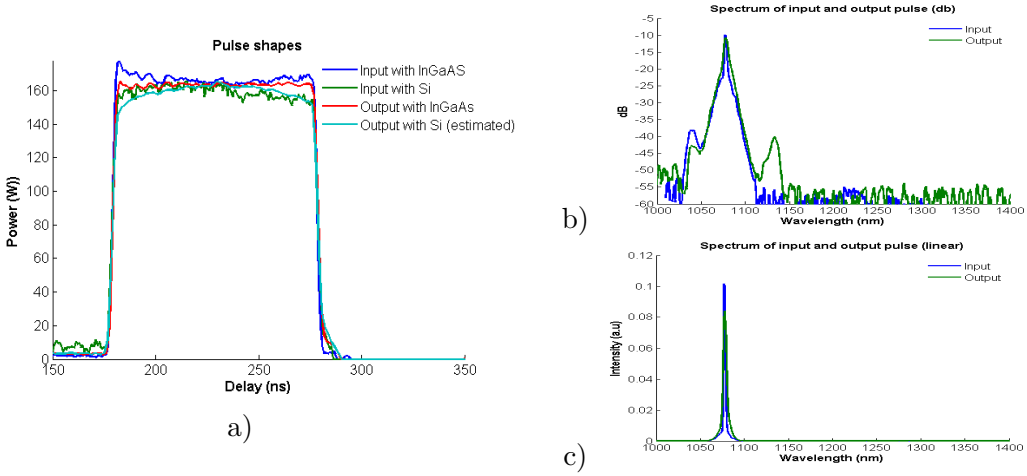

Figure 7.9: Low Raman pulse.

With pulse shaping now in place, a square pulse of the 1077nm pump was obtained and used to generate Raman pules. Figure 7.9 shows the first case where a very small amount of Raman was generated. In this case, there is almost no difference in pulse shapes measured with different detectors. There is only some small difference in spectra of the input and the output. The output spectrum has been broadened by Self-Phase Modulation.

Figure 7.10 shows the case when the 1077nm pump peak power was at 600W, which was above the estimated threshold of 450W. A large portion of the pump power now has been transferred to the 1st order Raman pulse. However, no higher order Raman peak has been generated. It is also clear that the remaining pump and the 1st order Raman

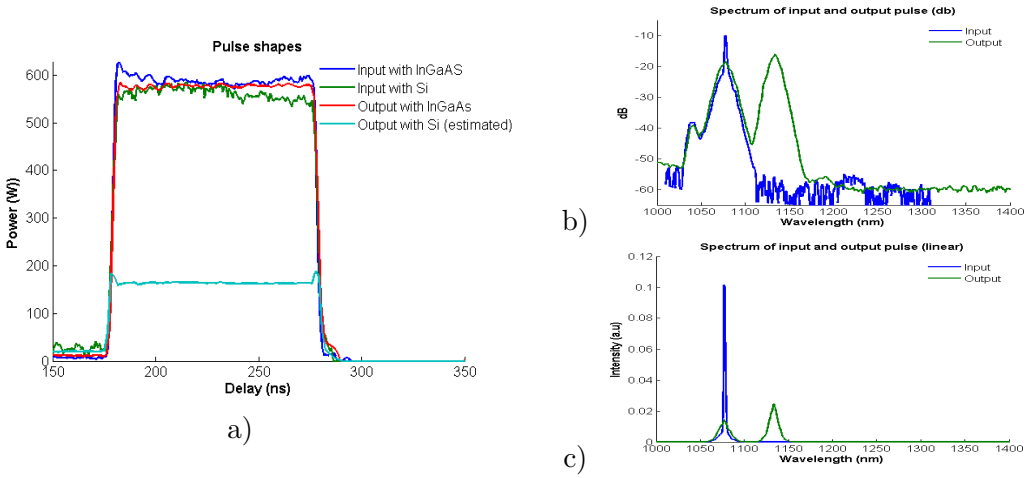

Figure 7.10: First-order Raman Stokes.

pulses now remain flat at the power level of 400W. The Raman Scattering occurs evenly across the pulse.

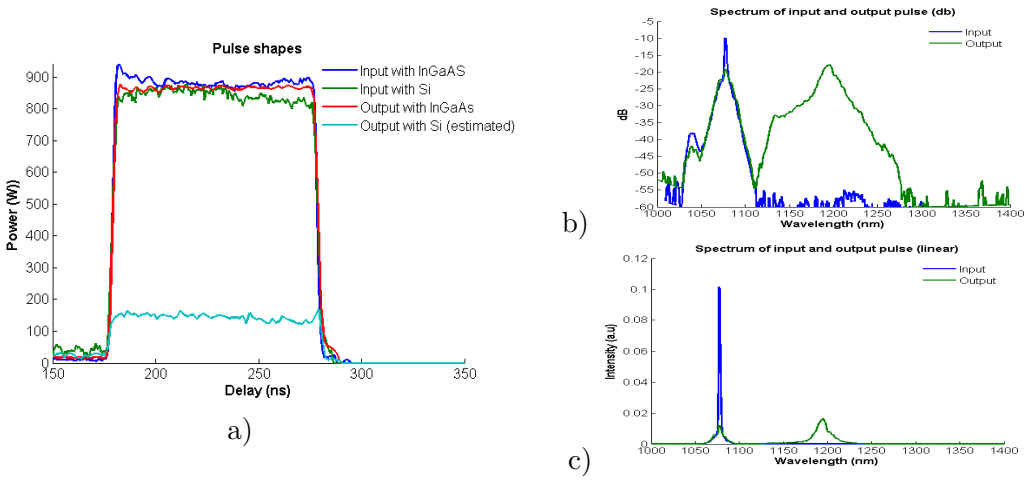

Figure 7.11: Second-order Raman Stokes.

As the pump peak power increased further, the energy from the pump continues to be transferred to the first-order Raman Stokes pulse. The first-order Raman Stokes now acts as the pump for the second-order Raman Stokes. Since the Raman threshold is inversely proportional to the wavelength, a higher threshold level is required as the pump wavelength increases. Therefore, it requires 480W of peak power in the first-order Raman Stokes to start to generate a second-order line. Again, once the threshold is reached, the power is transferred rapidly to the Raman pulse.

At the maximum available pump peak power of 900W, the 2nd order Raman pulse was fully generated and the 1st order Raman virtually disappears as shown in Figure 7.11. The first-order Raman Stokes is at least 15dB lower than the second-order Raman Stokes

peak. Furthermore, no other higher order Raman components were seen. The remaining pump pulse stayed at a similar level and shape as in the case of the first order pulse. Once again, the 2nd Raman pulse was a square pulse with an estimated peak power of about 700W.

These results provide strong evidence that higher order Raman Stokes could be generated if higher power is available. However, as the Raman order increases, the threshold will increase proportionally. At the same time, the Raman pulse will be broadened significantly. This will decrease the extinction ratio between pumping peak and the generated peak. A Raman amplifier can be built if an appropriate wavelength is used to seed the input of the Raman fiber. This will help to reduce the broadening effect and increase the extinction ratio.

7.7 Conclusion

Active pulse shaping using an EOM has been used to generate useful pulses for various applications. With active pulse shaping, the energy of the pulses is kept at 1mJ level but the peak power can be reduced significantly from 35kW to 11kW. Also, the energy in the spike in the non-shaped amplified pulse can be shifted to the tail of the pulse making the whole pulse useful.

This chapter also concentrates on two other tasks: reducing the nonlinear effect and optimising of nonlinear effect using the adaptively-shaped square pulses. The square pulses at the output of the amplifier are preferable as they lower the nonlinear effect. Also, the square pulses can be used to generate individual Raman Stokes components.

Chapter 8

Gain-Switched Diode Producing 1.06μm Picosecond Pulses

8.1 Introduction

Picosecond pulse sources at the 1.06μm regime are very attractive for the development of high power ultrashort pulse systems such as Second Harmonic Generation (SHG), Optical Parametric Oscillators (OPOs), material processing, biological imaging, and even as sources for parabolic pulse amplification to generate ultrashort pulses. Currently, picosecond pulses are commonly generated by mode-locking such as mode-locked fibre lasers [Fermann et al. (1991), Hofer et al. (1991), Tamura et al. (1993), De Souza et al. (1993), Ilday et al. (2003)], harmonically mode-locked fibre lasers [Yoshida and Nakazawa (1996), Deng et al. (2004), Roth et al. (2004)] and external cavity mode-locked semiconductor lasers [Derickson et al. (1992), Yvind et al. (2002)]. Some of the major disadvantages of this method are that it requires a complex set-up and the repetition rate can only be changed if the cavity length is varied. Also, stable operation is difficult to maintain in mode-locked lasers.

An alternative method to generate ps pulses is to use gainswitching of a semiconductor laser. Gain switching can be a very attractive way to generate ultrashort pulse sources because of its simplicity, convenience and low cost. Gain-switched diode lasers are widely used in telecommunications applications, and have recently also been used as seed lasers for high-power cladding-pumped rare-earth doped fiber amplifiers emitting at 1.55μm [Poelker (1995), Hak Kyu et al. (1995), Street et al. (1996), Wang et al. (1998), Thomsen et al. (2004)]and at 1.06μm [Piper et al. (2005a), Piper et al. (2005b), Dupriez et al. (2005), Dupriez et al. (2006)]. Investigation of 1.3μm InGaAsP gain-switched diode has been also been carried out by [Liu et al. (1989)].

In order to promote good spectral quality output (lasing on a single longitudinal cavity

mode) some form of optical seeding of the gain-switched diode is required. In this chapter, a detailed comparison of the spectral and temporal performance in injection and self seeding is presented. In injection seeding, an external narrow-line width cw DFB laser is fed to the diode so that it produces only wavelengths around the seeded laser wavelength. On the other hand, self seeding involves reflecting a portion of each pulse back into the laser diode using a Bragg Fiber grating. Compared to injection seeding, self seeding has considerable advantages in terms of simplicity and reduction in cost. For this reason, it is important to establish whether self seeding leads to any degradation of performance compared to injection seeding. This report will for the first time make a direct comparative study of injection and self seeding in FP semiconductor diode at 1060nm. It aims is to demonstrate that a high quality source of picosecond pulses can be made with a simple setup and at a very low cost.

A linear Frequency-Resolved Optical Grating (FROG) technique based on Electro-Optic Modulation (EOM) was also used to fully characterise pulses from a 1.06 μm fast photo laser diode for the first time. The output of the diode pulse shape was measured using EOM-FROG technique. The chirped pulse of the diode output was then passed on to a chirped fibre Bragg grating which provides optimum pulse compression. The time bandwidth product reduced from around 3.0 at the diode output to 0.7 at the output of the grating. Higher order chirp was the main cause for the pulse not to be transform limited.

8.2 Gain-Switched Diode Setup

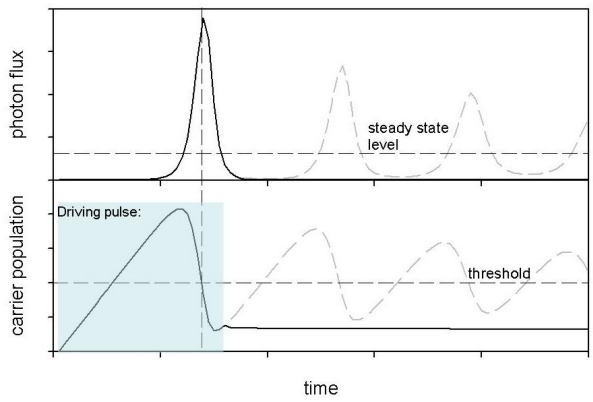

Figure 8.1: Generation of ultrashort pulse by gain switching technique.

The gain-switching of semiconductor laser diodes technique was first presented by Ito

et al. (1979). They showed that by injecting the semiconductor laser with short electrical pulses, optical pulses much shorter than the electrical pulse durations could be generated. The laser is biased just below threshold and a modulation current is superimposed on a continuous bias drive current. The modulation current can be a train of short electrical pulses or a large amplitude sinusoid. If the electrical pulse is terminated before the rise of the second peak of the relaxation oscillation, an optical pulse much shorter than the driving electrical pulse can be produced. Figure 8.1 shows schematically the principle of gain-switching.

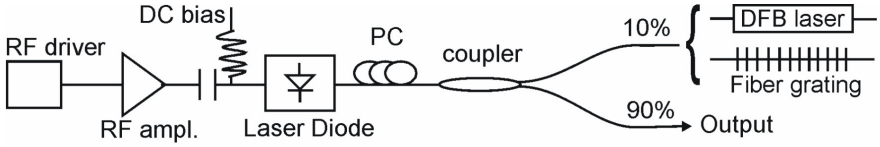

Figure 8.2: Gain switched diode setup.

Figure 8.2 shows the gain switched setup that was used in the experiments. The Fabry-Perot (FP) semiconductor laser, which was supplied as a joint product of Southampton Photonics and Bookham, was a 1060nm InGaAsP device with a threshold current of 34 mA, a modulation bandwidth much greater than 1.35 GHz and a longitudinal mode spacing of 0.2 nm. The diode was mounted in a butterfly mount on a home made printed circuit board.

Gain switching was realised by driving the laser with a modulated drive signal superimposed on a DC bias current. The injected modulation signal was around 1 GHz 35.6 V peak to peak amplitude electrical sinusoid generated by a signal generator and amplified with a RF amplifier. The -6 dBm input power to the RF amplifier was sufficient to saturate the amplifier so as to clamp the gain and reduce noise introduced from the amplifier. The bias tee and DC block provided isolation with a frequency cutoff of (<10kHz) between the DC bias source and the RF modulation signal.

Figure 8.3 shows the pulse shapes and spectrum of the gain-switch diode without any seeding. Without seeding, the diode had a broad spectrum with a FWHM of ∼25 nm. The spectrum consisted of modes spaced at 0.2 nm, corresponding to the short cavity length of ∼500μm. The pulse duration at FWHM was 61ps. The average output power was 3.5 mW. The pulse energy and peak power were then calculated to be around 3.5pJ and 20mW, respectively.

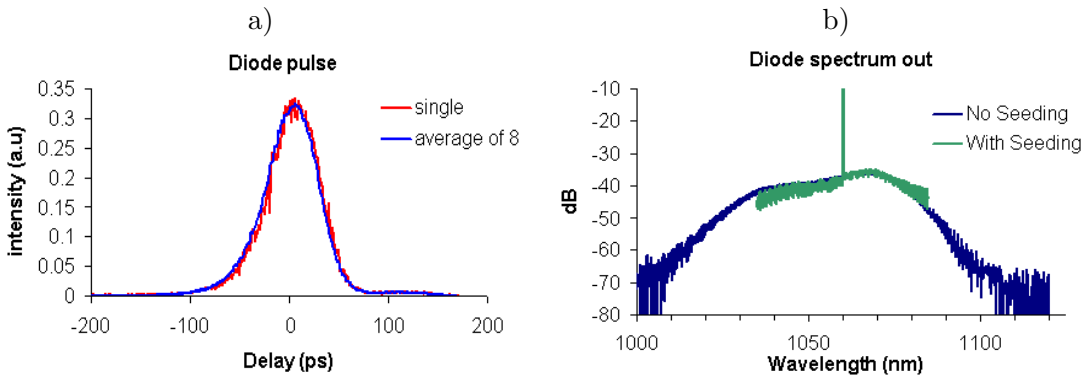

Figure 8.3: Output pulse and spectrum of the gain-switched diode without any seeding.

8.3 Injection Seeding

The diode output was spliced to a 10% coupler, allowing for a small seed signal, either from an external laser or the diode output, to be fed back to the diode as shown in Figure 8.2. In the first case, the seed signal to the diode came from a cw DFB fiber laser operating at 1059.9 nm with a line width of less than 100 kHz and an output power adjustable in the range 0.2-1.4 mW, corresponding to 20-140μW being coupled to the gain-switched diode. Because the DFB was a cw laser the effective seeding power only occurs for a relatively smaller fraction of time around the instant that the gain-switched pulse is being generated.

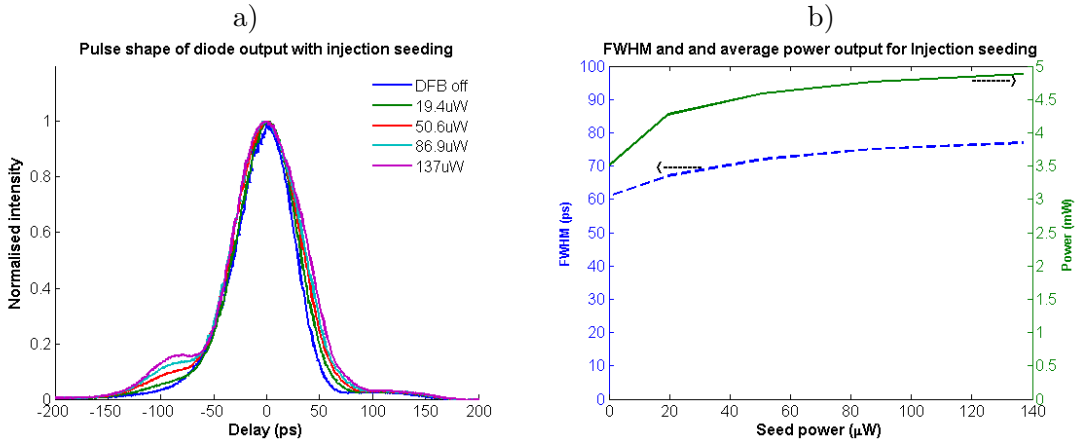

Figure 8.4: Pulse shapes with their FWHM width and the diode power output at various DFB laser seeding powers.

The pulse and spectra at the output were recorded as a function of the seed power. Figure 8.4 shows the summary of the measurement. As expected, the output power increased as the seed power increased and it reached a saturation value of around 5mW. It clearly indicates that there was a small change in the pulse shape as the seeding power increases. As the output power increased there was a small penalty for the pulse width. The pulse

width at FWHM increased from 61ps to 78ps as the seed increased from 20μW to 140μW. Also, there were clear pre-pulse features for high seeding levels. These pre-pulse features grew with seeding power and occupied a few percent of the total power of the pulse as the seed energy increased to 140μW. They stayed at a fixed position at about 100ps before the peak of the pulse.

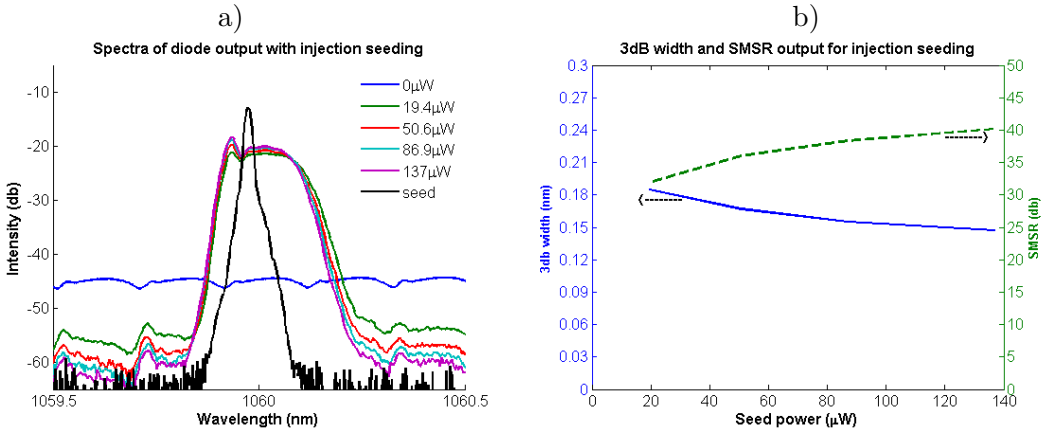

Figure 8.5: Spectra with their 3dB width and the side mode suppression ratios at various DFB laser seeding powers.

Figure 8.5 shows a series of plots of the spectra of the output as the seeding power increased. There was a spike on the spectra at the lower wavelength edge. The spectra show clearly that the side mode suppression ratios (SMSRs) increased significantly with seed power. Although, the spectral width decreased slightly from 0.184nm to 0.147nm as the seed power increased from 19.4μW to 137μW, there was only a small decrease of the time-bandwidth products (TBWPs) from 3.3 to 3.0. These TWBPs indicated that the pulse was highly chirped. The chirped pulse generated by gain-switched diodes have been well reported before [Linke (1985), Tucker (1985), Dudley et al. (1999)]. The measurement of this chirp will be discuss in the next sections of this chapter. This chirped pulse can be compressed to a smaller pulse width such that the TBWP is close to the transform limited value.

The quality of the output depended strongly on the relative position of the seed wavelength with respect to the FP mode of the laser. As seen in Figure 8.5, the FP diode laser produces a spectrum with a mode spacing of 0.2nm. Therefore, if the seed wavelength is tuned relative to the mode structure this dependence can be measured. In this experiment, however, the relative position of the seeding wavelength and diode mode were changed by varying the temperature of the gain-switched diode through a TEC controller. As the temperature decreased, the mode moved to the left (decreasing wavelength). The

rate of changes was measured to be 0.10kΩ/0.2nm. The TEC controller had a accuracy of 0.01kΩ.

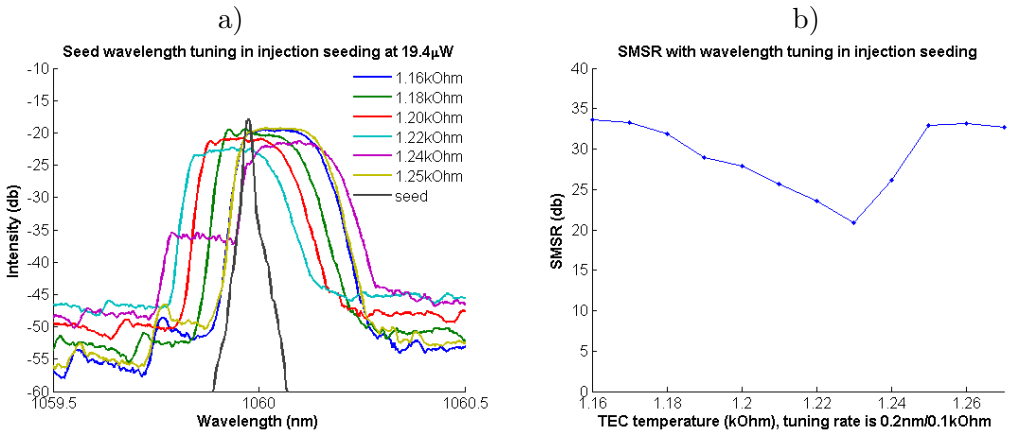

Figure 8.6: Tuning of spectra by changing the relative position of the mode to the seeding laser (at lowest seeding level of 19.4μW).

Figure 8.6 a) shows the spectra at the output as the mode was tuned across the seeding wavelength. The highest SMSR occurred when the seeding wavelength was located at the lower wavelength edge of the mode. As the TEC reading increased, the quality of the output spectra reduced as the mode tuned beyond the seed wavelength until the seeding wavelength was at the lower wavelength edge of the next mode. The Figure 8.6 b) shows that the SMSR at the seeding level of 19.4μW, the SMSR varied from a maximum value of 34dB to a minimum value of 20dB. Despite the use of a complicated, expensive DFB laser, a very specific spectral condition has to be maintained for the gain-switch diode to work at the optimum condition.

8.4 Self seeding

A set of gratings were used to feed some of the output power back to the FP diode. They included gratings with 5, 10, 20, 40 and 50 % reflectivities with relatively narrow bandwidths of around 0.2nm and a 99% reflectivity with a bandwidth of about 1nm. These corresponded to 0.05-1% of the diode output being fed back. All of these gratings had slightly different centre wavelengths as shown in Figure 8.7 a). However, to show them in perspective the spectra were normalised to have the same peaks and centre wavelengths as shown in Figure 8.7 b). The diode output at off-resonant conditions was used as a probe beam, therefore, there were ripples on the spectra due to the modes of the diode. Despite the large bandwidth of the 99% grating, the output of the diode depended very little on

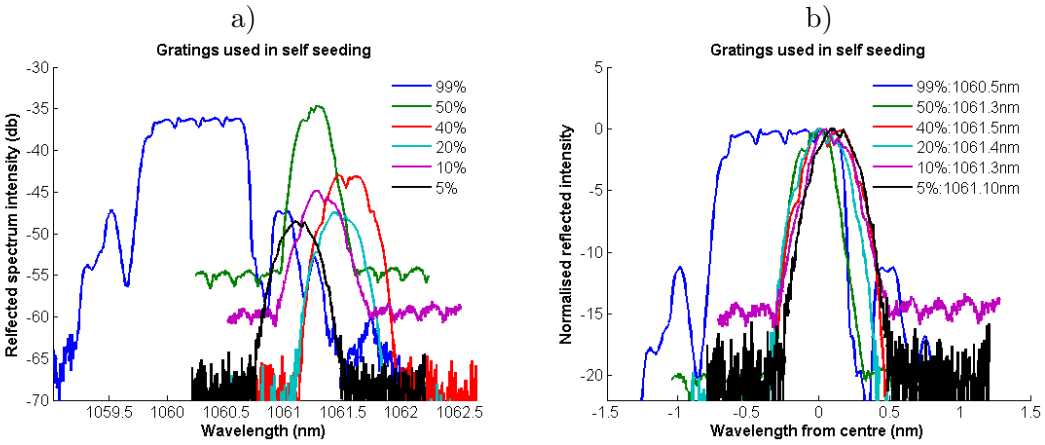

Figure 8.7: Properties of gratings used in the experiments. The gratings of 5, 10, 20 and 40 % reflectivity are with relatively small bandwidth of around 0.2nm. The gratings of 99% reflectivity have a much larger bandwidth of 1nm. a) raw reflection data b) re-scaled and re-centred reflection for comparison. The centre wavelengths of these gratings are shown on the right hand-side graph.

the bandwidth as will be shown next.

In the self-seeding case, it is important that seed pulse feedback needs to be synchronised with pulse emission. Thus, the round trip time between the diode and grating must be a multiple of the delay between pulses. In this experimental configuration, the corresponding fundamental repetition rate was ∼9.1 MHz. The diode was driven with a sinusoidal electrical signal at 109 times this frequency (∼992MHz), with a superimposed dc bias current of 30mA.

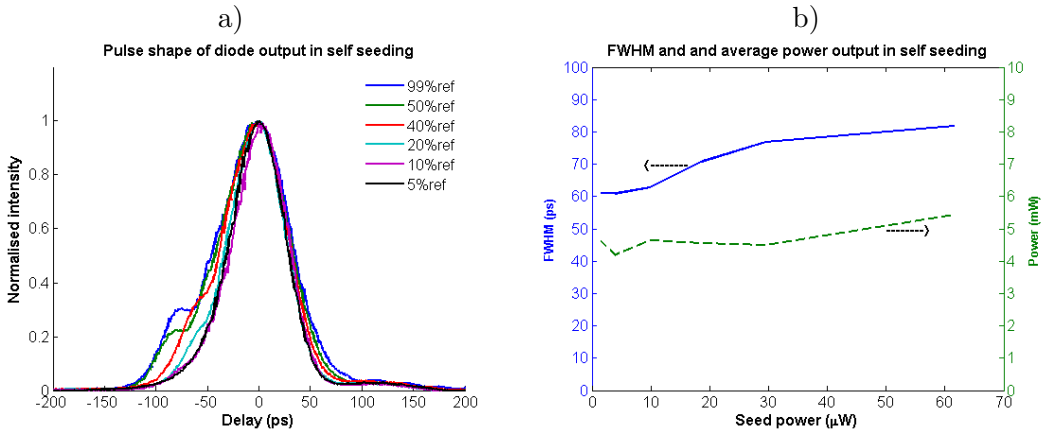

Figure 8.8: Pulse shape, width and power of the output with various gratings which gives different level of seeding.

The output pulse using those gratings are reported in Figure 8.8 a) and 8.8 b). For each grating used, the output pulse was optimised to obtained the maximum SMSR by adjusting the driving frequencies to ensure proper synchronisation and a polarisation controller to

rotate the seed pulse polarisation to optimise condition.

At the optimum SMSR, the shape of the output pulses were almost identical to the case of the DFB laser seeding. There were pre-pulse features at the front at about 80ns before the peak. These pre-pulse feature grew as the seeding power increased (in this case, higher reflectivity gratings were used). The FWHM width of the pulse increased from 61ps with no seeding to about 80ps. Meanwhile the average power at the output slightly raised to about 5.5mW.

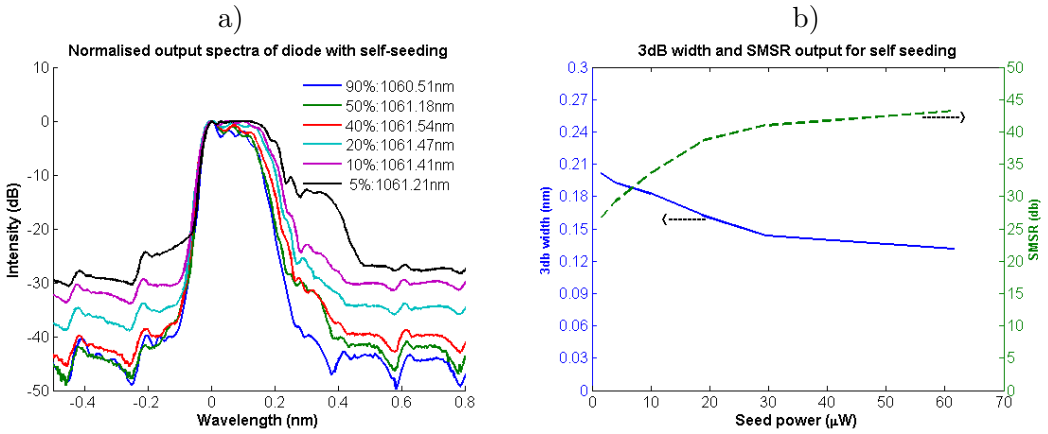

Figure 8.9: Spectra of the output with various gratings which gives different level of seeding.

The summary of the measurements of the output is shown in Figure 8.9. Figure 8.9 a) shows the normalised spectra where the peaks and centre wavelengths have been placed at the same point. The output spectrum depends very little on the actual spectral properties of the gratings. The SMSRs and the 3dB bandwidth are plotted in Figure 8.9 b). The trends in these factors are very similar to the case of DFB laser seeding. As the reflectivity of the grating increased (higher seeding power) the SMSRs increased from about 27dB with the lowest reflectivity of 5% to reach the highest SMSR of 42dB with a reflectivity of 99%. The inverse happened to the spectral bandwidth of the output, it lowered slightly as the amount of seeding increased. As a result, the TBWP changed slightly as well, reaching values of around 2.8 at maximum seeding to 3.2 at low seeding levels.

With the 50% grating in place, the driving frequency was tuned around the optimum value in order to estimate the tolerance of the system to external factors such as ambient temperature which could change the effective path lengths of the cavity and ultimately detune the system out of the optimum condition. As shown in Figure 8.10, the spectra of the output depended very strongly on the drive frequencies. However, the acceptable drive frequency had a bandwidth of about 1MHz. Within this bandwidth, the output pulse was

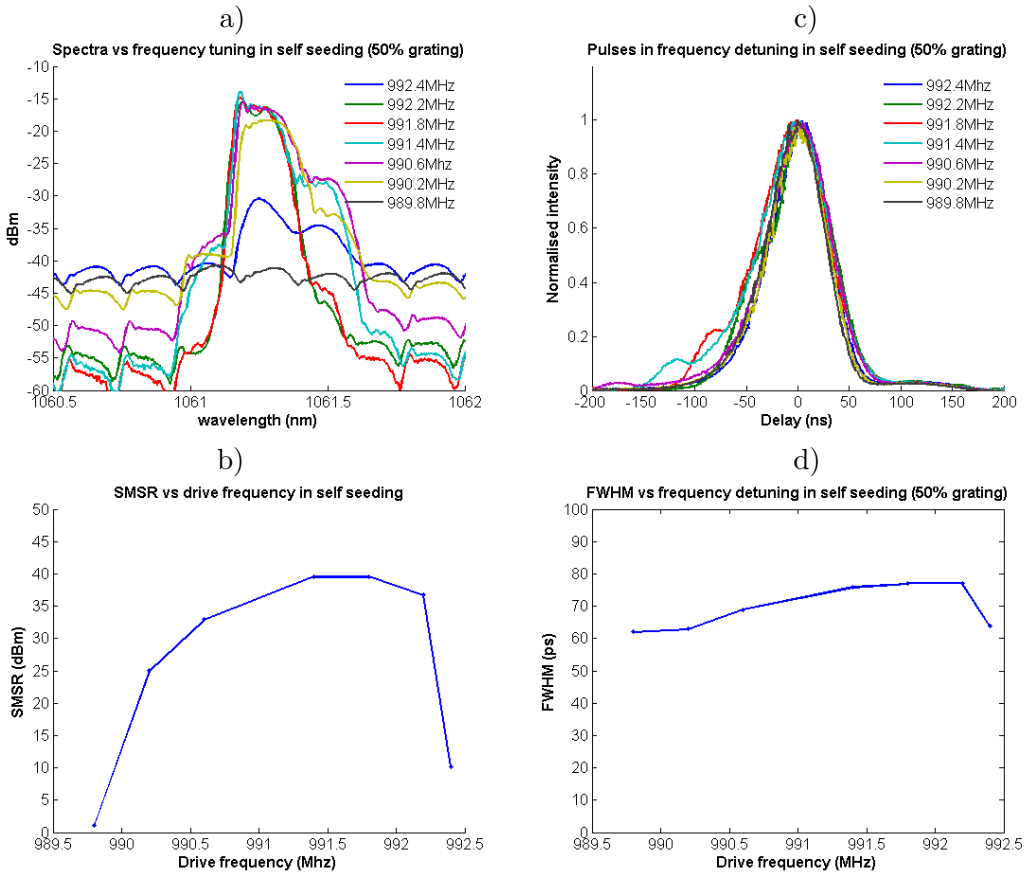

Figure 8.10: Spectra and pulse of the output with various drive frequency.

at optimum condition with, in this particular case, an SMSR of 40dB and a FWHM pulse width of around 72ps. The output pulses had very interesting pre-pulse features as shown in Figure 8.10 c). These features moved along the front end of the pulses as the drive frequency varied. As the frequency increased passing through the optimum value, the pre-pulse feature moved closer to the centre peak of the pulse. This, together with results in the DFB seeding case, suggests that the best seeding time for the diode pulse is not when the pulse reaches the maximum but actually at some time of order of 100ps before. This effect could be related to the response time of the FP semiconductor diode.

8.5 Direct Comparison of Injection Seeding and Self Seeding

In both the injection seeding and self-seeding cases, the output power increased slightly with seeding power (to about 5mW average power, corresponding to ∼5 pW pulse energy) as one would expect. Timing and amplitude jitter were reduced by seeding. The unseeded

pulses had an amplitude jitter of ∼7% and a timing jitter of ∼4 ps. For both types of seeding, over the range of seed powers investigated, the amplitude jitter was ∼2%; timing jitter was ∼3 ps, dominated by jitter from the drive electronics which was estimated to be ∼2ps.

In the injection seeding case, the SMSRs were strongly dependent on the position of the wavelength of the seed laser from the centre wavelength of the diode. With self seeding, this adjustment is not available, but a similar dependence was observed by detuning the repetition rate of the diode from the cavity harmonic frequency. SMSRs in excess of 40dB were achievable in both cases, with the SMSR increasing with seed power. High SMSRs were achieved at lower average seed powers in the case of self-seeding. In both cases, at SMSR values greater than about 30dB, a small secondary feature began to appear in the leading edge of the pulse.

Figure 8.11 plots the spectra(a) and pulse shapes (b) of the output of the diode for both injection and self-seeding at a similar SMSR level of 40dB. The spectra and pulse shapes at this condition were very similar in both cases. The self-seeding case had a narrower spectral width but higher pulse width. There were clearly secondary features at the leading edge of the pulses for both situations.

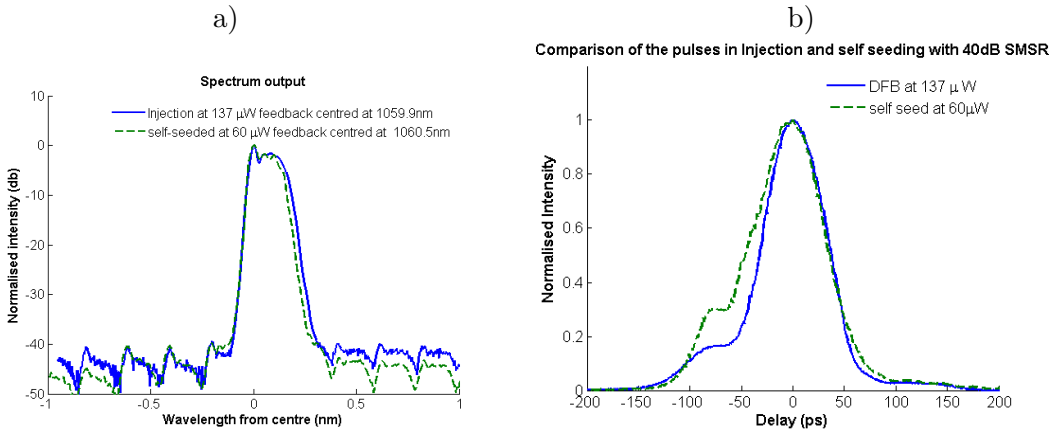

Figure 8.11: Direct comparison between DFB and self seeding: a) the spectra with SMSR of 40dB b) the corresponding pulse shape

For both types of seeding, pulse durations (as measured on a fast scope) increased and the spectrum narrowed slightly as the seeding power was increased. The dependence of TBWP on seed power level is shown on 8.12. At low seed powers FWHM durations of ∼65ps and bandwidths of ∼0.19 nm were observed. At the highest seed powers, the injection seeded pulses showed a duration of 77 ps and a bandwidth of 0.15nm (TBWP=3.1) and self-seeded pulses showed a duration of 82 ps and a bandwidth of 0.13nm (TBWP=2.8).

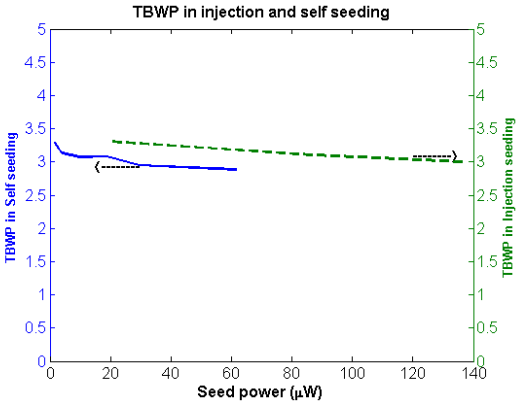

Figure 8.12: Direct comparison between DFB and self seeding: a) the spectra with SMSR of 40dB b) the corresponding pulse shape

Clearly, as expected with gain-switching, the pulses were strongly chirped.

8.6 FROG Technique Using EOM

8.6.1 Principle

In order to measure directly the chirp parameter of the output pulse, Frequency-Resolved Optical Grating (FROG) can be used. However, FROG techniques based on nonlinear processes (e.g. SHG-FROG) are poorly suited for the characterisation of picosecond pulses from these diodes because of the relatively low peak power. Here a FROG technique developed initially for telecoms at 1.5μm, based on linear gating is used [Dorrer and Kang (2002)]. This technique is highly sensitive, allowing characterisation of long duration, low energy pulses. It also has the advantage of simplicity and convenience, being achievable with fully fiberised components and using only electronic delays. To the best of my knowledge, this is the first time this technique has been used to characterise pulses at $\sim$1.06μm.

A spectrogram of the pulse is constructed by means of measuring the spectrum of the gated pulse as a function of the delay between the pulse and the gate. There is virtually no restriction on the modulators that can be used as a gate, as long as the gate width is not much higher than 10 times the duration of the pulses to be measured. This characterization technique is extremely sensitive, since it does not rely on nonlinear optics [Dorrer and Kang (2002)].

Assume that an optical pulse is represented by the analytic signal $E(t)$ and a temporal modulator is denoted as $G(t)$, both quantities being complex. The procedure for the

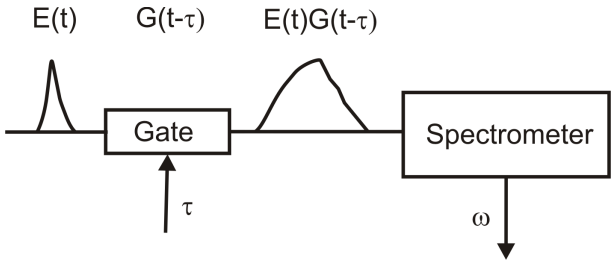

Figure 8.13: Schematic of the measurement of a spectrogram for simultaneous retrieval of the electric field of an optical pulse E(t) and the response of a temporal modulator G(t).

simultaneous determination of $E(t)$ and $G(t)$ is shown schematically in Figure 8.13. A programmable delay τ between the pulse and the gate can be set such that the output pulse is related to the input pulse by $E'(t) = E(t)G(t-\tau)$. One then builds up the spectrogram $S(\omega,\tau)$ by measuring the spectrum of the gated pulse as a function of the optical frequency ω and relative delay τ [Dorrer and Kang (2002)]:

$$S(\omega,\tau) = |\int_{-\infty}^{\infty} E^{'}(t,\tau)e^{-i\omega t}dt|^2 = |\int_{-\infty}^{\infty} E(t)G(t-\tau)e^{-i\omega t}dt|^2 \tag{8.1}$$

The extraction of both the pulse $E(t)$ and the gate $G(t)$ from the measurement spectrogram $S(\omega,\tau)$ is equivalent to a two-dimensional blind deconvolution [DeLong et al. (1995)]. This can be performed with the principle component generalised projection algorithm [Kane (1998)] which gives a unique solution in most cases . The retrieval does not require any assumptions and provides a complete description of both the pulse and the gate.

8.6.2 Setup

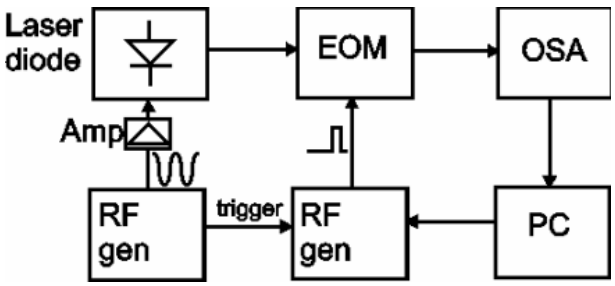

Figure 8.14: The experimental setup of FROG measurement using an Electro-Optic Modulator. The computed was programmed to control the RF generator delay and collect the spectrum on the OSA after each delay.

The detailed setup that was constructed for the FROG measurement using an EOM is shown in Figure 8.14. The output from the 90% port of the coupler was fed, via a

fiber polarisation controller, to a fiberised EOM. The modulator was driven by a square wave generator triggered by a signal from the diode driver. The amplitude of the output voltage was 5V. The square-wave generator was controlled by a PC which could vary both the pulse duration and delay of the pulse from the trigger signal. This created a timing window for transmission of the light from the diode. The minimum gate time was ∼200 ps, determined by the response of the EOM. The step of delay was set at 5ps. The output of the EOM went to an OSA with 0.01nm resolution. In this way, the signal can be spectrally resolved as a function of delay to produce a spectrogram. The system was fully fiberised and all delays were electronic rather than optical. Numerical retrieval was carried out on the spectrogram and independently recovered the diode signal and the EOM sampling function. The code for the blind deconvolution was written by Michaël Roelens at the ORC, University of Southampton. The code has been used very successfully for monitoring the performance of high bit-rate WDM systems at 1.5μm [Roelens et al. (2004) and Roelens et al. (2005)]. Pulse information can be retrieved even for pulses which are shorter by a factor of >10 than the gating time [Dorrer and Kang (2002)].

8.6.3 Results

The described FROG technique was used to characterise the output of the gain switch diode for both cases of injection and self seeding. As the output of the diode has a TBWP of around 3, therefore, they are chirped. This technique allowed us to learn about the chirp properties of the output pulse in more detail. The chirped pulse was then put through a chirped Fiber Bragg Gratings which was designed to optimally compressed the diode output to the minimum pulse width. Using the same FROG setup, the pulse intensity and phase of the compress pulses were also measured. The pulse and phase of the gate was also retrieved consistently as shown on Figure 8.15.

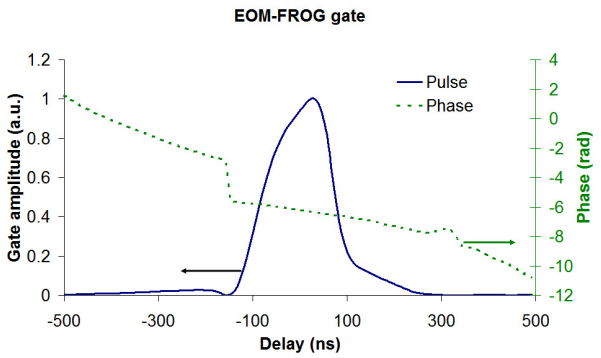

Figure 8.15: The retrieved pulse and phase of the EOM gate.

Uncompressed pulses

Initially, the output of the diode was passed directly to the EOM. The spectrograms were collected for the two cases of injection seeding and self-seeding. With injection seeding, the seed was set at 19.4μW. At this level, there is no pre-pulse feature as shown in Figure 8.4. The TBWP at this level of seeding was at 3.3. With self-seeding case, the 99% reflectivity grating was used. The output pulse has a pre-pulse at about 100ps in front of the pulse. The TBWP was 2.8.

A direct verification of the accuracy of this technique was obtained by comparing the retrieved pulses and spectra to the directly measured pulses by a Digital Communication Analyser (DCA) and spectra by an Optical Spectrum Analyser (OSA). In this experiment, DCA with a maximum sample resolution of 30Ghz (30ps resolution) and an OSA with a resolution of 0.01nm were used. Figure 8.16 shows a typical sets of results obtained. On the left hand side of the Figure are the graphs for the injection seeding case, where the agreement between the retrieved traces and the directly measured traces was excellent. The spectral agreement was down to 30dB from the maximum intensity. There was only a slight discrepancy in the pulse intensity at the front edge of the pulse.

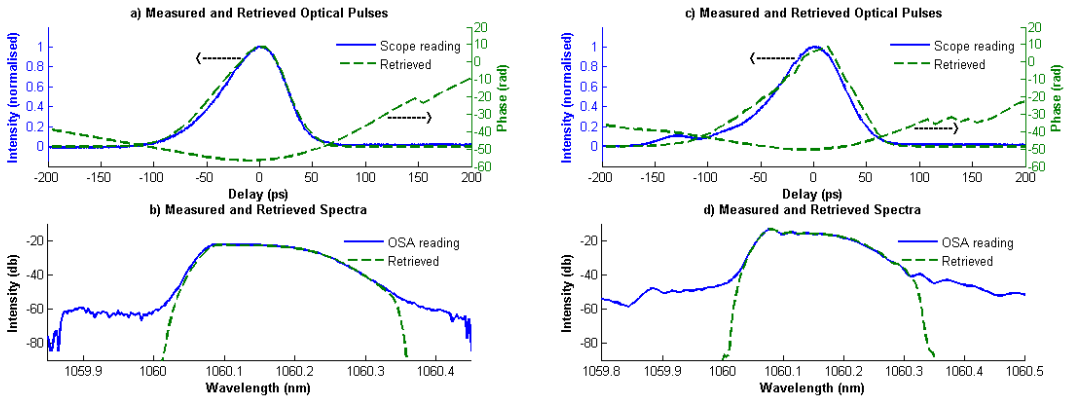

Figure 8.16: Directly measured and retrieved properties of the uncompressed optical pulse a):pulse intensity and phase, b): spectra of the injection seeding at 19.4μW seeding; c): pulse intensity and phase, d): spectra of the self seeding at 60μW seeding.

The agreement between the retrieved pulse and the DCA measured pulses for the self-seeding case (Figure 8.16 a)) was not quite as good as the injection seeding case (Figure 8.16 c)). Despite the excellent agreement in spectral measurement, the retrieved pulse deviated from the DCA measured pulse at the front edge of the pulse where the pre-pulse is located.

Compressed pulses

The output fiber of the diode was spliced to the chirped Fiber Bragg Grating through a fiber circulator. The total power of the pulse reflected back to the final output is about 50% of the output of the diode. The grating wavelength was finely adjusted by applying tension to the grating to match the pulses and to produce the optimally compressed output pulses. The reflected pulses were then analysed with the EOM-FROG.

The same set of measurements was repeated for the compressed pulses. The results are shown in Figure 8.17. Once again, the retrieved spectra were in excellent agreement with the directly measured ones by using a high resolution OSA. Due to the limited response of the pulse detector and the DCA, the directly measured intensity profile could not be used to compare with the retrieved pulses as shown in the two graphs at the top of Figure 8.17. Conventional nonlinear FROG measurement could not be used as an alternative due to the low peak intensity pulses. However, there is an indirect method to get convincing verification. Since the chirp grating only introduces a chirp that compensates the initial chirp of the pulse it did not introduce nonlinear effects into the pulse. The chirp grating can also be considered as a simple dispersive element. Therefore, using simple short pulse propagation calculations with the split-step method [Agrawal (2001)], it is possible to calculated the optimally compressed pulse.

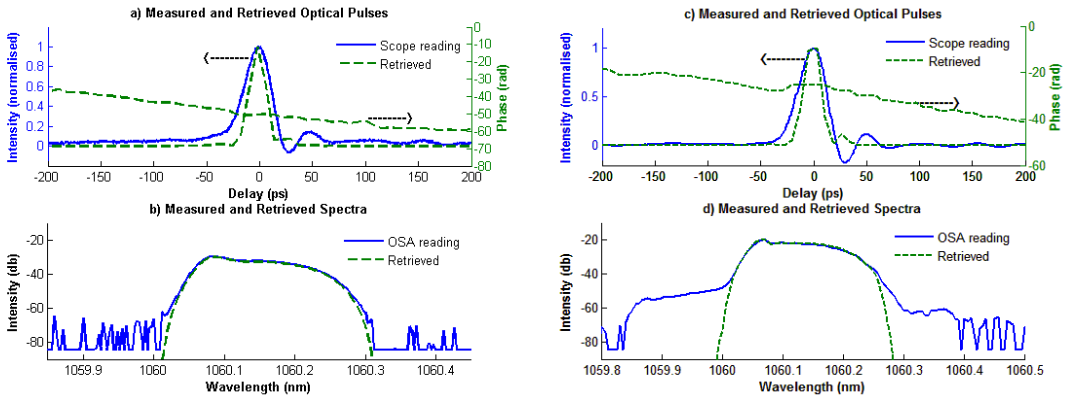

Figure 8.17: Directly measured and retrieved properties of the compressed optical pulse a):pulse intensity and phase, b): spectra of the injection seeding at 19.4μW seeding; c): pulse intensity and phase, d): spectra of the self seeding at 60μW seeding.

Pulse Reflection from Chirped Fiber Bragg Gratings

Figure 8.18 shows the results of the retrieved and simulated intensities and phases of the pulses. FROG measurements of the pulses showed that in both the injection and self-

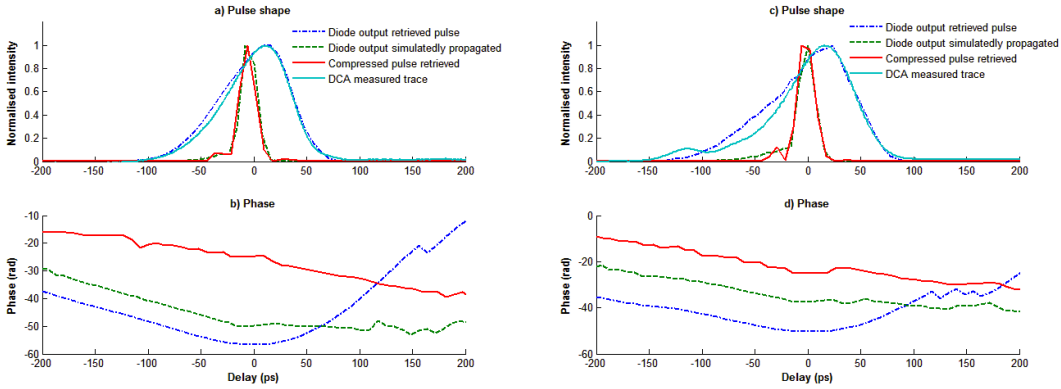

Figure 8.18: Optimally compressed pulses; the TBWP reduced from around 3.0 in uncompressed pulses to 0.70 in compressed pulses. a) and b): pulse intensities and phase of the injection seeding at 19.4μW seeding; c) and d): pulse intensities and phase of the self seeding at 60μW seeding

seeding cases the diode output pulses had nearly linear chirp (chirp slope $\sim$0.0025ps^{-2} in both cases) and hence should be cleanly compressible to near the transform limit. The top graphs show the intensities of both uncompressed and compressed pulses. They clearly show that the simulated compressed pulses are in excellent agreement with the EOM-FROG retrieved compressed pulse. Both show that the minimum duration of the compressed pulses was $\sim$18ps (TBWP=0.7) and that $\sim$90% of the pulse energies is in the main peak. The phases of the pulse in the bottom graphs of the figure also show that the phases across the compressed pulses were approximately linear, other than some higher order components.

8.7 Conclusion

Whilst the advantages of self over external injection seeding in terms of simplicity and cost are obvious, this is the first detailed study to be undertaken to investigate the differences in performance of a gain-switched diode depending on whether it is self or externally seeded. The results show that there was no significant difference in performance of self seeding and injection seeding. For both approaches a SMSR of greater than 40dB was readily achievable, differences in pulse duration and shape were small, amplitude and timing stability were the same and, crucially for ultrafast applications, both approaches were shown to produce pulses with a close to linear chirp across the centre of the pulse, allowing compression using a simple linearly chirped fiber grating. The compensated pulse had a pulse duration of less than 20 ps, corresponding to a TBW product of $\sim$0.7.

A highly sensitive linear FROG technique, originally developed for telecoms applica-

tions at 1.55 μm, was used to analyse pulses from a picosecond FP laser diode operating at 1.06μm for the first time. The data was used to design a fiber Bragg grating for optimum pulse compression. The experimental setup for the FROG measurements is simple to construct using standard fiberised components, completely alignment free and fully computer controlled, and works well with low energy, long duration pulses which are difficult to characterise using techniques based on optical nonlinearities.

Chapter 9

Conclusion

9.1 Introduction

This project has concentrated on important aspects of nanosecond laser source development: LMA fiber characterisation for high power pulse MOPA system, the realisation of a commercial 0.5mJ MOPA systems, characterisation of SRS generated by high peak power of pulses, active pulse shaping of 1mJ MOPA to improve the versatility of the system and individual Raman order generation with shaped square pulses.

The square output pulse of the high energy amplifier is an important result in this project. With the shaped square output pulse, the total energy was kept the same as the non-shaped pulse but the peak power was significantly reduced. Therefore, nonlinear effects could then be decreased significantly or controlled to produce pulses with desired properties. If the Raman Stokes is generated by a square pulse, the individual high-order Stokes can be produced consecutively depending on the level of power providing a useful wavelength tunable sources.

Furthermore, this project also investigated picosecond pulses from gain-switched diode at 1.06μm as a potential seeding source for the high power MOPA. A comparative study of injection seeding and self seeding was also performed. The properties of pulses from the two seeding methods were measured with an innovative FROG technique using an EOM.

9.2 Large Mode Area Fibers

One of many challenges of fiber amplifiers is to maintain single mode operation in large mode area fibers. As the diameter of the core of the fiber increases to accommodate higher power and reduce nonlinear effect, the number of modes increases as well making the fiber multimoded. However, the simple method to achieve single mode operation is to bend the fiber below a critical bend radius such that bending loss for high order modes are very high and loss for fundamental mode is relatively small [Koplow et al. (2000)].

A series of LMA fibers with diameters in the range from 20μm to 40μm with the numerical apertures of around 0.06 were investigated in detail from output mode observation, bend loss measurement to M^2 and mode field diameter measurement. The experimental results were in good agreement with the simulation results. The fibers from the more top hat preform with NA of ∼0.06 gave single mode operation for all fibers of 20, 30, and 40 μm core diameters by bending them to radii of 90mm, 50mm and 30mm, respectively. The output was quasi-single mode with M^2 close to 1. The measurements showed that the flat top index profile is the preferred choice over more complex profiles as light follows the refractive index profile in low numerical aperture, large core fibers very strongly.

The profile of the fundamental mode can also be manipulated to reduce the nonlinear effect caused by its high peak power of the centre of the mode. Strategic control of refractive index profile and doping region of the fiber can be further investigated as an advanced method of reducing the peak intensity of the fundamental mode. The refractive index profile with a dip at the centre can flatten the single mode. If the whole core area is doped, the centre of the fundamental mode tends to form a shape with very high peak at the centre of the fiber. In the strategic doping technique, dopants are introduced as a ring within the core such that the fundamental mode gets amplified to generate a relatively flat mode. Simulation has shows that the fundamental mode could be flattened to reduce the peak intensity by up to 50%. This technique will required a significant investment in fiber fabrication technique. At the time of this project, there was not enough resource to perform these experiments.

9.3 Nanosecond Pulsed Fiber MOPA

First, a fully fiberised MOPA consisted of a directly modulated nanosecond laser diode, a preamplifier and a postamplifier were built. The fully fiberised MOPA was possible because of the use of GTWave fiber technology from Southampton Photonics. The directly modulated diode allowed flexibility in setting the pulse repetition rate, duration and shape. The output of the diode could have a repetition rate ranging from a few kHz to a few hundred kHz and a duration from few nanoseconds to few microseconds.

The performance of the 0.5mJ MOPA was investigated in both long pulse and short pulse cases. A 20μm core diameter with a numerical aperture of 0.07 was used in the postamplifier. For long pulses of 100ns and a repetition rate of 20kHz, there were very little nonlinear effects introduced, however, the output pulse was reshaped significantly.

An output of more than 0.4mJ has been achieved with the available pump power of 30W. The short pulse of 20ns at a repetition rate of 20kHz produced a significant amount of SRS when the postamplifier was pumped with 30W of power. The peak power limit of the signal at 1070nm was at 13kW for a 3m passive delivery fiber. The total peak power, including SRS, was as high as 30kW.

Then, the postamplifier was replaced with a free-space end-pumped fiber. The new fiber had a core diameter of 30μm and numerical aperture of 0.06. This allowed much higher pulse energy and peak power to be generated with little effect of SRS. Raman-free 1mJ pulses were easily produced at 10kHz repetition rate with 30W of pump at 915nm.

I have also now demonstrated the power scaling of the actively shaped pulse MOPA. A third power amplifier was added to the setup. The fiber of the power amplifier had a 43μm diameter ytterbium doped core with a numerical aperture of 0.09. The D-shaped inner cladding had a 650/600μm diameter and a nominal NA of 0.48. The pump absorption rate in the inner cladding was ∼3dB/m at the 975nm pump. The fiber length used in the final stage of amplification was 8 m. The backward pump power of 500W produced signal average power of 312W with a slope efficiency of 66%. The pulse was at 100kHz repetition rate and 200ns duration. Pulse with energy of 3.1mJ and peak power of 50kW was produced. The ASE level was 17dB below the signal peak.

9.4 Active Pulse Shaping

Two separate methods of active pulse shaping of the MOPA were demonstrated. The first was to directly modulate the diode with a shaped electrical pulse, the second was to modulate the optical pulse with an EOM after the diode to carve the output pulse to an arbitrary optical pulse. These two methods based on the same algorithm of Simulated Annealing [Kirkpatrick et al. (1983)]. These have been effective and versatile methods of controlling pulse shape in high gain amplifiers. Both methods of pulse shaping, direct shaping of diodes and using EOM, have shown promising results.

With EOM shaping, the quality improved significantly over direct modulation of the diode due to the inherent properties of the diode and design of the circuit board. The diode has a dynamic range of only 10dB compared to more than 30dB of the EOM. There are also oscillatory feature on the output pulse of the diode for the duration of 100ns. This feature could not filtered out in the direct modulation method, therefore, the final output pulse contained some high spikes on top of the pulse envelope. The EOM shaping

completely suppressed the oscillatory feature. Furthermore, as the diode operated near the threshold, significant noise was introduced to the pulse, hence instability was a major issue with pulses that required very low power in the leading edge. This was a major limitation for the square output pulse case. The pulse energy achieved for this pulse was only 0.2mJ in the diode modulation and 1mJ in the EOM modulation. The instability problem disappeared for the cases where the leading edge of the input pulse was well above the threshold as in cases of triangle and two-step pulse. The maximum pulse energy that could be achieved in these pulses were only limited by the available pump power.

With the use of EOM, arbitrary pulse shapes can be generated without any restriction. As a demonstration, I have generated Gaussian and parabolic pulses with fitness factors of below 0.1 (10%). I have also performed high average power (200W output signal at 1070nm using 350W pump at 975nm on the third amplifier) shaping of square, two-step, Gaussian and parabolic pulse.

Furthermore, different effects can be used as a measure of the fitness factor, for instantly, the efficiency of nonlinear conversion processes, Raman, welding yield, welding speed. Future experiments are needed to fully explore these aspects of the adaptive pulse shaping.

9.5 Stimulated Raman Scattering in Nanosecond Pulsed Fiber Amplifier

The dynamics of SRS Stokes pulse formation have been also investigated in detail. The temporal and spectral scans were performed on the pulses exhibiting a significant Raman broadened spectrum. It was shown that, the signal energy transferred to the Stokes signal vary rapidly when the SRS threshold had been reached. For a pulse with an uneven power distribution across its temporal profile, the Raman Stokes generation starts at the highest power level and quickly spreads to the lower power part of the pulse [Wang (2005a)]. As demonstrated in the case of unshaped square pulses, the spike at the front of the pulse initiates the Raman Scattering and almost all of the power is transferred to Raman Stokes when more pump power was put into the amplifier.

The maximum peak power of the 1077nm signal came out at the end of the beam delivery fiber was the same as the SRS threshold. With 3m of 20μm delivery fiber, the RSR threshold was around 13kW. The threshold was inversely proportional to the length

of the delivery fiber. The use of a suitable Photonic Bandgap Fiber would reduce the effect of SRS significantly. However, more research is required into making large mode PBGF and into coupling the power from ordinary large mode fiber to the PBGF. Therefore, active pulse shaping is an attractive options to reduce the peak power in high energy pulse amplification.

In the demonstration of versatility of active pulse shaping, SRS pulses were generated in a single mode fiber using a shaped square pulse. The experiments showed that there were great improvements in the quality of Raman Stokes spectrum compared with the non-shaping case. Without any shaping, only a very broad Raman spectrum could be produced and the pump signal got distorted further due to uneven nonlinear effect across the pulse. However, with shaped square pulse individual Raman peak could be generated and both the pump and Raman pulses remained square. This indicated that individual Raman pulses of a very high order could be generated if enough power is available. This can be a potential candidate for being a useful wavelength tunable source. High-order narrow-bandwidth Raman amplifier can also be possible with an appropriate feeding wavelength.

9.6 Gain-Switched Diode Producing 1.06μm Picosecond Pulses

A detail investigation of the performance of 1.06μm picosecond gain-switched diode was also done as a part of my project. The purpose was to use this source as a seed for the MOPA system. The gain-switched diode was seeded by two methods: injection seeding and self seeding. The direct comparison between this two methods is reported for the first time. The injection seeding was though the use of a narrow-bandwidth distributed feed back laser at 1060nm. The self seeding was done using simple fiber Bragg gratings with various reflectivities and bandwidths and centre wavelengths around 1060nm. It was found that the quality of the gratings was not an important factor affecting the quality of the pulse output.

An EOM was used again in the characterisation of picosecond pulses. The EOM-FROG technique in a fiberised system at 1060nm was used for the first time. With the use of only electronics delay to obtain the spectrogram, it was shown to be a very simple but effective method for low power pulse characterisation. The results showed that there was little difference in the performance of the gain-switched diode under both injection or

self seeding operation.

In both cases, high side mode suppression ratios of more than 40dB were achieved. Pulse widths of 60-80ps were also easily obtained directly from the diode. However, these output pulses were approximately linearly chirped allowing them to be compressed to much shorter pulses. The compression was done by the use of a linearly chirped fiber Bragg grating designed to compensate the chirp of the diode. Compressed pulses with a FWHM width below 20ps were achieved. The compression reduced the time bandwidth product from around 3 in noncompressed pulses to 0.7 in compressed pulses. Further compressed was not possible with a linearly chirped grating due to high order chirped in the pulses.

References

G.P. Agrawal. *Nonlinear Fiber Optics*. Academic Press, USA, third edition, 2001.

M. Artiglia, G. Coppa, P. Di Vita, M. Potenza, and A. Sharma. Mode field diameter measurements in single-mode optical fibers. *Journal of Lightwave Technology*, 7(8):1139–52, 1989.

C.H. Avila, R.L. Burnham, Youming Chen, W. Torruellas, H.R. Verdun, and R.A. Utano. Polarization-maintaining master oscillator fiber amplifier (MOPA) for high-repetition-rate applications. *Proceedings of the SPIE - The International Society for Optical Engineering Fiber Lasers: Technology, Systems, and Applications, 26-28 Jan. 2004*, 5335(1): 24–32, 2004.

C. Barnard, P. Myslinski, J. Chrostowski, and M. Kavehrad. Analytical model for rare-earth-doped fiber amplifiers and lasers. *IEEE Journal of Quantum Electronics*, 30(8): 1817, 1994.

N.G.R. Broderick, H.L. Offerhaus, D.J. Richardson, and R.A. Sammut. Power scaling in passively mode-locked large-mode area fiber lasers. *IEEE Photonics Technology Letters*, 10(12):1718–20, 1998.

N.G.R. Broderick, H.L. Offerhaus, D.J. Richardson, R.A. Sammut, J. Caplen, and L. Dong. Large mode area fibers for high power applications. *Optical Fiber Technology: Materials, Devices and Systems ACOFT '98: Australian Conference on Optical Fibre Technology, 5-8 July 1998*, 5(2):185–96, 1999.

S. R. Chinn. Simplified modeling of transients in gain-clamped Erbium-doped fiber amplifiers. *Journal of Lightwave Technology*, 16(6):1095, 1998.

E. A. De Souza, C. E. Soccolich, W. Pleibel, R. H. Stolen, J. R. Simpson, and D. J. DiGiovanni. Saturable absorber modelocked polarisation maintaining Erbium-doped fibre laser. *Electronics Letters*, 29(5):447–9, 1993.

Kenneth W. DeLong, Rick Trebino, and William E. White. Simultaneous recovery of two ultrashort laser pulses from a single spectrogram. *Journal of the Optical Society of America B: Optical Physics*, 12(12):2463, 1995.

Y. Deng, M. W. Koch, G. W. Wicks, and W. H. Knox. Colliding-pulse passive harmonic mode-locking in a femtosecond Yb-doped fiber laser with a semiconductor saturable absorber. *Optics Express*, 12(16), 2004.

D. J. Derickson, R. J. Helkey, A. Mar, J. R. Karin, J. G. Wasserbauer, and J. E. Bowers. Short pulse generation using multisegment mode-locked semiconductor lasers. *IEEE Journal of Quantum Electronics*, 28(10):2186–202, 1992.

F. Di Teodoro and C. D. Brooks. 1.1MW peak-power, 7W average-power, high-spectral-brightness, diffraction-limited pulses from a photonic crystal fiber amplifier. *Optics Letters*, 30(20):2694, 2005.

F. Di Teodoro, J.P. Koplow, and S.W. Moore. Diffraction-limited, 300kW peak-power pulses from a coiled multimode fiber amplifier. *Optics Letters*, 27(7):518–20, 2002.

M. J. F. Digonnet, editor. *Continuous-Wave Silica Fiber Lasers.* Rare-Earth-Doped Fiber Lasers and Amplifiers. Marcel Dekker, USA, second edition, 2001.

V. Dominic, S. MacCormack, R. Waarts, S. Sanders, S. Bicknese, R. Dohle, E. Wolak, P.S. Yeh, and E. Zucker. 110W fibre laser. *Electronics Letters*, 35(14):1158–60, 1999.

C. Dorrer and I. Kang. Simultaneous temporal characterization of telecommunication optical pulses and modulators by use of spectrograms. *Optics Letters*, 27(15):1315–17, 2002.

J. M. Dudley, L. P. Barry, J. D. Harvey, M. D. Thomson, B. C. Thomsen, P. G. Bollond, and R. Leonhardt. Complete characterization of ultrashort pulse sources at 1550 nm. *IEEE Journal of Quantum Electronics*, 35(4):441–50, 1999.

P. Dupriez, A. Piper, A. Malinowski, J. K. Sahu, M. Ibsen, Y. Jeong, L. M. B. Hickey, M. N. Zervas, J. Nilsson, and D. J. Richardson. 321W average power, 1GHz, 20ps, 1060nm pulsed fiber MOPA source. Vol. 5 of *2005 Optical Fiber Communications Conference Post deadline Papers (IEEE Cat. No. 05CH37672)*, page 3 pp. Vol. 5, Anaheim, CA, USA, 2005. IEEE.

P. Dupriez, A. Piper, A. Malinowski, J. K. Sahu, M. Ibsen, B. C. Thomsen, Y. Jeong, L. M. B. Hickey, M. N. Zervas, J. Nilsson, and D. J. Richardson. High average power, high repetition rate, picosecond pulsed fiber master oscillator power amplifier source seeded by a gain-switched laser diode at 1060 nm. *IEEE Photonics Technology Letters*, 18(9): 1013–15, 2006.

M. E. Fermann, M. Hofer, F. Haberl, A. J. Schmidt, and L. Turi. Additive-pulse compression mode locking of a Neodymium fiber laser. *Optics Letters*, 16(4):244–6, 1991.

L. M. Frantz and J. S. Nodvik. Theory of pulse propagation in a laser amplifier. *Journal of Applied Physics*, 34(8):2346, 1963.

A. Galvanauskas, G.C. Cho, A. Hariharan, M.E. Fermann, and D. Harter. Generation of high-energy femtosecond pulses in multimode-core Yb-fiber chirped-pulse amplification systems. *Optics Letters*, 26(12):935–7, 2001.

F. Ghiringhelli, K. Vysniauskas, L. M. B. Hickey, M. N. Zervas, A. Malinowski, and D.J. Richardson. Pulse shaping in high gain all-fiber pulse MOPA. In *CLEO Europe 2005*, Munich, 2005.

C. Randy Giles and E. Desurvire. Modeling Erbium-doped fiber amplifiers. *Journal of Lightwave Technology*, 9(2):271–283, 1991.

L. Hak Kyu, P. Seo Yeon, K. Kyong Hon, and L. El-Hang. Two-stage Er^{3+}-doped fiber amplifier to generate transform-limited high-power pulses from a gain-switched 1.5-μm DFB laser diode. OFC '95 Optical Fiber Communication. Summaries of Papers Presented at the Conference on Optical Fiber Communication. Vol. 8. 1995 Technical Digest Series. Postconference Edition, pages 170–1, San Diego, CA, USA, 1995. Opt. Soc. America.

D.C. Hanna, R.M. Percival, I.R. Perry, R.G. Smart, P.J. Suni, and A.C. Tropper. An Ytterbium-doped monomode fibre laser: broadly tunable operation from 1.010 μm to 1.162 μm and three-level operation at 974 nm. *Journal of Modern Optics, Ninth National Quantum Electronics Conference, 18-22 Sept. 1989*, 37(4):517–25, 1990.

M. Hofer, M. E. Fermann, F. Haberl, M. H. Ober, and A. J. Schmidt. Mode locking with cross-phase and self-phase modulation. *Optics Letters*, 16(7):502–4, 1991.

F. O. Ilday, J. Buckley, L. Kuznetsova, and F. W. Wise. Generation of 36-femtosecond pulses from a Ytterbium fiber laser. *Optics Express*, 11(26), 2003.

D. Inniss, D.J. DiGiovanni, T.A. Strasser, A. Hale, C. Headley, A.J. Stentz, R. Pedrazzani, D. Tipton, S.G. Kosinaki, D.L. Brownlow, K.W. Quoi, K.S. Kranz, R.G. Huff, R. Espindola, J.D. LeGrange, and G. Jacobovitz-Veselka. Ultrahigh-power single-mode fiber lasers from 1.065 to 1.472 μm using Yb-doped cladding-pumped and cascaded Raman lasers. In *CLEO 1997, Pastdeadline Paper CPD30*, 1997.

H. Ito, H. Yokoyama, S. Murata, and H. Inaba. Picosecond optical pulse generation from an r.f. modulated AlGaAs d.h. diode laser. *Electronics Letters*, 15(23):738–40, 1979.

Y. Jeong, J.K. Sahu, D.N. Payne, and J. Nilsson. Ytterbium-doped large-core fibre laser with 1kW of continuous-wave output power. *Electronics Letters*, 40(8):470–472, 2004.

D. J. Kane. Real-time measurement of ultrashort laser pulses using principal component generalized projections. *IEEE Journal of Selected Topics in Quantum Electronics*, 4(2): 278–84, 1998.

S. Kirkpatrick, C.D. Gelatt, and M.P. Vecchi. Optimization by simulated annealing. *Science*, 220:671, 1983.

R. J. Koester and E. Snitzer. Amplification in fiber laser. *Optics Letters*, 3(10):1192, 1964.

J.P. Koplow, D.A.V. Kliner, and L. Goldberg. Single-mode operation of a coiled multimode fiber amplifier. *Optics Letters*, 25(7):442–4, 2000.

J. Limpert, S. Hofer, A. Liem, H. Zellmer, A. Tunnermann, S. Knoke, and H. Voelckel. 100W average-power, high-energy nanosecond fiber amplifier. *Applied Physics B (Lasers and Optics)*, B75(4-5):477–9, 2002.

R. A. Linke. Modulation induced transient chirping in single frequency lasers. *IEEE Journal of Quantum Electronics*, QE-21(6):593–7, 1985.

H. F. Liu, M. Fukazawa, Y. Kawai, and T. Kamiya. Gain-switched picosecond pulse <10 ps generation from 1.3 μm InGaAsP laser diodes. *IEEE Journal of Quantum Electronics*, 25(6):1417–25, 1989.

A. Malinowski, A. Piper, J.H.V. Price, K. Furusawa, Yoonchan Jeong, J. Nilsson, and D.J. Richardson. Ultrashort-pulse Yb^{3+}-fiber-based laser and amplifier producing >25W average power. *Optics Letters*, 29(17):2073–5, 2004.

R. J. Mears, L. Reekie, S.B. Poole, and D.N. Payne. Low-threshold tunable cw and Q-switched fibre laser operating at 1.55μm. *Electronics Letters*, 22:159, 1986.

M. Muendel, B. Engstrom, D. Kea, B. Laliberte, R. Minns, R. Robinson, B. Rockney, Y. Zhang, R. Collins, P. Gavrilovic, and A. Rowley. 5-Watt cw single-mode Ytterbium fiber laser at 1.1 μm. In *CLEO 1997, Pastdeadline Paper CPD30*, 1997.

K. Nagano, S. Kawakami, and S. Nishida. Change of the refractive index in an optical fiber due to external forces. *Applied Optics*, 17(13):2080–5, 1978.

W.G. Otten, F.P. Kapron, and T.C. Olson. Mode-field diameter of single-mode fiber by knife-edge scanning in the far field. *Journal of Lightwave Technology*, LT-4(10):1576–9, 1986.

R. Paschotta, J. Nilsson, A. C. Tropper, and D. C. Hanna. Ytterbium-doped fiber amplifiers. *IEEE Journal of Quantum Electronics*, 33(7):1049–1056, 1997.

H.M. Pask, R.J. Carman, D.C. Hanna, A.C. Tropper, C.J. Mackechnie, P.R. Barber, and J.M. Dawes. Ytterbium-doped silica fiber lasers: versatile sources for the 1-1.2 μm region. *IEEE Journal of Selected Topics in Quantum Electronics*, 1(1):2–13, 1995.

A. Piper, P. Dupriez, M. Ibsen, A. Malinowski, J. H. V. Price, B. C. Thomsen, D. J. Richardson, L. M. B. Hickey, and M. N. Zervas. A compact 1GHz, 16ps pulse source operating at 1060nm incorporating a high power gain-switched semiconductor laser and fiber grating pulse compressor. 2005 Conference on Lasers and Electro-Optics Europe (IEEE Cat. No. 05TH8795), page 358, Munich, Germany, 2005a. IEEE.

A. Piper, A. Malinowski, K. Furusawa, and D.J. Richardson. High-power, high-brightness, *mJ* Q-switched Ytterbium-doped fibre laser. *Electronics Letters*, 40(15): 928–929, 2004.

A. Piper, A. Malinowski, B. C. Thomsen, D. J. Richardson, L. M. B. Hickey, and M. N. Zervas. 11.1W average power, 20 ps pulses at 1 GHz repetition rate from a fiber-amplified gain-switched 1.06 μm Fabry-Perot laser diode. Volume 2 of *2005 Conference on Lasers and Electro-Optics (CLEO) (IEEE Cat. No. 05TH8796)*, pages 1141–3, Baltimore, MD, USA, 2005b. IEEE.

M. Poelker. High power gain-switched diode laser master oscillator and amplifier. *Applied Physics Letters*, 67(19):2762–4, 1995.

C. C. Renaud, H.L. Offerhaus, J.A. Alvarez-Chavez, J. Nilsson, W.A. Clarkson, P.W. Turner, D.J. Richardson, and A.B. Grudinin. Characteristics of Q-switched cladding-pumped Ytterbium-doped fiber lasers with different high-energy fiber designs. *IEEE Journal of Quantum Electronics*, 37(2):199–206, 2001.

H. Renner. Bending losses of coated single-mode fibers: a simple approach. *Journal of Lightwave Technology*, 10(5):544–51, 1992.

M. A. F. Roelens, M. Forzati, A. Djupsjobacka, P. Petropoulos, A. Berntson, and D. J. Richardson. High quality pulse and device characterisation using EAM-based frequency resolved optical gating. Vol. 3 of *31st European Conference on Optical Communication*, pages 397–8, Glasgow, UK, 2005. IEE.

M. A. F. Roelens, B. C. Thomsen, and D. J. Richardson. Multiwavelength EAM based optical sampling for performance monitoring in high bit-rate WDM systems. Vol. 3 of *30th European Conference on Optical Communication. ECOC 2004*, pages 700–1, Stockholm, Sweden, 2004. Royal Inst. of Technol.

J. M. Roth, T. G. Ulmer, N. W. Spellmeyer, S. Constantine, and M. E. Grein. Wavelength-tunable 40GHz picosecond harmonically mode-locked fiber laser source. *IEEE Photonics Technology Letters*, 16(9):2009–11, 2004.

J. Sakai and T. Kimura. Bending loss of propagation modes in arbitrary-index profile optical fibers. *Applied Optics*, 17(10):1499–1506, 1978.

A.B. Sharma, A.-H. Al-Ani, and S.J. Halme. Constant-curvature loss in monomode fibers: an experimental investigation. *Applied Optics*, 23(19):3297–301, 1984.

A. E. Siegman. *Lasers*. University Science Books, 1986.

R. G. Smith. Optical power handling capacity of low loss optical fibers as determined by stimulated Raman and Brillouin scattering. *Applied Optics*, 11(11):2489, 1972.

E. Snitzer. Optical maser action of Nd in Barium crown glass. *Physical Review Letters*, 7(12):444, 1961.

E. Snitzer, H. Po, F. Hakimi, R. Tumminelli, and B.C. McCollum. Double-clad, offset core Nd fiber laser. In *Proc. Opt. Fiber Sensors Post-deadline power PD5*, New Orleans, 1988.

A. W. Snyder and J.D. Love. *Optical Waveguide Theory*. Kluwer Academic Pulishers, London, 1983.

R. H. Stolen and C. Lee. Development of the stimulated Raman spectrum in single-mode Silica fibers. *Journal of the Optical Society of America B (Optical Physics)*, 1(4):652–7, 1984.

M. W. Street, D. Nesset, A. D. Ellis, J. H. Marsh, and J. S. Aitchison. Generation of high peak power (615W) subpicosecond pulses using a gain-switched distributed feedback laser diode and a nonlinear fiber compression technique. *Pacific Rim Conference on Lasers and Electro-Optics, CLEO - Technical Digest*, pages 64–65, 1996.

P.J. Suni, D.C. Hanna, R.M. Percival, I.R. Perry, R.G. Smart, J.E. Townsend, and A.C. Tropper. Lasing characteristics of Ytterbium, Thulium and other rare-earth doped Silica based fibers. *Proceedings of the SPIE - The International Society for Optical Engineering Fiber Laser Sources and Amplifiers, 6-8 Sept. 1989*, 1171:244–60, 1990.

K. Tamura, J. Jacobson, E. P. Ippen, H. A. Haus, and J. G. Fujimoto. Unidirectional ring resonators for self-starting passively mode-locked lasers. *Optics Letters*, 18(3):220–2, 1993.

B. C. Thomsen, Jeong Yoonchan, C. Codemard, M. A. F. Roelens, P. Dupriez, J. K. Sahu, J. Nilsson, and D. J. Richardson. 60W, 10GHz 4.5ps pulse source at 1.5 μm. Vol. 1 of *Conference on Lasers and Electro-Optics (CLEO)*, page 2 pp. vol.1, San Francisco, CA, USA, 2004. IEEE.

R. S. Tucker. High-speed modulation of semiconductor lasers. *Journal of Lightwave Technology*, T-3(6):1180–92, 1985.

Y. Wang. Dynamics of stimulated Raman scattering in double-clad fiber pulse amplifiers. *IEEE Journal of Quantum Electronics*, 41(6):779–88, 2005a.

Y. Wang. Optimization of pulse amplification in Ytterbium-doped double-clad fiber amplifiers. *Journal of Lightwave Technology*, 23(6):2139–47, 2005b.

Y Wang, G Chen, and X Wang. The characteristics of 1.55 μm gain-switched DFB laser diode. Vol. 3547 of *Proc. SPIE - Int. Soc. Opt. Eng. (USA)*, pages 4–7, Beijing, China, 1998. SPIE-Int. Soc. Opt. Eng.

Y. Wang and H. Po. Dynamic characteristics of double-clad fiber amplifiers for high-power pulse amplification. *Journal of Lightwave Technology*, 21(10):2262–70, 2003.

E. Yoshida and M. Nakazawa. 80∼200GHz Erbium doped fibre laser using a rational harmonic mode-locking technique. *Electronics Letters*, 32(15):1370–2, 1996.

K. Yvind, P. M. W. Skovgaard, J. Mork, J. Hanberg, and M. Kroh. Performance of external cavity mode-locked semiconductor lasers employing reverse biased saturable absorbers. *Physica Scripta Volume T*, T101:129–32, 2002.

Appendix: List of Publications

K. T. Vu, A. Malinowski, M. A. F. Roelens, M. Ibsen, P. Petropoulos, D. J. Richardson. Full Characterisation of Low Power Picosecond Pulses From a Gain-Switched Diode Laser using Electro-Optic Modulation Based Linear FROG. Photonics Technology Letters. Accepted Jan 2008.

K.T. Vu, A. Malinowski, M.A.F. Roelens, M. Ibsen, D.J. Richardson. Detailed Comparison of Injection-Seeded and Self-Seeded Performance of a Gain-Switched Laser Diode. CLEO 2007, Baltimore, US, paper JWA119.

K.T. Vu, A. Malinowski, M.A.F. Roelens, M. Ibsen, P. Petropoulos, D.J. Richardson. Full Characterisation of Low Power Picosecond Pulses From a Gain-Switched Diode Laser using Electro-Optic Modulation Based FROG. CLEO 2007, Baltimore, US, paper CFF4.

K.T. Vu, A. Malinowski, D. J. Richardson, F. Ghiringhelli, L. M. B. Hickey, and M. N. Zervas. Adaptive pulse shape control in a diode-seeded nanosecond fiber MOPA system. Opt. Express 14, 10996-11001, 2006.

F. He, J. H. Price, K. T. Vu, A. Malinowski, J. K. Sahu, and D. J. Richardson. Optimisation of cascaded Yb fiber amplifier chains using numerical-modelling. Opt. Express 14, 12846-12858, 2006.